Fortschritt-Berichte VDI

VDI

Dip.-Ing. Michael Pagel,
Bad Liebenzell

Model-based diagnosis of electric cooling fan drive systems

Berichte aus dem

Institut für
Automatisierungstechnik
und Mechatronik
der TU Darmstadt

iat

Model-based diagnosis of electric cooling fan drive systems

Vom Fachbereich
Elektrotechnik und Informationstechnik
der Technischen Universität Darmstadt
zur Erlangung der Würde eines Doktor-Ingenieurs (Dr.-Ing.)
genehmigte Dissertation

von

Dipl.-Ing. Michael Pagel

geboren am 13. Januar 1983 in Daun

D 17

Darmstädter Dissertationen

Fortschritt-Berichte VDI

Model-based diagnosis of electric cooling fan drive systems

Pagel, Michael
Model-based diagnosis of electric cooling fan drive systems
Fortschr.-Ber. VDI Reihe 08 Nr. 1262. Düsseldorf: VDI Verlag 2018.
144 Seiten, 89 Bilder, 17 Tabellen.
ISBN 978-3-18-526208-1 ISSN 0178-9546,
€ 52,00/VDI-Mitgliederpreis € 46,80.

Model-based diagnosis of electric cooling fan drive systems is a contribution to the field of fault detection and diagnosis for electrically driven engine cooling fans. Its main focus is on the online gathering and determination of important parameters and internal states. The developed methods for fault detection and diagnosis are characterized by resource and computing efficient design and by a low application effort, drastically reducing the costs for transferring them to other applications. Novel algorithms are presented for determination of the winding resistance, the flux linkage over angle and the equivalent series resistance. Based on these algorithms, a new and innovative approach for determination of the magnet temperature is proposed, utilizing the winding temperature, which is derived without requiring an additional temperature sensor. Furthermore, methods are presented for detection of a demagnetization event, detection of an aged DC-link capacitor and a novel approach is introduced for detection and diagnosis of unusual load conditions, caused for example, by a blockage or dirt on the fan blade.

Vorwort

Die vorliegende Dissertation entstand während meiner Tätigkeit als Doktorand der Robert Bosch GmbH in der Vorausentwicklung des Geschäftsbereichs Electrical Drives.

Mein besonderer Dank gilt Herrn Prof. Dr.-Ing. Dr. h. c. Rolf Isermann für die Betreuung meiner Arbeit. Durch seine beständige Unterstützung, die zahlreichen Gespräche und wertvollen Diskussionen hat er sehr zum Gelingen dieser Arbeit beigetragen. Ich habe unsere Dialoge stets als Ermutigung und Motivation empfunden.

Herrn Prof. Dr.-Ing. habil. Dr. h. c. Andreas Binder danke ich für die Betreuung als Zweitgutachter und das meiner Arbeit entgegengebrachte Interesse. Seine Anregungen und kritischen Kommentare waren stets hilfreich.

Herrn Dr.-Ing. Bernd Galyga danke ich für die Anregung zu dieser Arbeit, für seine Unterstützung sowie für die mir gewährten wissenschaftlichen Freiräume. Besonderer Dank gilt auch Herrn Dr.-Ing. Lucas Ginzinger, der für das letzte halbe Jahr die Betreuung meiner Arbeit übernommen hat. Allen Kollegen sei an dieser Stelle herzlich für die freundschaftliche Arbeitsatmosphäre, die außerordentlich gute Zusammenarbeit sowie die anregenden Diskussionen gedankt.

Großer Dank gebührt auch allen Studenten, die als Praktikanten, als Werkstudenten oder im Rahmen ihrer Abschlussarbeit Teilaspekte des Vorhabens bearbeiteten. Erwähnen möchte ich an dieser Stelle insbesondere Gerhard Decker, Philippe Kocher, Volker Kimmig und Christoph Jatzek.

Besonderer Dank gilt auch meinen Eltern, die mich auf meinem Weg durch das Studium begleitet und immer an mich geglaubt haben. Ohne ihre Unterstützung wäre ein Studium und eine anschließende Promotion nicht möglich gewesen.

Schließlich möchte ich ausdrücklich meiner Frau Marie danken, die für mich während der gesamten Zeit eine sehr große persönliche Unterstützung gewesen ist. Die Fertigstellung einer Dissertation neben der täglichen Arbeit hat starke Auswirkungen auf das Privatleben. Ohne ihre Geduld, ihre mentale Unterstützung und ihr großes Verständnis hätte ein solcher Arbeitsumfang niemals gelingen können.

Bad Liebenzell, im September 2017

Contents

List of Symbols

Symbol	Description	Unit
A	(cross sectional) area	m^2
$\mathbf{A}$	Dynamic matrix	-
$\mathbf{B}$	Input matrix	-
$\mathbf{C}$	Output matrix	-
c	Specific heat capacity	$\mathrm{J\,kg^{-1}\,K^{-1}}$
C	Capacity	$\mathrm{A\,s\,V^{-1}}$
$\mathbf{D}$	Feedthrough matrix	-
E	Energy	J
i	Electrical current	A
I	DC current	A
f	Frequency	Hz
f_u, f_y	Additive faults	-
F	Transfer function	-
J	Inertia	$\mathrm{kg\,m^{-1}}$
k_fr	Friction coefficient	-
K	Gain	-
L	Inductance	$\mathrm{V\,s\,A^{-1}}$
m	Mass	kg
$\dot{m}$	Mass flow rate	$\mathrm{kg\,s^{-1}}$
M	Torque	$\mathrm{N\,m}$
n	Process noise	-
	Rotational speed	$\mathrm{min^{-1}}$
P	Power (loss)	W
$\mathbf{P}$	Covariance matrix	-
p	Pressure	Pa
$\dot{Q}$	Heat flow	$\mathrm{J\,s^{-1}}$
r	Residual	-
R	Electrical resistance	$\mathrm{V\,A^{-1}}$
$\mathbf{S}$	Upper triangular matrix	-
s	Laplace operator	$\mathrm{s^{-1}}$
	System poles	-
T	Time constant	s
	Temperature difference	K
$\mathbf{T}$	Transformation matrix	-
u	Voltage	V
u_i	Induction voltage	V
U	DC voltage	V
v	Velocity	$\mathrm{m\,s^{-1}}$

Symbol	Description	Unit
V	Cost function	-
$\dot{W}$	Heat capacity flow	$\mathrm{J\,s^{-1}\,K^{-1}}$
$\mathbf{x}$	State vector	-
y	Output signal	-
z	z operator	-
α	Heat transfer coefficient	$\mathrm{W\,m^{-1}\,K^{-2}}$
γ	Temperature coefficient	$\mathrm{K^{-1}}$
δ	Condition number	-
ϑ	Temperature	$^{\circ}\mathrm{C}$
$\boldsymbol{\Theta}$	Parameter vector	-
κ	Eigenvalue	-
λ	Forgetting factor	-
ρ	Density	$\mathrm{kg\,m^{-3}}$
σ	Singular value	-
φ	Rotor angle	rad
ξ	Duty cycle	-
Ψ	Flux linkage	$\mathrm{V\,s}$
$\boldsymbol{\Psi}$	Data matrix	-
ω	Angular velocity	$\mathrm{rad\,s^{-1}}$

Subscripts

AG	Airgap
bat	battery
br	bridge
c	cooler
cab	cable
cf	coolant fluid
cm	car manufacturer
d	dynamic
dc	intermediate circuit
el	electrical
ESR	equivalent series resistance
f	fan
fr	friction
hys	hysteresis
ind	induced
inj	injection
j	junction
l	losses
mag	magnet
mot	motor
res	resulting
rot	rotor
r	resistance
rms	root mean square
R	Rotor
s	sampling time
sp	supplier plant
st	static
sw	switching
S	Stator
vn	vehicle net
0	reference value

Abbreviations

A/D	Analog-to-Digital
AC	Alternating current
DC	Direct current
DF	Dissipation factor
CAN	Control Area Network
CFD	Computational Flow Dynamics
DSFI	Discrete Square Root Filtering
DSP	Digital Signal Processor
EC	Electonically Commutated
ECU	Electronics Control Unit
ESR	Equivalent Series Resistance
ETD	Entry Temperature Difference
EoL	End-of-Line
FEM	Finite Element Method
FFT	Fast-Fourier-Transform
LS	Least Squares
LUT	Look-up-table
MIMO	Multi-Input-Multi-Output
MOSFET	Metal-Oxide-Semiconductor Field-Effect-Transistor
OEM	Original Equipment Manufacturer
PCB	Printed Circuit Board
PRBS	Pseudo Random Binary Sequence
PMSM	Permanent-Magnet Synchronous Motor
SISO	Single-Input-Single-Output

1 Introduction

The demand for deployment of electrical drives in automobiles has risen extensively throughout the last couple of years. This growing demand can be attributed to several reasons (see Figure 1.1).

Regulations concerning CO_2-emissions dictate an average maximum output of $130\,\mathrm{g\,km^{-1}}$
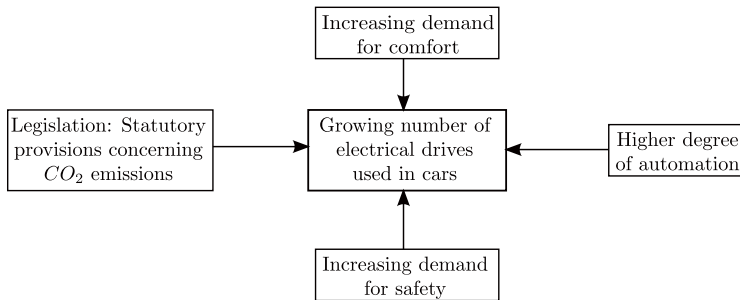
Figure 1.1: Reasons for growing number of electrical drives employed in cars

for the whole car fleet of a car manufacturer sold in 2015 (EU Regulation 443, 2009). A proposal was made by the European Union suggesting a further reduction of the CO_2-output to $95\,\mathrm{g\,km^{-1}}$ as of 2020 (EU Proposal, 2012), which is to be adopted in 2013 (Brünglinghaus and Winterhagen, 2011). CO_2-emissions are directly proportional to the fuel consumption, which necessitates a reduction of the fuel consumption to meet the statutory provisions. Besides using lightweight material for reduction of the car weight and downsizing the combustion engine, replacement of mechanically or hydraulically driven common auxiliaries with electrical drives shows a high potential for increasing the overall efficiency. Krebber-Hortmann et al. (2013) put forward the possibilities of further fuel reduction by using an electric camshaft phaser. Further examples include electrical fuel and water pumps, the steering and transmission actuators. Rau (2006) gives an overview of possible fields of application for electrical common auxiliaries and Schmidt (2003) has investigated measures which allow for an efficient management of all auxiliary devices.

Other reasons leading to an increase of small electrical drives employed in cars is the rising demand for comfort and safety. Nowadays, even small sized cars offer the possibility to purchase electric window lifters or seat actuators. Furthermore, due to EU Regulation 661 (2009), as of 2011, an Electronic Stability Control (ESC) system, which is relying on several small electrical actuators, is mandatory for all newly developed passenger cars in the European Union.

Besides comfort and safety aspects, the customers also demand a higher degree of automation. Examples for this include electric seat actuators with memory functions, dynamic headlight leveling and dynamic bend lighting.

In Figure 1.2, an overview of electrical drives employed in modern cars is given. The overview does not lay any claim to completeness, but rather serves to convey an impression about the large number of electrical drives used in the automotive area.
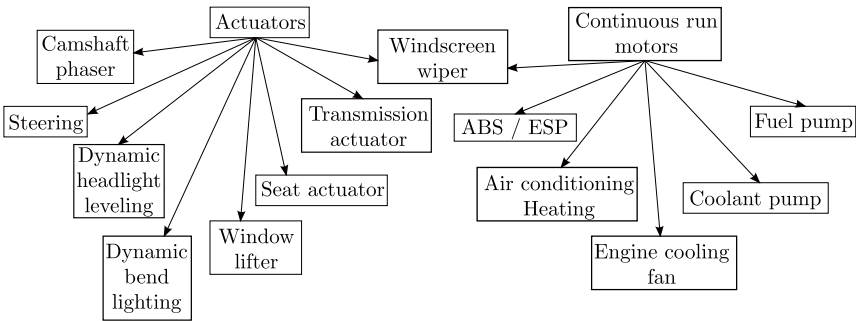
Figure 1.2: Overview of selected electric drives employed in cars

Due to this high penetration of small electrical drives, a reliable fault detection and diagnosis has gained a growing importance. Safety-critical applications are particularly in focus here, as failure of these devices can lead to hazardous situations. But also the applications that are not directly safety-related, such as auxiliary drives, demand a continuous health monitoring.
Malfunction or failure of the engine cooling fan or the coolant pump, e.g., can cause damage to the combustion engine due to overheating. Recognition of a failure in one of the auxiliary drives might prevent damage to the combustion engine. However, in most cases the car is not operational anymore and has to be towed. Early identification of prospective faults through a continuous health monitoring is thus necessary for a timely reaction.

Figure 1.3 depicts the association between the topic of fault detection and diagnosis and other fields of activity. As can be seen in the figure, the continuous online determination
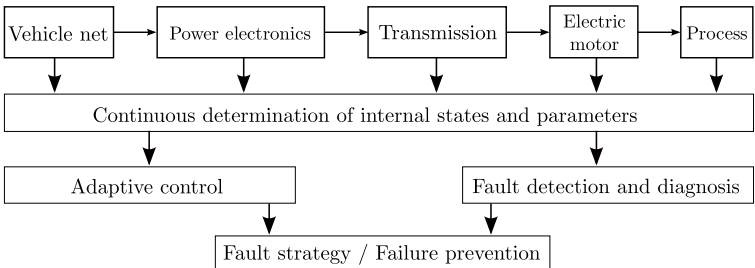
Figure 1.3: Association between topic of fault detection and diagnosis and other fields of activity

of internal states and parameters serves as a basis for both fault detection and diagnosis as well as for adaptive control. Due to component tolerances, wear and temperature dependencies, parameters of electrical drives change during runtime and over lifetime. Incorporating the knowledge about these changes in the control algorithm enables finetuning of the control according to the current conditions. Adaptive control and fault detection and diagnosis in turn are the foundation for implementation of efficient fault strategies and measures for an improvement of control and failure prevention.

1.1 State of the Art

The literature dealing with the topic of fault detection and diagnosis concerning electrical drives has gained considerable attention. Basic research in this area has been conducted by Höfling (1996) and Füssel (2002), who investigate different methods for fault detection and diagnosis using parameter estimation, parity equations and tree-structured neuro-fuzzy systems. Application of theses methods to the fault detection and diagnosis of motor vehicle actuators is examined by Pfeufer (1999) and Straky (2003). With focus on implementing the methods on a microcontroller, Moseler (2001) explores fault detection for an electromechanic actuator. Fault diagnosis of an asynchronous electrical machine is thoroughly investigated by Wolfram (2002), and Vetter (1988) examines the supervision of the heating behaviour of asynchronous machines.

Da et al. (2011), Henao et al. (2014) and Basak et al. (2006) give a brief overview of condition monitoring and fault diagnosis for certain types of electrical machines. They cover a wide range of possible faults, including electrical faults like stator interturn faults, faults concerning the permanent magnets and mechanical faults, such as eccentricity and bearing related faults.

Zhou et al. (2007) focus on bearing faults and describe several techniques relying on a frequency analysis of the stator current for bearing fault detection. Saadaoui and Jelassi (2011), Blodt et al. (2008) and Xie et al. (2012) give more details about the various stator current based techniques given in Zhou et al. (2007). The first two both rely on a spectral analysis of the stator current for diagnosing a bearing damage, whereas Xie et al. (2012) base their health assessment of a cooling fan bearing on a continuous wavelet transform and an autocorrelation function indicator.

Ebrahimi et al. (2010) present a method for detection of static and dynamic eccentricity faults under different load conditions. They evaluate frequencies of side-band components of the stator current, extract eccentricity signatures and use a support vector machine to predict the type and the degree of eccentricity. The same principle is applied by Ebrahimi et al. (2009). However, besides static and dynamic eccentricities, with their approach it is also possible to detect mixed-eccentricities.

A review of methods for detection of stator interturn faults is given in Gandhi et al. (2011). Techniques covered include signal analysis, model- as well as knowledge-based approaches. As for other areas of fault detection of electrical drives, analysis of the motor

current signature also plays a dominant role for detection of interturn faults and is thus the main focus of this paper. Krüger (2003) makes use of a model-based approach to detect a broken winding, a short circuit between two windings and between the winding and the housing.

Extensive application of both model- and signal-based approaches to different systems, such as an electrical throttle valve actuator or an electrical motor actuating the aircraft cabin pressure valve, is given in Isermann (2011).

1.2 Thesis Structure and New Contribution

Despite several publications for the fault detection and diagnosis of electrical drives, fault detection and diagnosis focusing on engine cooling fans is very scarce. The importance of these devices, however, has grown drastically in the last couple of years due to the demand for increasing capacity of thermal management systems. The engine cooling fan is a key component of such a system (see Chapter 3), as it delivers the required airflow for dissipating the heat contained in the coolant fluid to the surrounding air. Failure or malfunction of the cooling fan thus results in an overheating of the coolant fluids and the components being cooled by the fluids, such as the combustion engine.

The thesis at hand examines possibilities for fault detection and diagnosis for engine cooling fans. It focuses on the development of algorithms, which are application independent but are still able to reliably detect and diagnose faults and upcoming failures. The adaption of existing algorithms to new applications is very costly and requires extensive measurements and tuning on the test-bench. Eliminating the need for adaption is thus a key for reduction of the overall cost of a new application.

The market for small electrical drives employed in cars is highly competitive and cost-driven. The microcontrollers utilized in these drives therefore only offer a limited computing power and amount of memory. This, however, renders most of the methods described in the literature unsuitable for implementation, as they assume usage of a state-of-the-art controller, which offers far more resources than the one usually employed for small electrical drives. Even with increasing computing power and adoption of new controllers for small electrical drives, most of the methods covered in the current literature have to be adapted for implementation.

The new contribution of this work thus lies in the development of application independent algorithms, being able to detect and diagnose faults and impending failure for engine cooling fans, by taking into account the limited possibilities concerning signal injection and computing power. Another key issue is the consideration of thermal effects, adding the ability to the proposed methods for reliable operation under all operating conditions.

Figure 1.4 gives an overview of the topics covered in this work and outlines the most important parameters. As the contribution of this work is on the application independent development of algorithms suitable for fault detection and diagnosis, the focus is on the

| Vehicle net | Power electronics | Motor | Cooling fan | Engine cooling system |

Online parameter gathering

Parameters (Power electronics): R_{ESR}

Parameters (Motor):
- $R_{a,b,c}$
- $\frac{\partial \Psi}{\partial \varphi_{\mathrm{el}}}$
- $i_{a,b,c}$
- $u_{a,b,c}$

Parameters (Cooling fan):
- J
- $k_{\mathrm{fr0}}, k_{\mathrm{fr1}}$
- M_0, n_0

Parameters (Engine cooling system):
- p
- v_{car}
- ETD
- $\dot{W}_{\mathrm{air}}, \dot{W}_{\mathrm{cf}}$

Torque calculation — Loss calculation → P_1

LUT → $\vartheta_{\mathrm{cAir}}$

Calculation air density → ρ_{cAir}

Thermal network → ϑ_{R} ϑ_{S}

Affinity laws → M_{load}

Fault detection and diagnosis

Electrical subsystem	Electro-magnetic subsystem	Thermal subsystem	Mechanical subsystem
Aged capacitor Winding fault	Demagnetization	Overheat Winding Overheat Magnet	Blockage Dirt on blade Defect bearing

Figure 1.4: Overview of covered topics

machine independent determination of parameters and internal states. Only a few faults were thus selected for this work. The criteria for selection was based on faults not already covered in existing literature. Furthermore, faults were selected, which, according to company experts, constitute main reasons for the failure of engine cooling fans in the field.

The faults selected for investigation are displayed in Table 1.1. Along with the listed faults, three stages, which allow for fault detection and diagnosis, are introduced. First stage is the End-of-Line (EoL) of the supplier that produces the electrical drive, second stage is the EoL of the car manufacturer, where the whole cooling fan system consisting of the electrical motor and the fan is assembled in the engine compartment and the third stage constitutes normal operation of the engine cooling fan system in the car. Throughout this work it is investigated, if a suitable and reliable detection and diagnosis of the listed faults is possible at the corresponding stages and, which methods and parameters are required for detection and diagnosis. The completed table, which lists the possibilities for detecting and diagnosing the faults along with the required methods and parameters, can be found in Section 5.6.

Table 1.1: Investigated faults in this work. The required methods and parameters for detection and diagnosis of the selected faults are investigated throughout this work.

Subsystem	Fault	Parameters required for detection and diagnosis		
		EoL supplier	EoL car manufacturer	In the car
Electrical	Aged Capacitor			
	Winding fault			
Electro-magnetic	Demagnetization			
Thermal	Overheat Winding	Investigated throughout this work (See Table 5.8)		
	Overheat Magnet			
Mechanical	Blockage			
	Dirt on fan blade			
	Defect bearing			

The thesis at hand is structured as follows: The second chapter gives an overview of the methodology used for fault detection and diagnosis. Besides the topic of parameter estimation, which is covered in more detail, information is also given about parity equations and state observers. The chapter finishes by giving an overview of existing diagnosis methods and their specific advantages and disadvantages.

Chapter three outlines the structure of thermal management systems utilized in modern cars and gives an overview of the engine cooling fan prototype. It further gives a mathematical model for the electrical motor and the attached process, i.e. the airflow through the engine compartment. The simulation model and the test-bench, both used for evaluating the developed algorithms, are also described.

Chapter four outlines algorithms for online parameter gathering and constitutes the main part of this work. Methods for determination of the winding resistance, the flux linkage over angle and the equivalent series resistance are presented. Together with the thermal network for determination of the magnet temperature, which is also thoroughly covered in the fourth chapter, they serve as a basis for machine independent parametrization of the fault detection and diagnosis algorithms.

Chapter five exploits the algorithms and methods described in the preceding chapters to detect and diagnose the desired faults. It is structured according to the different subsystems, for which faults have been investigated.

The last chapter gives a summary of the whole work and a prospectus about future work useful to be undertaken.

2 Methods of Fault Detection and Diagnosis

This chapter gives an explanation of the terms detection and diagnosis along with a brief overview of the methods utilized for fault detection and diagnosis. As the field of fault detection and diagnosis has been the topic of many research activities, only the most important aspects will be presented here. For deeper coverage of this topic reference is made to the corresponding literature.

2.1 Fault Detection

Fault detection includes the generation of process features from measured signals and comparison of these features with reference values of the fault-free case (Wolfram, 2002). A symptom is the deviation of the generated features from the normal condition. A symptom with a value unequal to zero usually indicates a fault in the process.

A compilation of methods utilized for symptom generation based on Isermann (2006), Isermann (2011) and Pfeufer (1999) is illustrated in Figure 2.1.
In general, a distinction is made between direct and model-based methods. With the first one, symptoms are directly generated by evaluation of measured signals, whereas generation of symptoms with the latter one is based on process models. The direct methods
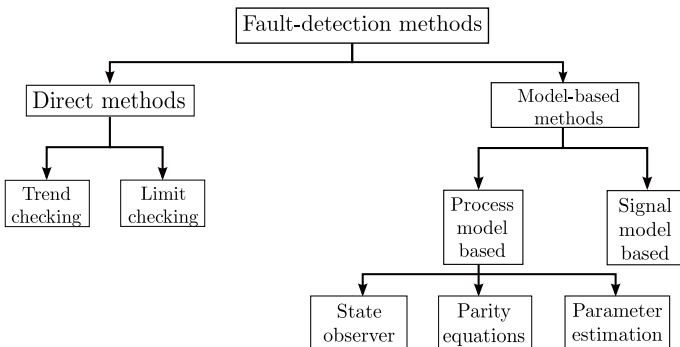

Figure 2.1: Overview of methods for symptom generation.

can be easily understood and applied and are therefore frequently used. However, they only react to large signal changes which make them unsuitable for detection of incipient faults (Wolfram, 2002). In comparison, the model-based approach allows for a deeper and broader surveillance of the process.

Model-based methods are based on a mathematical model of the system. The model can either describe a signal waveform or be based on the process itself, i.e. it models the relationship between input and output quantities. This model can provide additional information about the process, such as the reconstruction of process parameters or internal states. In the following, the main approaches based on process models used throughout this work are covered in more detail.

2.1.1 Parity Equations

Parity equations can be designed with transfer functions as well as in state-space notation. Based on a process model describing the behavior for the fault-free case, residuals are generated by comparison of measured process values with the model output (Isermann, 2011). Two different structures for residual generation with parity equations can be considered, as illustrated with transfer functions in Figure 2.2. The process is designated with F_p and the process model with F_m. The corresponding equation for the output error can
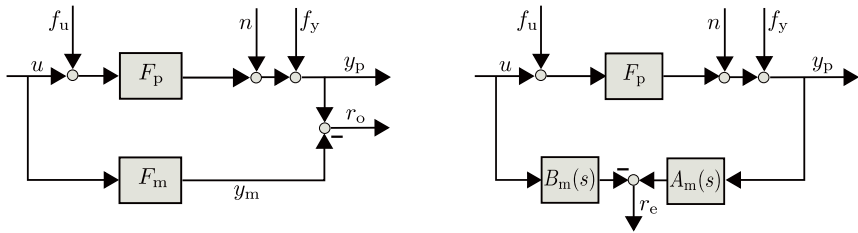
Figure 2.2: Residual generation with parity equations by using the output error (left) and the equation error (right). f_u and f_y are additive faults, n is noise.

be derived as

$$r_\mathrm{o}(s) = y_\mathrm{p}(s) - F_\mathrm{m}(s)u(s) = y_\mathrm{p}(s) - \frac{B_\mathrm{m}(s)}{A_\mathrm{m}(s)}u(s)\,, \tag{2.1}$$

and the equation error to

$$r_\mathrm{e}(s) = A_\mathrm{m}(s)y_\mathrm{p}(s) - B_\mathrm{m}(s)u(s)\,. \tag{2.2}$$

A comparison of (2.2) and (2.1) yields

$$r_\mathrm{e}(s) = A_\mathrm{m}(s)r_\mathrm{o}(s)\,. \tag{2.3}$$

The residual generated with the equation error thus includes derivatives of the signal of higher order. This can lead to an amplification of high frequent noise (Isermann, 2011). In contrast, when using the output error, additive faults will be detected with a delay due to the low-pass filtering effect of $\frac{1}{A_\mathrm{m}}$. In most cases however, this can be tolerated, which, besides being less prone to measurement noise, makes the output error structure being

the preferred choice for residual generation with parity equations (Wolfram, 2002). See Höfling (1996) for information about designing parity equations for state space models.

Parity equations are well suited for the detection of additive faults. Furthermore, their computational cost is very low and they do not require constant process excitation, making them ideally suited for online supervision of processes. Parity equations pose a disadvantage insofar, as they only allow for one residual being generated for each measurement signal, limiting information available for diagnosis.

2.1.2   State Observer

State observers are utilized for reconstruction of unmeasurable state variables by just using input and output signals (Föllinger et al., 2008; Isermann, 2006). It can both be used for Single-Input-Single-Output (SISO) and Multi-Input-Multi-Output (MIMO) systems, assuming they are observable. The general structure of the observer is illustrated in Figure 2.3. Based on Figure 2.3, the equations for the state observer can be derived as
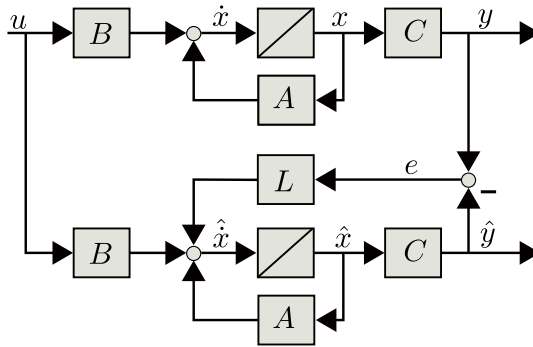
Figure 2.3: Process and state observer

$$\dot{\hat{\mathbf{x}}}(t) = \mathbf{A}\hat{\mathbf{x}}(t) + \mathbf{B}u(t) + \mathbf{L}e(t) \tag{2.4}$$
$$e(t) = y(t) - \hat{y}(t) \,. \tag{2.5}$$

Inserting (2.5) into (2.4) yields

$$\dot{\hat{\mathbf{x}}}(t) = (\mathbf{A} - \mathbf{LC})\,\hat{\mathbf{x}} + \mathbf{B}u(t) + \mathbf{L}y(t) \,, \tag{2.6}$$

with the dynamic matrix

$$\mathbf{G} = \mathbf{A} - \mathbf{LC} \,. \tag{2.7}$$

The matrix $\mathbf{L}$ is chosen such that the estimation error

$$\tilde{\mathbf{x}}(t) = \dot{\mathbf{x}}(t) - \dot{\hat{\mathbf{x}}}(t) \tag{2.8}$$

approaches zero for $t \to \infty$. This is the case, if the eigenvalues of the dynamic matrix $\mathbf{G}$ are positioned left in the s-plane (Föllinger et al., 2008). Several algorithms exist for proper design of the observer feedback matrix, e.g. pole placement or the usage of an optimality criterion (Föllinger et al., 2008; Lunze, 2008).

2.1.3   Parameter Estimation

Parameter estimation is an important technique for the field of fault detection and diagnosis as well as for any kind of adaptive control. It aims at identifying unknown process parameters by just measuring input and output signals. Compared to parity equations, parameter estimation is well suited for identification of multiplicative faults. Futhermore, depending on the number of parameters, it usually allows for the generation of more symptoms. Parameter estimation requires constant process excitation, making it best suited for End-of-Line (EoL) applications, as a predefined excitation signal can be applied to the process. For such a case, even small deviations from the normal behavior can be detected (Wolfram, 2002).

The underlying algorithm applied in this thesis is based on the Least Squares (LS) method. As the algorithm is well-researched and an in-depth discussion is given in many textbooks, only the most important aspects shall be presented here. The following subsections outline the fundamental principle behind the method of least squares, derive the recursive version, which is more suitable for online implementation, and explain an extension to the classic algorithm that is numerically more stable.

The Method of Least Squares

The method of least squares can be applied to discrete and continuous time processes. Throughout this work only continuous models are used. See Isermann and Münchhof (2011) for an application to discrete models.

To understand the principle of the least squares method, a continuous time-invariant differential equation is considered

$$a_{\mathrm{n}} y_{\mathrm{u}}^{(\mathrm{n})}(t) + a_{\mathrm{n}-1} y_{\mathrm{u}}^{(\mathrm{n}-1)}(t) + \ldots + a_1 y_{\mathrm{u}}^{(1)}(t) + y_{\mathrm{u}}(t) \tag{2.9}$$
$$= b_{\mathrm{m}} u^{(\mathrm{m})}(t) + b_{\mathrm{m}-1} u^{(\mathrm{m}-1)}(t) + \ldots + b_1 u^{(1)}(t) + b_0 u(t) \, ,$$

where $m < n$. It is assumed that the input and output signals can be measured, their derivatives exist and the initial values at $t = 0$ are zero. The transfer function of (2.9) is given as

$$F_p(s) = \frac{Y(s)}{U(s)} = \frac{b_0 + b_1 s + \ldots + b_{\mathrm{m}-1} s^{(m-1)} + b_{\mathrm{m}} s^{\mathrm{m}}}{1 + a_1 s + \ldots + a_{\mathrm{n}-1} s^{(n-1)} + a_{\mathrm{n}} s^{\mathrm{n}}} \, . \tag{2.10}$$

It is assumed that a normally distributed noise $n(t)$ is superimposed on the measurable output $y(t)$

$$y(t) = y_{\mathrm{u}}(t) + n(t) \, . \tag{2.11}$$

Substituting (2.11) into (2.9) and introducing an equation error $e(t)$ yields

$$y(t) = \boldsymbol{\psi}^T(t)\boldsymbol{\Theta} + e(t) \,, \tag{2.12}$$

with the data vector $\boldsymbol{\psi}(t)$ and the parameter vector $\boldsymbol{\Theta}$ (input and output quantities are separated by a vertical line for better readability)

$$\boldsymbol{\psi}^T(t) \;=\; \begin{bmatrix} -y^{(1)}(t) & \dots -y^{(n)}(t) & | & u(t) & \dots & u^{(m)}(t) \end{bmatrix} \tag{2.13}$$
$$\boldsymbol{\Theta}^T \;=\; \begin{bmatrix} a_1 & \dots & a_{\mathrm{n}} & | & b_0 & \dots & b_{\mathrm{m}} \end{bmatrix} . \tag{2.14}$$

Measuring the input and output signals at discrete-time intervals kT_0 with $k = 0, 1, 2, \dots, N$ with a sampling rate of T_0, and determining the corresponding derivatives results in $N+1$ equations of the form

$$y(k) = \boldsymbol{\psi}^T(k)\boldsymbol{\Theta} + e(k) \qquad \text{for } k = 0, 1, 2, \dots, N \,. \tag{2.15}$$

(2.15) can be written in Matrix notation as

$$\boldsymbol{y} = \boldsymbol{\Psi}\boldsymbol{\Theta} + \boldsymbol{e} \,, \tag{2.16}$$

with

$$\boldsymbol{y}^T \;=\; \begin{bmatrix} y(0) & y(1) & \dots & y(N) \end{bmatrix} \tag{2.17}$$
$$\boldsymbol{e}^T \;=\; \begin{bmatrix} e(0) & e(1) & \dots & e(N) \end{bmatrix} \tag{2.18}$$
$$\boldsymbol{\Psi} \;=\; \begin{bmatrix} -y^{(1)}(0) & \cdots & -y^{(\mathrm{n})}(0) & u(0) & \cdots & u^{(\mathrm{m})}(0) \\ \vdots & & \vdots & \vdots & & \vdots \\ -y^{(1)}(N) & \cdots & -y^{(\mathrm{n})}(N) & u(N) & \cdots & u^{(\mathrm{m})}(N) \end{bmatrix} . \tag{2.19}$$

The equation error therefore can be written as

$$\boldsymbol{e} = \boldsymbol{y} - \boldsymbol{\Psi}\boldsymbol{\Theta} \,. \tag{2.20}$$

The task is to find the parameters $\boldsymbol{\Theta}$ which best fit with N observations of the process output $\boldsymbol{y}$, i.e. minimizing the equation error $\boldsymbol{e}$. The LS method utilizes a quadratic cost function, i.e. it seeks to minimize the sum of the squared errors

$$V = e^2(1) + e^2(2) + \dots + e^2(N) = \boldsymbol{e}^T\boldsymbol{e} = \sum_{k=1}^{\mathrm{N}} \left(e(k) \right)^2 \,. \tag{2.21}$$

Isermann and Münchhof (2011) show that a quadratic cost function gives the same result as the maximum likelihood estimator, and that it shows the lowest variance for the parameter estimation error for normally distributed noise. The cost function is then given as

$$\begin{aligned} V \;&=\; (\boldsymbol{y} - \boldsymbol{\Psi}\boldsymbol{\Theta})^T(\boldsymbol{y} - \boldsymbol{\Psi}\boldsymbol{\Theta}) \\ &=\; \boldsymbol{y}^T\boldsymbol{y} - \boldsymbol{\Theta}^T\boldsymbol{\Psi}^T\boldsymbol{y} + \boldsymbol{\Theta}^T\boldsymbol{\Psi}^T\boldsymbol{\Psi}\boldsymbol{\Theta} - \boldsymbol{y}^T\boldsymbol{\Psi}\boldsymbol{\Theta} \,. \end{aligned} \tag{2.22}$$

The derivative of (2.22) with respect to the parameter $\boldsymbol{\Theta}$ yields

$$\frac{dV}{d\boldsymbol{\Theta}} = -2\boldsymbol{\Psi}^T(\boldsymbol{y} - \boldsymbol{\Psi}\boldsymbol{\Theta}) . \tag{2.23}$$

With the optimality criterion

$$\frac{dV}{d\boldsymbol{\Theta}}\mid_{\boldsymbol{\Theta} = \hat{\boldsymbol{\Theta}}} \overset{!}{=} 0 , \tag{2.24}$$

$\hat{\boldsymbol{\Theta}}$ can be determined as

$$\hat{\boldsymbol{\Theta}} = \left(\boldsymbol{\Psi}^T\boldsymbol{\Psi}\right)^{-1}\boldsymbol{\Psi}^T\boldsymbol{y} . \tag{2.25}$$

For a reliable parameter estimation the number of measurements N has to be significantly larger than the number n of parameters to be estimated. In practice this leads to a large data matrix $\boldsymbol{\Psi}$. As the calculation of the covariance matrix $\boldsymbol{P} = \left(\boldsymbol{\Psi}^T\boldsymbol{\Psi}\right)^{-1}$ requires a matrix inversion, the normal method of least squares is not suitable for online estimation due to the high calculation demand.

For online parameter estimation recursive versions of the normal least square algorithm have been developed. The algorithm presented in the next section determines a new parameter estimate $\hat{\boldsymbol{\Theta}}(k)$ for each time step based on old measurements and process data acquired at the current time interval k.

Recursive Least Squares Method

The parameter estimate at time step k is given as

$$\hat{\boldsymbol{\Theta}}(k) = \boldsymbol{P}(k)\boldsymbol{\Psi}^T(k)\boldsymbol{y}(k) , \tag{2.26}$$

with

$$\boldsymbol{P}(k) = \left(\boldsymbol{\Psi}^T(k)\boldsymbol{\Psi}(k)\right)^{-1} \tag{2.27}$$

$$\boldsymbol{y}(k) = \begin{pmatrix} y(1) \\ y(2) \\ \vdots \\ y(k) \end{pmatrix} \tag{2.28}$$

$$\boldsymbol{\Psi}(k) = \begin{pmatrix} \psi^T(1) \\ \psi^T(2) \\ \vdots \\ \psi^T(k) \end{pmatrix} . \tag{2.29}$$

Accordingly, $\hat{\boldsymbol{\Theta}}(k+1)$ at time step $k+1$ is given as

$$\hat{\boldsymbol{\Theta}}(k+1) = \boldsymbol{P}(k+1)\boldsymbol{\Psi}^T(k+1)\boldsymbol{y}(k+1) . \tag{2.30}$$

(2.30) can be split up and one obtains

$$
\begin{aligned}
\hat{\boldsymbol{\Theta}}(k+1) &= \boldsymbol{P}(k+1)\begin{pmatrix} \boldsymbol{\Psi}(k) \\ \boldsymbol{\psi}^T(k+1) \end{pmatrix}^T \begin{pmatrix} \boldsymbol{y}(k) \\ y(k+1) \end{pmatrix} \\
&= \boldsymbol{P}(k+1)\left(\boldsymbol{\Psi}^T(k)\boldsymbol{y}(k) + \boldsymbol{\psi}(k+1)y(k+1)\right).
\end{aligned}
\tag{2.31}
$$

(2.26) can be rephrased to

$$
\boldsymbol{\Psi}^T(k)\boldsymbol{y}(k) = \boldsymbol{P}^{-1}(k)\hat{\boldsymbol{\Theta}}(k).
\tag{2.32}
$$

Substituting (2.32) in (2.31) yields

$$
\begin{aligned}
\hat{\boldsymbol{\Theta}}(k+1) &= \boldsymbol{P}(k+1)\left(\boldsymbol{P}^{-1}(k)\hat{\boldsymbol{\Theta}}(k) + \boldsymbol{\psi}(k+1)y(k+1)\right) \\
&= \boldsymbol{P}(k+1)\boldsymbol{P}^{-1}(k)\hat{\boldsymbol{\Theta}}(k) + \boldsymbol{P}(k+1)\boldsymbol{\psi}(k+1)y(k+1) \\
&= \hat{\boldsymbol{\Theta}}(k) + \left(\boldsymbol{P}(k+1)\boldsymbol{P}^{-1}(k) - \boldsymbol{I}\right)\hat{\boldsymbol{\Theta}}(k) \\
&\quad + \boldsymbol{P}(k+1)\boldsymbol{\psi}(k+1)y(k+1).
\end{aligned}
\tag{2.33}
$$

From (2.27) it can be seen, that

$$
\begin{aligned}
\boldsymbol{P}(k+1) &= \left(\begin{pmatrix} \boldsymbol{\Psi}(k) \\ \boldsymbol{\psi}^T(k+1) \end{pmatrix}^T \begin{pmatrix} \boldsymbol{\Psi}(k) \\ \boldsymbol{\psi}^T(k+1) \end{pmatrix}\right)^{-1} \\
&= \left(\boldsymbol{\Psi}^T(k)\boldsymbol{\Psi}(k) + \boldsymbol{\psi}(k+1)\boldsymbol{\psi}^T(k+1)\right)^{-1} \\
&= \left(\boldsymbol{P}^{-1}(k) + \boldsymbol{\psi}(k+1)\boldsymbol{\psi}^T(k+1)\right)^{-1}.
\end{aligned}
\tag{2.34}
$$

From (2.34) it follows that

$$
\boldsymbol{P}^{-1}(k) = \boldsymbol{P}^{-1}(k+1) - \boldsymbol{\psi}(k+1)\boldsymbol{\psi}^T(k+1).
\tag{2.35}
$$

Substituting (2.35) in (2.33) finally yields the recursive version of the LS problem

$$
\begin{aligned}
\hat{\boldsymbol{\Theta}}(k+1) &= \hat{\boldsymbol{\Theta}}(k) + \left(\boldsymbol{P}(k+1)\left(\boldsymbol{P}^{-1}(k+1) - \boldsymbol{\psi}(k+1)\boldsymbol{\psi}^T(k+1)\right) - \boldsymbol{I}\right)\hat{\boldsymbol{\Theta}}(k) \\
&\quad + \boldsymbol{P}(k+1)\boldsymbol{\psi}(k+1)y(k+1)
\end{aligned}
\tag{2.36}
$$

$$
\begin{aligned}
&= \hat{\boldsymbol{\Theta}}(k) + \left(\boldsymbol{I} - \boldsymbol{P}(k+1)\boldsymbol{\psi}(k+1)\boldsymbol{\psi}^T(k+1) - \boldsymbol{I}\right)\hat{\boldsymbol{\Theta}}(k) \\
&\quad + \boldsymbol{P}(k+1)\boldsymbol{\psi}(k+1)y(k+1)
\end{aligned}
\tag{2.37}
$$

$$
\underbrace{\hat{\boldsymbol{\Theta}}(k+1)}_{\substack{\text{New parameter} \\ \text{estimate}}} = \underbrace{\hat{\boldsymbol{\Theta}}(k)}_{\substack{\text{Old parameter} \\ \text{estimate}}} + \underbrace{\boldsymbol{P}(k+1)\boldsymbol{\psi}(k+1)}_{\substack{\text{Correction} \\ \text{Vector}}}\cdot
\tag{2.38}
$$

$$
\cdot\left(\underbrace{y(k+1)}_{\substack{\text{New} \\ \text{measurement}}} - \underbrace{\boldsymbol{\psi}^T(k+1)\hat{\boldsymbol{\Theta}}(k)}_{\substack{\text{Predicted Measurement based on} \\ \text{last parameter estimate}}}\right).
$$

To avoid the matrix inversion to determine $\boldsymbol{P}^{-1}(k+1)$, the matrix inversion lemma is exploited which results in the three equations (Isermann and Münchhof, 2011)

$$\gamma(k) = \boldsymbol{P}(k+1)\boldsymbol{\psi}(k+1) = \frac{1}{\boldsymbol{\psi}^T(k+1)\boldsymbol{P}(k)\boldsymbol{\psi}(k+1)+1}\boldsymbol{P}(k)\boldsymbol{\psi}(k+1) \quad (2.39)$$

$$\hat{\boldsymbol{\Theta}}(k+1) = \hat{\boldsymbol{\Theta}}(k) + \gamma(k)\left(y(k+1) - \boldsymbol{\psi}^T(k+1)\hat{\boldsymbol{\Theta}}(k)\right) \quad (2.40)$$

$$\boldsymbol{P}(k+1) = \left(\boldsymbol{I} - \gamma(k)\boldsymbol{\psi}^T(k+1)\right)\boldsymbol{P}(k). \quad (2.41)$$

Initial values for $\boldsymbol{P}(0)$ and $\hat{\boldsymbol{\Theta}}(0)$ have to be set to start off with the recursive LS parameter estimation. For $\hat{\boldsymbol{\Theta}}(0)$ initial values should be assumed based on measurements or derived from physical coherences. Isermann and Münchhof (2011) recommend a choice of

$$P(0) = \zeta \boldsymbol{I}\,, \quad (2.42)$$

with ζ in the range of $100\ldots 10000$ and $\boldsymbol{I}$ the identity matrix. For slowly time-varying processes a forgetting factor λ, $0 < \lambda < 1$, can be introduced, which determines how strong the current data vector $\boldsymbol{\psi}(k)^T$ affects the new parameter estimate. Resulting equations can be found in Isermann and Münchhof (2011).

Both the normal least squares and the recursive least squares method can lead to significant errors in the parameter estimate. On the one hand, this can be attributed to a possible propagation of measurement errors in the determination of the covariance matrix $\boldsymbol{P}$. On the other hand, an oversampling of the process or an insufficient process excitation can lead to a set of measurement vectors that are strongly linear dependent. In the worst case, such an ill-conditioned matrix can be singular.
For improvement of the numerical stability, Isermann and Münchhof (2011) recommend the Discrete Square Root Filtering (DSFI) method, which avoids calculation of the covariance matrix by utilizing a orthogonality transformation for solving the estimation problem.

Discrete Square Root Filtering Method

Every matrix $\boldsymbol{A}$ can be transformed into the product of an orthogonal matrix $\boldsymbol{T}$ and an upper triangular matrix $\boldsymbol{S}$

$$\boldsymbol{A} = \boldsymbol{TS}\,, \quad (2.43)$$

with $\boldsymbol{T}$ the transformation matrix and $\boldsymbol{S}$ the upper triangular matrix. It can be shown that the condition number δ (see Appendix A) of the triangular matrix $\boldsymbol{S}$ satisfies

$$\delta(\boldsymbol{S}) \leq \delta(\boldsymbol{S}^T\boldsymbol{S}) = \delta^2(\boldsymbol{S}) = \delta(\boldsymbol{A})\,. \quad (2.44)$$

That means that the condition number of the square root of a given matrix is always better than the condition number of the matrix itself. If the transformation matrix $\boldsymbol{T}$ is chosen such, that

$$\boldsymbol{T\Psi} = \begin{bmatrix} \boldsymbol{S} \\ 0 \end{bmatrix} \quad (2.45)$$

and

$$\boldsymbol{T}\boldsymbol{y} = \begin{bmatrix} \boldsymbol{b} \\ \boldsymbol{e} \end{bmatrix} , \tag{2.46}$$

the non-recursive version can be derived by inserting (2.45) and (2.46) into (2.25), yielding

$$\boldsymbol{\Psi}^T \boldsymbol{T}^T \boldsymbol{T} \boldsymbol{\Psi} \hat{\boldsymbol{\Theta}} = \boldsymbol{\Psi}^T \boldsymbol{T}^T \boldsymbol{T} \boldsymbol{y} \tag{2.47}$$

$$\begin{bmatrix} \boldsymbol{S}^T & 0 \end{bmatrix} \begin{bmatrix} \boldsymbol{S} \\ 0 \end{bmatrix} \hat{\boldsymbol{\Theta}} = \begin{bmatrix} \boldsymbol{S}^T & 0 \end{bmatrix} \begin{bmatrix} \boldsymbol{b} \\ \boldsymbol{e} \end{bmatrix} \tag{2.48}$$

$$\boldsymbol{S}^T \boldsymbol{S} \hat{\boldsymbol{\Theta}} = \boldsymbol{S}^T \boldsymbol{b} \tag{2.49}$$

$$\boldsymbol{S} \hat{\boldsymbol{\Theta}} = \boldsymbol{b} . \tag{2.50}$$

The unknown parameters can now be calculated by simple back-substitution. A recursive version of the DSFI-algorithm can be derived by appending the newly acquired measurement vector at time step $k + 1$ to (2.50) given at time step k (Vetter, 1988):

$$\begin{bmatrix} \boldsymbol{S}(k) \\ \boldsymbol{\psi}^T(k+1) \end{bmatrix} \hat{\boldsymbol{\Theta}}(k+1) = \begin{bmatrix} \boldsymbol{b}(k) \\ y(k+1) . \end{bmatrix} \tag{2.51}$$

Applying the householder transformation $\boldsymbol{T}$ according to (2.45) and (2.46) to (2.51) yields the final equation for the DSFI-algorithm in its recursive version

$$\boldsymbol{S}(k+1)\hat{\boldsymbol{\Theta}}(k+1) = \boldsymbol{b}(k+1) . \tag{2.52}$$

Hence, an update of the parameter vector in each time step can easily be done by appending the new current measurement vector $\boldsymbol{\psi}^T(k + 1)$ to $\boldsymbol{S}(k)$ and the new output vector $y(k + 1)$ to $\boldsymbol{b}(k)$. After applying the householder transformation to the new vectors, $\hat{\boldsymbol{\Theta}}(k + 1)$ can be calculated by simple back-substitution.

2.2 Fault Diagnosis

Fault diagnosis aims at creating a relationship between detected faults and a predefined set of symptom patterns. Given enough symptoms, a specific and unique pattern can be determined for different faults. The pattern itself can either be determined by analytic observations or through experiments by artificially introducing faults (Pfeufer, 1999).

Figure 2.4 illustrates a compilation of selected methods for assigning a symptom vector to its corresponding fault vector (compilation based on Isermann, 2011, Pfeufer, 1999, Wolfram, 2002 and Füssel, 2002). The methods can be clustered into two major areas, classification and inference methods. Classification methods, also referred to as pattern matching methods, utilize an implicit knowledge base, whereas inference methods are based on explicit knowledge.

Characteristic for classification methods is, that the relationship between the symptom and the fault vector is learned based on gathered training data. Examples for methods assigning the symptom vector to a specific fault include neural networks, statistical methods
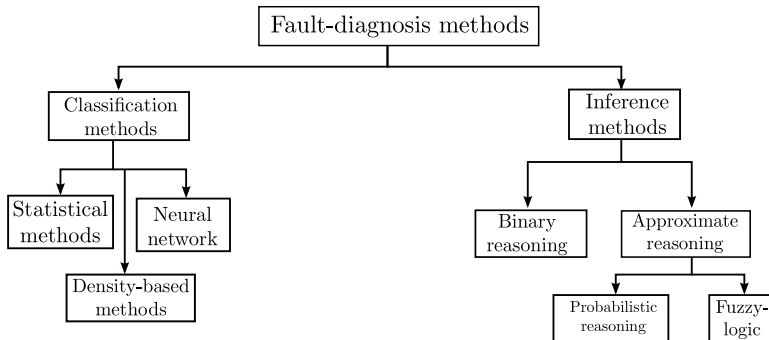
Figure 2.4: Overview of fault-diagnosis methods

and density-based methods. The latter one includes geometric methods, which evaluate the geometric distance from the symptom to the fault vector. The fault with the lowest distance measure is then selected. Statistical methods involve statistic data such as mean and variance. The Bayes-classifier, e.g., provides a conditional probability, that a symptom vector belongs to a specific fault. Pattern matching with neural networks is done by creating complex, nonlinear mapping rules. Their performance is strongly related to the number of neurons used and their linkage.

Inference methods are based on explicit knowledge, which can be described by fault-symptom trees. The fault-symptom connection is described in a qualitative manner, in the form of „if-then" relationships. Evaluation can be done with binary or approximate reasoning. The first one utilizes boolean algebra, i.e. the result can either be zero, meaning the fault is not present, or one, meaning the fault is present. This is a main disadvantage of binary reasoning, as it can not provide gradual information about the existence of a fault. This, however, is possible with approximate reasoning. When using probabilistic reasoning, each symptom is viewed as a statistic variable and is being assigned a corresponding probability. Evaluation can then be performed by using the Bayes formulas. Identification of a suitable probability distribution and determination of the parameters often poses problems, as Isermann (2006) points out. Fuzzy-logic allows for describing the symptoms in the form of membership functions. Result of the evaluation is a possibility grade for the specific fault, residing in the interval between zero and one. Compared to the probabilistic reasoning, fuzzy-logic is characterized by less design effort.

Advantageous about inference methods is the easy representation of knowledge in the form of „if-then" relationships. Due to this representation, additional faults can be amended to the existing rule base at any time. By contrast, rule generation for classification methods is based on implicit knowledge, making it in most cases difficult to interpret the automatically generated rule base. In most cases, an extension with additional faults is also not possible.

3 The Engine Cooling Fan System

Up to a few years ago, the main task of the engine cooling system was to protect components, like the combustion engine or the transmission, against overheating (Eilemann and Pantow, 2014). This has changed in the past years due to new and more strict requirements regarding fuel consumption and pollutant emissions with the challenge of bringing these requirements into conformity with an increased demand for air-conditioning comfort (Robert Bosch GmbH, 2011). One possibility for increasing the overall efficiency is the transition of the former mechanically driven engine cooling fan to one which is driven by an electrical drive. The output power delivered by the cooling fan is thus decoupled from the rotational speed of the combustion engine.

Furthermore, a popular method for reduction of fuel consumption is downsizing of the combustion engine, which is connected with a trend towards indirect charge air cooling. A shortening of the motor warm-up phase through a shutter and coolant standstill by closing shut-off valves is another effective approach for reducing fuel consumption (Edwards et al., 2008). Together with a cooled exhaust gas recirculation, which contributes to a decrease of the pollutant emission, this demands more cooling capacity, a higher efficiency and more intelligence by introduction of a thermal management.

Following this trend, engine cooling fans will become one of the main function components of an engine cooling system. This also entails rising requirements regarding reliability for engine cooling fans, which necessitates proper methods for fault detection and diagnosis being implemented in future drives.

A modern cooling system is very complex and can be assembled in a multitude of varieties. A schematic of a possible configuration is illustrated in Figure 3.1. The cooling module usually consists of a high temperature coolant radiator, a condensor for air-conditioning (not shown in Figure 3.1), the engine cooling fan and sealing against the surrounding environment (Sebastian et al., 2010). Depending on the type of car, the module can also be equipped with a low temperature coolant radiator. The engine cooling system, the engine oil and the exhaust gas recirculation are part of the high-temperature coolant loop, whereas the low temperature loop is composed of the transmission oil and the turbo charging air (Simonin et al., 2008).

The configuration possibilities for the assembly of the cooling module are depicted in Figure 3.2. Placing the cooling fan in front of the coolant radiators (upstream configuration) shows advantages in terms of cooling of the electric motor driving the fan, as it is only subjected to air with ambient temperature. Despite this benefit, the configuration preferred by most car manufacturer is placing the cooling fan behind the radiator (downstream configuration). Reasons are the decreased noise radiated to the passenger compartment (Walter, 2001) and regulations concerning pedestrian safety in case of a crash. The existence of both a down- and an upstream configuration entails a high multitude of different application variants, increasing the complexity of the development process of the engine
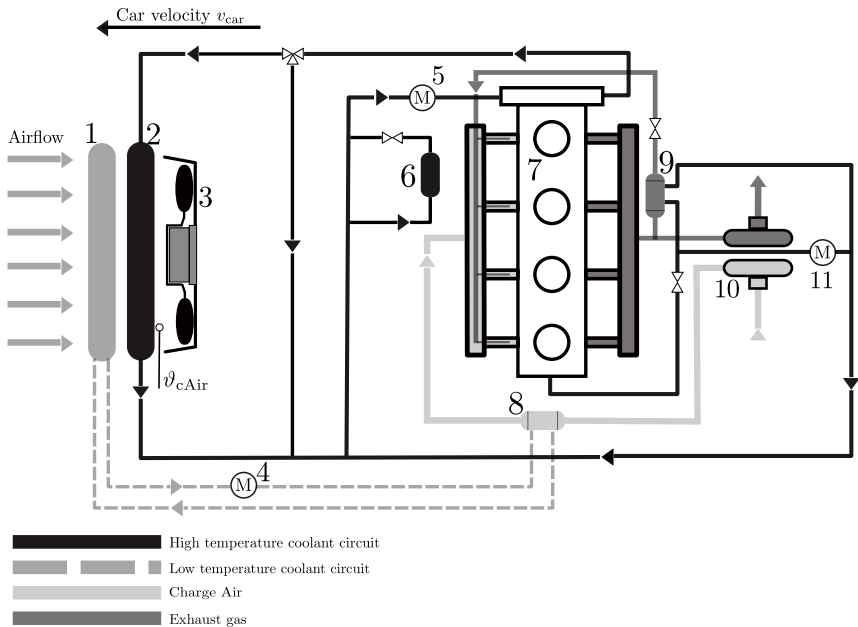
Figure 3.1: Possible setup of a cooling system, the heating circuit is not shown. 1: Low temperature coolant radiator, 2: High temperature coolant radiator, 3: Engine cooling fan, 4: Auxiliary coolant pump, 5: Main coolant pump, 6: Engine oil cooler, 7: Combustion engine, 8: Charge air cooler, 9: Exhaust gas recirculation cooler, 10: Turbocharger, 11: Auxiliary coolant pump.

cooling fan.

For subsequent examinations, however, it is always assumed, that the cooling fan is placed behind the radiator, i.e. the electric motor is exposed to ambient air, which is heated by the heat transfer from the radiator to the incoming air.

In this work, a recent Bosch engine cooling fan drive is used for evaluation of the developed algorithms (see Figure 3.3). Characteristics of the motor are shown in Table 3.1. It is a 3-phase, electronically commutated (EC) motor with ferrite permanent magnets assembled on the rotor, making it a permanent-magnet synchronous motor (PMSM). Electronically commutated means that the commutation of the motor current is not performed by a commutator or slip-ring but instead brushless by electronic power switches. The motor is built upon the external rotor design principle, i.e. the stator is in the inside and the rotor on the outside. A technical drawing showing the structure of the motor is illustrated in Figure 3.4. The material of the used permanent magnets is ferrite.

The drive is speed-contolled, however, due to cost reasons, the drive is not equipped with an incremental encoder. The rotational speed is determined by introduction of a
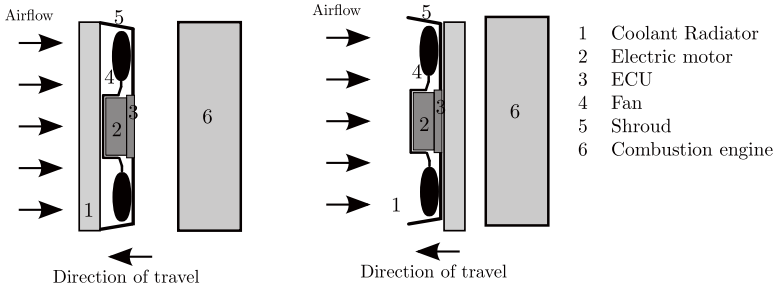
Airflow	1 Coolant Radiator
	2 Electric motor
	3 ECU
	4 Fan
	5 Shroud
	6 Combustion engine

Figure 3.2: Schematic view of downstream (left) and upstream (right) configuration of the engine cooling fan.

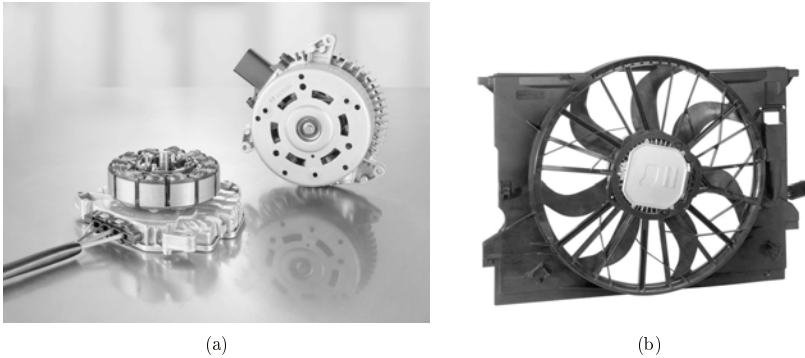(a)   (b)

Figure 3.3: Bosch motor used for evaluation of the developed algorithms. (a): rotor and stator. (b): assembled module. Source: Bosch media database.

blanking interval, i.e. a certain time interval during each electrical period the transistors connected to a certain phase are set open, leading to a current of zero in that phase. This allows for detection of the zero-crossing of the induced voltage. By evaluating the elapsed time between two consecutive zero-crossings of the induced voltage the rotational speed can be calculated. The electrical rotor angle is derived from the rotational speed by prediction. Future drives will implement an algorithm developed by Bosch, which allows for determination of the rotor angle and rotational speed without requiring a blanking interval. In this work, an incremental encoder or the blanking interval technique was utilized for acquisition of the rotational speed.

The electronic control unit (ECU) of the engine cooling fan is enclosed in a tightly sealed housing and directly attached to the stator. It is comprised of a three-phase inverter and an 8-bit microcontroller. To minimize the cost, the controller is only equipped with a fixed-point unit. A temperature sensor is mounted on the printed circuit board (PCB). Due to the limited computing power, the lack of a floating-point unit and the tight integration,
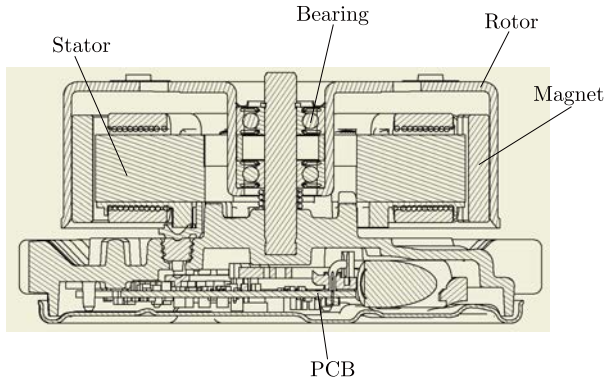
Figure 3.4: Technical drawing showing the structure of the used motor. Except the PCB, the motor is assembled on the test bench in this configuration. Not shown in the illustration: fan and shroud. Technical drawing provided by Robert Bosch GmbH.

which makes access to the signals on the PCB difficult, a different ECU and inverter were used throughout this work.

With the series ECU, only the bridge current i_{br} (see Figure 3.5) can be measured. It is assumed here, that future drives will have the possibility to measure all three phase currents, e.g. with the technique described by Lee et al. (2001), Marcetic and Adzic (2010) and Microchip (2009). On the test bench, current clamps connected to an oscilloscope were used for current measurement (see Section 3.2).

Table 3.1: Characteristics of used motor.

Output power	300 W or 400 W
Pole pair number	4
Self-inductivity per phase	116 μH
Absolute value of mutual inductivity per phase	57.7 μH
Resistance per phase at 25 °C	0.0394 Ω
Rotational range	$1000\,\mathrm{min}^{-1}$ to $3000\,\mathrm{min}^{-1}$
Load range	0.5 N m to 1.3 N m

The motor has some built-in supervision and health-monitoring capabilities. The motor is shut down if

- a blockage is detected,

- the vehicle net voltage violates allowed voltage ranges,

- the temperature measured with the sensor mounted on the PCB exceeds a certain threshold,

- the measured bridge current exceeds a certain threshold,

- internal electronic faults (such as an AD-conversion error or a fault in the bridge driver) are detected.

3.1   Mathematical model of the components of an electrically driven fan

In the following, models are derived for the electrical and the mechanical subsystem along with a model of the air path way through the engine compartment. The models serve as a basis for implementation of a simulation model, which was used for testing of the algorithms before implementation and evaluation on the test bench. The corresponding equations are derived in Section 3.1.1 to Section 3.1.4, the simulation model and its validation are presented in Section 3.1.5.

3.1.1   Electrical Subsystem

The electrical subsystem consists of the vehicle electrical system, a B6-bridge and the 3-phase motor (see Figure 3.5). The vehicle electrical system is modeled with one battery,
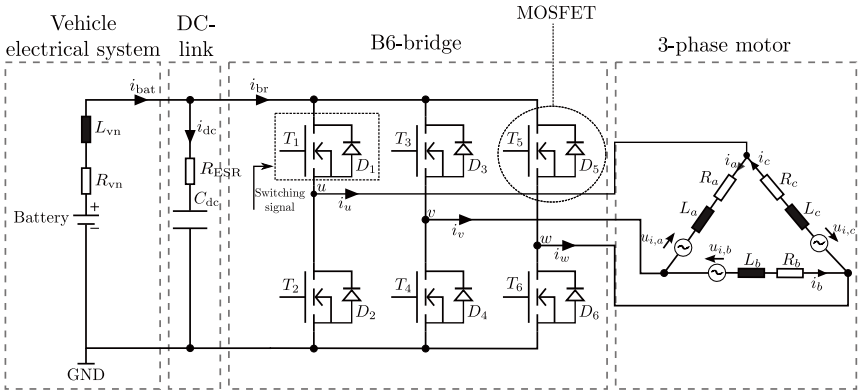

Figure 3.5: Electrical setup of engine cooling fan with battery supply

as described in Robert Bosch GmbH (2011) and by Fabis (2006). The supply cable from the battery to the Electronics Control Unit (ECU) of the cooling fan is modeled with a resistance and an inductance. Corresponding values are assumed to be $5\,\mathrm{m\Omega}$ for the resistance and $5\,\mathrm{\mu H}$ for the inductance.

The DC-link is modeled as a capacitor in series with a resistance (see Figure 3.5). For a detailed description of the DC-link capacitor and its model see Section 4.3.

The B6-bridge consists of three half-bridges, each composed of two Metal-Oxide-Semiconductor Field-Effect-Transistors (MOSFETs) with free-wheeling diodes. The MOS-FETs are designated by T_1 to T_6 in Figure 3.5. Connected to each MOSFET is a control line for transmission of the duty cycle issued by the microcontroller. For reasons of clarity only one of the control lines is shown in Figure 3.5.

The power losses of the B6-bridge can be split up into switching and conduction losses caused by the MOSFETs and the diodes. Calculation of these losses is performed according to Graovac et al. (2006). The conduction losses P_c are given as

$$P_{l,c} = P_{l,c,M} + P_{l,c,D} = R_{DSon}(i_{Mrms}, T_j, u_{GS})i_{Mrms}^2 + u_{D0}(T_j)i_{Drms} + R_D(i_{Drms})i_{Drms}^2 \,, \quad (3.1)$$

with $P_{l,c,M}$ and $P_{l,c,D}$ the conduction losses of the MOSFET and the diode, R_{DSon} the drain-source on-state resistance, i_{Mrms} the rms value of the MOSFET on-state current, T_j the junction temperature, u_{GS} the gate-source voltage, u_{D0} the zero-current voltage of the diode in on-state, R_D the diode on-state resistance and i_{Drms} the rms value of the diode current. The values for R_{DSon}, U_{GS}, u_{D0} and R_D can be extracted from the MOSFET data-sheet. The on-state resistance R_{DSon} of the MOSFET depends on the on-state current i_{Mrms} and is strongly temperature dependent. The temperature dependency has to be adjusted during simulation time according to the current junction temperature T_j of the MOSFET and is given as

$$R_{DSon}(T_j) = R_{DSon,max}(25\,°C) \left(1 + \frac{\gamma_{DSon}}{100}\right)^{(T_j - 298\,K)} \qquad T_j \text{ in K} \qquad (3.2)$$
$$\gamma_{DSon} \text{ in K}^{-1}$$

$R_{DSon,max}$ and the temperature coefficient γ_{DSon} can both be extracted from the datasheet. The switching losses of the MOSFET $P_{l,sw,M}$ and the diode $P_{l,sw,D}$ are composed of the switch-on energy loss of the MOSFET, $E_{on,M}$, and the switch-off energy loss of the MOS-FET, $E_{off,M}$, and the diode, $E_{off,D}$, yielding

$$P_{l,sw} = P_{l,sw,M} + P_{l,sw,D} = (E_{on,M} + E_{on,D} + E_{off,M})\, f_{sw} \,, \qquad (3.3)$$

with f_{sw} the switching frequency. The MOSFET switching losses are a function of the on-state current and several datasheet parameters, i.e. the gate resistance, gate-drain capacitance, the plateau voltage and current rise and fall times. To speed-up simulation time, an infinite slope was assumed for rise and fall of driving signals, voltages and currents. Calculation of the current rise and fall times depending on the operating condition can be found in Brown (2004). The switch-off energy loss of the diode can be calculated by taking the reverse recovery charge into account, which can also be found in the datasheet. For a typical operating point, the switching and conduction losses of the MOSFETs' comprise around 15 % of the total motor losses.

3.1.2 Electromagnetic Subsystem

For derivation of the equations of the electromagnetic subsystem consider Figure 3.6. It illustrates the structure of a motor with a pole pair number p of 4 and gives a definition

for the two used rotor angles. One rotation of the rotor corresponds to a complete cycle of the mechanical rotor angle φ_{rot} from $0°$ to $360°$. As can be seen in Figure 3.6, a complete cycle of the electrical rotor angle ranges over one pole pair. With the angular velocity ω defined as

$$\omega = \frac{\mathrm{d}\varphi}{\mathrm{d}t}\,, \tag{3.4}$$

the relationship between the mechanical and the electrical angular velocity yields

$$\omega_{\mathrm{el}} = p\omega_{\mathrm{rot}}\,. \tag{3.5}$$

With a pole pair number of $p = 4$, the electrical rotor frequency is thus four times higher than the mechanical rotor frequency.

The model of the electromagnetic subsystem is based on the voltage equations for each
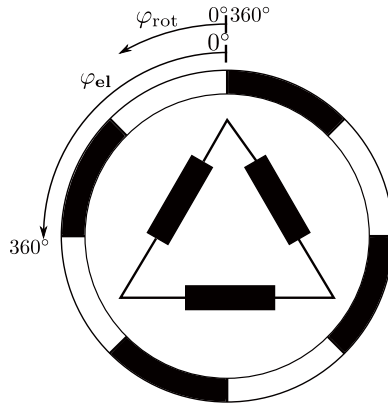

Figure 3.6: Structure of motor with four pole pairs

of the three phases. Taking a phase k, the equation yields

$$k : a, b, c \qquad\qquad u_k = R_k i_k + \frac{\mathrm{d}\Psi_k}{\mathrm{d}t}\,. \tag{3.6}$$

According to the induction law, the induced voltage in each phase is caused by a change of the flux linkage Ψ. This change can be attributed to a change of the electrical rotor position $\mathrm{d}\varphi_{\mathrm{el}}$ or a change in current $\mathrm{d}i$. Assuming a linear system, the total flux linkage seen by a phase can be described by a superposition of the flux generated by the stator with the flux generated by the rotor as

$$\Psi_k = \Psi_{k,\mathrm{S}} + \Psi_{k,\mathrm{R}}\,. \tag{3.7}$$

The induced voltage can then be written as

$$\begin{aligned} u_{\mathrm{i},k} &= -\frac{\mathrm{d}\Psi_k}{\mathrm{d}t} = -\frac{\partial\Psi_k}{\partial\varphi_{\mathrm{el}}}\frac{\mathrm{d}\varphi_{\mathrm{el}}}{\mathrm{d}t} - \sum_{j=a,b,c}\frac{\partial\Psi_k}{\partial i_j}\frac{\mathrm{d}i_j}{\mathrm{d}t} \\ &= -\left(\frac{\partial\Psi_{k,\mathrm{S}}}{\partial\varphi_{\mathrm{el}}} + \frac{\partial\Psi_{k,\mathrm{R}}}{\partial\varphi_{\mathrm{el}}}\right)\frac{\mathrm{d}\varphi_{\mathrm{el}}}{\mathrm{d}t} - \sum_{j=a,b,c}\left(\frac{\partial\Psi_{k,\mathrm{S}}}{\partial i_j} + \frac{\partial\Psi_{k,\mathrm{R}}}{\partial i_j}\right)\frac{\mathrm{d}i_j}{\mathrm{d}t}\,. \end{aligned} \tag{3.8}$$

The flux $\Psi_{k,\mathrm{R}}$ is generated by the permanent magnets, so it is not depending on the current. Due to the cylindrical shape of the motor, the flux $\Psi_{k,\mathrm{S}}$ does not depend on the current rotor angle (Krüger, 2003). The corresponding derivations can thus be set to zero.

$$\frac{\partial \Psi_{k,\mathrm{R}}}{\partial i_j} = 0 \tag{3.9}$$

$$\frac{\partial \Psi_{k,\mathrm{S}}}{\partial \varphi_{\mathrm{el}}} = 0 \,. \tag{3.10}$$

Assuming further, that the permeability of the iron core is constant, the inductivities

$$L_{k,j} = \frac{\partial \Psi_{k,\mathrm{S}}}{\partial i_j} \tag{3.11}$$

have the same value. Taking (3.8) to (3.11) into account, (3.8) can be rewritten as

$$u_{\mathrm{i},k} = -\left(\frac{\partial \Psi_{k,\mathrm{R}}}{\partial \varphi_{\mathrm{el}}}\right) \frac{\mathrm{d}\varphi_{\mathrm{el}}}{\mathrm{d}t} - \sum_{j=a,b,c} \left(\frac{\partial \Psi_{k,\mathrm{S}}}{\partial i_{\mathrm{j}}}\right) \frac{\mathrm{d}i_j}{\mathrm{d}t} \,, \tag{3.12}$$

and (3.6) as

$$u_k = R_k i_k - u_{\mathrm{i},k} \,. \tag{3.13}$$

The electrical input power of a three-phase electrical machine is defined as

$$P_{\mathrm{el}} = \sum_{k=a,b,c} u_k i_k \,. \tag{3.14}$$

Applying (3.14) to (3.6) yields

$$P_{\mathrm{el}} = \sum_{k=a,b,c} \left(R_k i_k + \frac{\partial \Psi_{k,\mathrm{R}}}{\partial \varphi_{\mathrm{el}}} \frac{\mathrm{d}\varphi_{\mathrm{el}}}{\mathrm{d}t} + \sum_{j=a,b,c} \frac{\partial \Psi_{k,\mathrm{S}}}{\partial i_j} \frac{\mathrm{d}i_j}{\mathrm{d}t} \right) i_k \,. \tag{3.15}$$

The electrical power as defined in (3.15) can be split up into mechanical power P_{mech}, winding power losses P_{winding} and inductive power P_{ind} according to

$$P_{\mathrm{el}} = \underbrace{\sum_{k=a,b,c} R_k i_k^2}_{P_{\mathrm{winding}}} + \underbrace{\sum_{k=a,b,c} \frac{\partial \Psi_{k,\mathrm{R}}}{\partial \varphi_{\mathrm{el}}} \frac{\mathrm{d}\varphi_{\mathrm{el}}}{\mathrm{d}t} i_k}_{P_{\mathrm{mech}}} + \underbrace{\sum_{k=a,b,c} \sum_{j=a,b,c} \frac{\partial \Psi_{k,\mathrm{S}}}{\partial i_j} \frac{\mathrm{d}i_j}{\mathrm{d}t} i_k}_{P_{\mathrm{ind}}} \,. \tag{3.16}$$

Given the definition of mechanical power

$$P_{\mathrm{mech}} = M_{\mathrm{mot}} \omega_{\mathrm{rot}} \,, \tag{3.17}$$

with M_{mot} the torque delivered by the electrical machine and ω_{rot} the angular rotor velocity. Substituting

$$\frac{\mathrm{d}\varphi_{\mathrm{el}}}{\mathrm{d}t} = \omega_{\mathrm{el}} \tag{3.18}$$

in (3.16) and utilizing (3.5), the torque delivered by the electric motor can be derived as

$$M_{\mathrm{mot}} = p \sum_{k=a,b,c} \frac{\partial \Psi_{k,\mathrm{R}}}{\partial \varphi_{\mathrm{el}}} i_k \,. \tag{3.19}$$

The flux generated by the permanent magnets is depending on the current magnet temperature. Ferrite magnets have a negative temperature coefficient γ_{br} of $-0.2\,\%\,\mathrm{K}^{-1}$. The alternating field of the permanent magnets leads to a change in magnetization direction and thus results in hysteresis losses when traveling around the hysteresis loop. In addition, the field induces voltages in the iron core. The resulting eddy currents generate losses, too. The iron losses are thus composed of

$$P_{\mathrm{l,iron}} = P_{\mathrm{l,eddy}} + P_{\mathrm{l,hys}}\,. \tag{3.20}$$

According to Pyrhönen et al. (2008), eddy current and hysteresis losses can be approximated by

$$P_{\mathrm{hys}} = k_{\mathrm{hys}}\omega_{\mathrm{el}} \tag{3.21}$$

$$P_{\mathrm{eddy}} = k_{\mathrm{eddy}}\omega_{\mathrm{el}}^2\,, \tag{3.22}$$

with ω_{el} the electrical angular velocity. Using the relationship $P = \omega M$ yields

$$M_{\mathrm{r,hys}} \propto 1 \tag{3.23}$$

$$M_{\mathrm{r,eddy}} \propto f_{\mathrm{el}}\,. \tag{3.24}$$

with $M_{\mathrm{r,hys}}$ and $M_{\mathrm{r,eddy}}$ the braking torque caused by the hysteresis and eddy current losses due to the rotating permanent magnet rotor, respectively. As both the hysteresis and the eddy losses are caused by the alternating field of the rotating permanent magnets, the iron losses are lumped together and have to be adapted to a change in the magnet temperature according to

$$P_{\mathrm{l,iron}}(T_{\mathrm{mag}}) = \left(1 - (T_{\mathrm{mag}} - T_0)\gamma_{\mathrm{br}}\right)P_{\mathrm{iron}}(T_0) = \beta(T_{\mathrm{mag}})P_{\mathrm{iron}}(T_0)\,, \tag{3.25}$$

with T_{mag} the magnet temperature and T_0 the reference temperature.

3.1.3 Mechanical Subsystem

The mechanical part of the engine cooling fan is fully described by the equation of motion as

$$J\dot{\omega}_{\mathrm{rot}} = M_{\mathrm{mot}} - \left(M_{\mathrm{load}} + M_{\mathrm{fr,bearing}} + M_{\mathrm{r,iron}}\right)\,, \tag{3.26}$$

with M_{mot} the torque generated by the electrical machine (see (3.19)), M_{load} the load torque induced by the rotating fan due to the air movement (see Section 3.1.4), $M_{\mathrm{fr,bearing}}$ the friction torque of the bearing and $M_{\mathrm{r,iron}}$ the braking torque caused by rotational iron losses. The friction torque generated by the bearing is assumed to be temperature independent and can be modeled as (Isermann, 2008)

$$M_{\mathrm{fr,bearing}} = k_{\mathrm{b0}}\,\mathrm{sgn}\,\omega_{\mathrm{rot}} + k_{\mathrm{b1}}\omega_{\mathrm{rot}} + k_{\mathrm{b3}}\omega_{\mathrm{rot}}^3\,. \tag{3.27}$$

If only a small part of the speed range covered by the bearing is considered, the factor k_{b3} can be set to zero. Rotational iron losses and bearing losses of the engine cooling
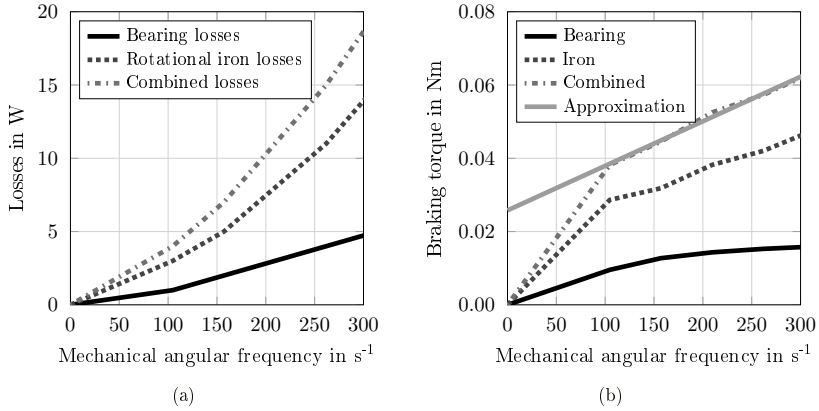
Figure 3.7: Calculated rotational iron losses and measured bearing losses and resulting braking torque for used motor. (a) Losses, (b) Braking torque

fan motor used throughout this work are depicted in Figure 3.7. For the diagram given, a motor with no load attached, i.e. in idle condition, was operated on a test-bench. In steady-state, (3.26) thus becomes

$$M_{\text{mot}} = M_{\text{r,total}} = M_{\text{fr,bearing}} + M_{\text{r,iron}} . \tag{3.28}$$

For the given configuration, the measured motor torque equals the total braking torque generated by bearing and rotational iron losses. Additionally, only the bearing torque was measured by disconnecting the stator from the shaft. The braking torque generated by rotational iron losses was then calculated with

$$M_{\text{r,iron}} = M_{\text{r,total}} - M_{\text{fr,bearing}} . \tag{3.29}$$

As can be seen from Figure 3.7, above an electrical angular frequency of $100\,\text{s}^{-1}$, the total braking torque caused by bearing and rotational iron losses can be well approximated with a straight line yielding

$$M_{\text{r,total}} = k_{\text{r,hys}} + (k_{\text{fr,bearing}} + k_{\text{r,eddy}})\omega_{\text{rot}} . \tag{3.30}$$

Substituting (3.30) in (3.26) yields

$$M_{\text{mot}} = J\dot{\omega}_{\text{rot}} + M_{\text{load}} + M_{\text{fr,bearing}} + M_{\text{r,iron}} \tag{3.31}$$

$$= J\dot{\omega}_{\text{rot}} + M_{\text{load}} + k_{\text{b0}} \operatorname{sgn}\omega_{\text{rot}} + k_{\text{b1}}\omega_{\text{rot}} + k_{\text{r,iron}}\omega_{\text{rot}} \tag{3.32}$$

For subsequent considerations, the friction and braking coefficients are lumped together as

$$k_{\text{fr0}} = k_{\text{b0}} \tag{3.33}$$

$$k_{\text{fr1}} = k_{\text{b1}} + k_{\text{r,iron}} \tag{3.34}$$

3.1.4   Air Pathway in the Engine Compartment

The cooling system of a modern car usually consists of a cooler, one or more condensers, a cooling fan and a water pump circulating the cooling liquid. A common setup used by many car manufacturers is to assemble the condenser and the cooler into one unit and to place it at the front of the engine compartment to allow for air circulation when the car is moving. The cooling fan is usually situated behind the cooler and ensures a sufficient air flow for cooling, in case the car is not moving fast enough or is not moving at all. The described setup including the air pathway is depicted in Figure 3.8.

 According to Straßer (1990), for the given constellation a Mach-number of
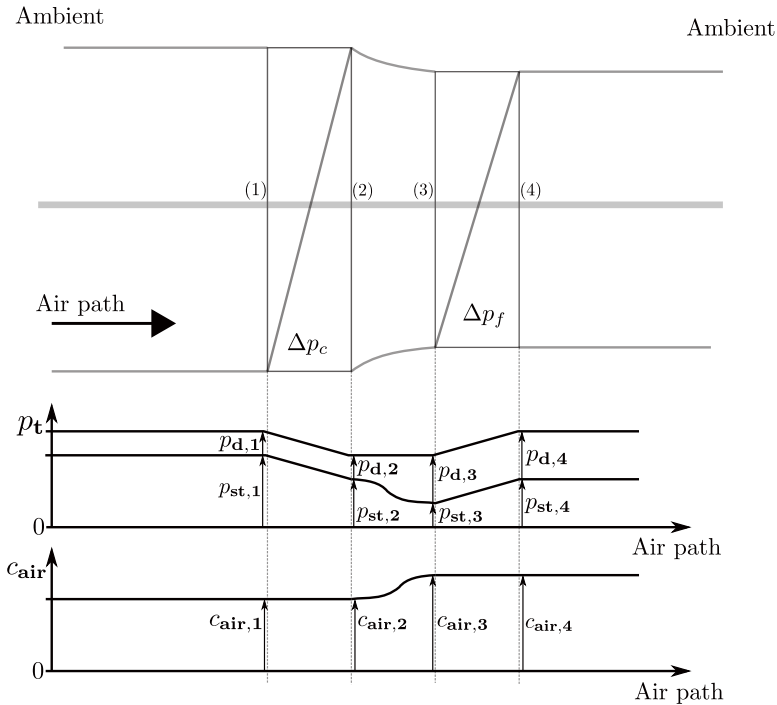
Figure 3.8: Setup of cooling system with development of pressure and air velocity in the air path

$$Ma \leq 0.3 \qquad\qquad\qquad (3.35)$$

can be assumed. The air flow can thus be assumed to be incompressible. Given a constant volume, Bernoulli's law states, that with $\rho = \text{const.}$ and no external energy supplied, the

total pressure stays constant, yielding

$$p_t = p_{st} + p_d = p_{st} + \frac{\rho}{2}c_{air}^2 = \text{const.}, \tag{3.36}$$

with p_{st} the static pressure, p_d the dynamic pressure, c_{air} the velocity of the air flowing through and ρ the air mass density. Applying this law to the setup depicted in Figure 3.8, one can derive the following equations:

$$(1) \qquad p_{t,1} = p_{st,1} + p_{d,1} = p_{st,1} + \frac{\rho}{2}c_{air,1}^2 \tag{3.37}$$

$$(2) \qquad p_{t,2} = p_{st,2} + p_{d,2} = p_{st,2} + \frac{\rho}{2}c_{air,2}^2 = p_{st,1} - \Delta p_c \tag{3.38}$$

$$(3) \qquad p_{t,3} = p_{st,3} + p_{d,3} = p_{st,3} + \frac{\rho}{2}c_{air,3}^2 = p_{t,2} \tag{3.39}$$

$$(4) \qquad p_{t,4} = p_{st,4} + p_{d,4} = p_{st,4} + \frac{\rho}{2}c_{air,4}^2 = p_{t,3} + \Delta p_f, \tag{3.40}$$

with Δp_f the pressure rise across the fan (delivery head) and Δp_c the pressure drop across the cooler. The total pressure $p_{t,1}$ before the cooler equals the total pressure $p_{t,4}$ behind the fan, yielding

$$\Delta p_c = \Delta p_f. \tag{3.41}$$

The fan thus compensates for the pressure loss induced by the cooler and other flow resistances in the engine compartment. With a car velocity greater than zero an additional dynamic pressure, $p_{v,car} = \frac{\rho}{2}v_{car}^2$, is present in the system, and (3.37) now yields

$$(1) \qquad p_{t,1} = p_{st,1} + p_{d,1} + p_{v,car} = p_{st,1} + \frac{\rho}{2}c_{air,1}^2 + \frac{\rho}{2}v_{car}^2. \tag{3.42}$$

(3.41) then becomes

$$\Delta p_c - p_{v,car} = \Delta p_f. \tag{3.43}$$

The pressure induced by the car velocity thus supports the fan, i.e. the pressure difference, which the fan has to generate for compensation of the pressure loss caused by the cooler, is lower, compared to the case when the car velocity v_{car} is zero.

Affinity Laws

To account for new applications, it is often required to adapt a known fan geometry to a new one with different diameter D or different liquid properties to be conveyed, such as the mass density ρ. This can easily be achieved with dimensionless numbers leading to so-called affinity laws. These laws not only allow for easy adaption of known fans to ones with different geometry or changed liquid properties, but also for simple load calculation for the current operating point based on reference values. The affinity laws stated here are used for the software implementation of the engine cooling fan model and for symptom creation (see Section 5.4). Only the equations necessary throughout this work shall be given here, for a detailed derivation of the equations based on the continuum and the

Euler-equation see Schlender and Klingenberg (1996). The equations for torque M and pressure drop Δp_{f} are given by

$$M = \frac{\rho_0}{\rho} \cdot \left(\frac{n}{n_0}\right)^2 \cdot \left(\frac{D}{D_0}\right)^2 \cdot M_0 \tag{3.44}$$

$$\Delta p_{\mathrm{f}} = \Delta p_{\mathrm{f},0} \cdot \left(\frac{n}{n_0}\right)^2 \cdot \left(\frac{D}{D_0}\right)^2 \cdot \frac{\rho}{\rho_0} \,. \tag{3.45}$$

Please note that quantities marked with the subscript $_0$ are reference quantities $(M_0, n_0, \rho_0, \Delta p_{\mathrm{f},0}, D_0)$ which have to be acquired by measurement.

Measuring the load torque M for a given rotational speed n and mass density ρ respectively, thus allows for easy calculation of the load for different rotational speeds. This coherence is used for predicting the load induced by an healthy system at a given rotational speed. For correct rescaling of the reference torque to the current operating point using (3.44), the air mass density ρ is required, which depends on the ambient pressure p_{a}, the absolute temperature T_{cAir} and the humidity of the air. Considering air as an ideal gas, the air density can be calculated as

$$\rho = \frac{p_{\mathrm{a}}}{R_{\mathrm{a,d}} T_{\mathrm{cAir}}} \,, \tag{3.46}$$

with $R_{a,d} = 287.085 \, \mathrm{J\,kg^{-1}\,K^{-1}}$ the gas constant for dry air, p_{a} and T_{cAir} the current air pressure and absolute temperature (in K) of the air. Taking the air humidity into consideration leads to

$$\rho = \frac{p_{\mathrm{a}}}{R_{\mathrm{a,m}} T_{\mathrm{cAir}}} \,, \tag{3.47}$$

with

$$R_{\mathrm{a,m}} = \frac{R_{\mathrm{a,d}}}{1 - \xi \frac{p_{\mathrm{s}}}{p_{\mathrm{a}}} \left(1 - \frac{R_{\mathrm{a,d}}}{R_{\mathrm{v}}}\right)} \,. \tag{3.48}$$

In (3.48) the gas constant of water vapour is designated as $R_{\mathrm{v}} = 461 \, \mathrm{J\,kg^{-1}\,K^{-1}}$, ξ is the relative humidity and p_{s} is the saturated vapour pressure. According to Schlender and Klingenberg (1996), p_{s} (in Pa) can be approximated with the Antoine equation in a region between $0\,^{\circ}\mathrm{C}$ to $100\,^{\circ}\mathrm{C}$ as

$$p_{\mathrm{s}} = 10^{\left(A - \frac{B}{C + T_{\mathrm{cAir}}}\right)} p_{\mathrm{u}} \,, \tag{3.49}$$

with $A = 10.1962$, $B = 1731\,\mathrm{K}$, $C = -39.724\,\mathrm{K}$, T_{cAir} the absolute air temperature in K and $p_{\mathrm{u}} = 1\,\mathrm{Pa}$. The specified temperature range for the engine cooling fan is between $-40\,^{\circ}\mathrm{C}$ and $120\,^{\circ}\mathrm{C}$. Although the equation given in (3.49) is only valid for a smaller temperature range, the error made when extending the range to $-40\,^{\circ}\mathrm{C}$ and $120\,^{\circ}\mathrm{C}$ can be neglected.

The air temperature behind the cooler is an important quantity, which is not only required for the above mentioned air density calculation, but it is also indispensable for a reliable operation of the thermal network covered in Section 4.4. With knowledge of the cooling system, an average air temperature behind the cooler can be calculated, as it is described in the next section.

Calculation of the Air Temperature Behind the Cooler

Accurate calculation of the current load seen by the engine cooling fan according to (3.44) requires knowledge of the air temperature behind the cooler/condensor system. This temperature is usually not directly measured, but, taking some simplifications into account, can be calculated and provided to the engine cooling fan drive by the car manufacturer. Only a brief overview of the calculation method and the required parameters shall be given here. For a detailed discussion and derivation of the given equations see Baehr and Stephan (2013). In order to calculate the air exit temperature of one cross-flow heat exchanger, the following quantities have to be known:

- The air entry temperature $\vartheta_{\mathrm{air,in}}$, the entry and output temperature of the coolant fluid $\vartheta_{\mathrm{cf,in}}$ and $\vartheta_{\mathrm{cf,out}}$. It is assumed here that these quantities are measured.

- The „heat capacity flow" of the air and the coolant fluid

$$\dot{W}_{\mathrm{air}} = \dot{m}_{\mathrm{air}} c_{\mathrm{p,air}} \tag{3.50}$$

$$\dot{W}_{\mathrm{cf}} = \dot{m}_{\mathrm{cf}} c_{\mathrm{p,cf}} \,, \tag{3.51}$$

  with $\dot{m}$ the mass flow and c_{p} the specific heat capacity of the air at constant pressure, respectively of the coolant fluid. The mass flow $\dot{m}_{\mathrm{air}}$ is a function of the current car velocity v_{car}, the air temperature and the rotational speed of the engine cooling fan. The mass flow $\dot{m}_{\mathrm{cf}}$ is a function of the rotational speed of the combustion engine and the coolant fluid temperature. Determination of the air and the coolant fluid mass flow rate is too complex for online-calculation in the car, but both can be pre-calculated and approximated by a characteristic map.
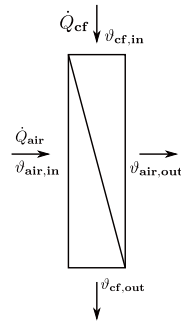

Figure 3.9: Heat flows and temperatures for cross-flow heat exchanger

Assuming a stationary behavior and given these parameters, the heat transferred by a cross-flow heat exchanger can be calculated with the heat-flow balance (see Figure 3.9)

$$\dot{Q}_{\mathrm{air}} = \dot{Q}_{\mathrm{cf}} \,. \tag{3.52}$$

From (3.52) it follows, that

$$\dot{W}_{\text{air}} \cdot (\vartheta_{\text{air,out}} - \vartheta_{\text{air,in}}) = \dot{W}_{\text{cf}} \cdot (\vartheta_{\text{cf,in}} - \vartheta_{\text{cf,out}}) \ , \tag{3.53}$$

which yields for the air exit temperature

$$\vartheta_{\text{air,out}} = \vartheta_{\text{air,in}} + \frac{\dot{W}_{\text{cf}}}{\dot{W}_{\text{air}}} \cdot (\vartheta_{\text{cf,in}} - \vartheta_{\text{cf,out}}) \ . \tag{3.54}$$

It has to be noted that the equations given above are only valid for one cross-flow heat exchanger and (3.54) only gives an averaged air outside temperature $\vartheta_{\text{air,out}}$.

Software Implementation

Emulating the load characteristic of the engine cooling fan module on the test bench requires a simple model which is able to calculate the load torque for a specified engine compartment topology and a given speed, relative air humidity and air pressure. The block diagram depicting input and output variables of the engine cooling fan process model, which is suitable for implementation on the test bench hardware, is shown in Figure 3.10. The model requires the characteristic fan curves in terms of total generated

Rotational speed n

Car velocity v_{car}

Air temperature ϑ_{cAir}

Air pressure p_{cAir}

Relative air humidity ξ

Engine cooling fan process model

Load torque M_{load}
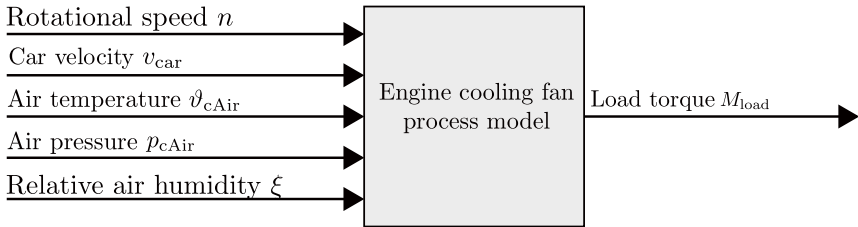
Figure 3.10: Engine cooling fan process model with input and output quantities

pressure Δp_{f} over volume flow and torque over volume flow for a reference rotational speed. Furthermore, the air channel characteristic curve (pressure drop through air channel over volume flow) is needed. Besides the rotational speed of the fan, the air pressure, the relative air humidity and the air temperature are required for exact calculation of the air density. Both the characteristic fan curve and the air channel characteristic curve have to be acquired by measurements in the car or on a test bench respectively. The process for calculation of the current load torque is as follows:

1. Calculation of the air density based on pressure, temperature and relative humidity according to (3.46) to (3.49).

2. Rescaling of fan characteristic (generated pressure Δp_{f} over volume flow and torque over volume flow) to demanded rotational speed according to (3.45) and (3.44). Exemplary results for a rescaling procedure from $2000\,\text{min}^{-1}$ to $2500\,\text{min}^{-1}$ are depicted
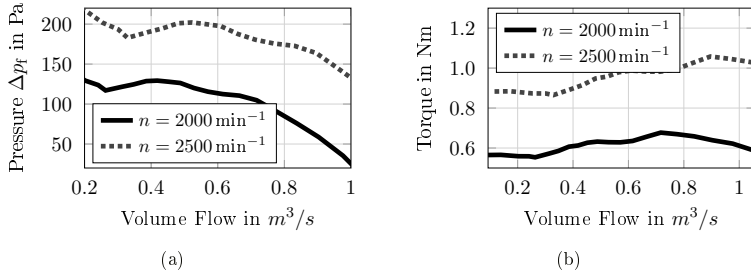
(a)   (b)

Figure 3.11: (a) Generated pressure Δp_f over volume flow for two rotational speeds (measured at $2000\,\mathrm{min}^{-1}$ and calculated at $2500\,\mathrm{min}^{-1}$). (b) Torque over volume flow (measured at $2000\,\mathrm{min}^{-1}$ and calculated $2500\,\mathrm{min}^{-1}$).

in Figure 3.11. The solid line represents base data retrieved from measurements on a test bench or in the car.

3. Offset characteristic of air channel characteristic curve based on current car velocity. As was described in Section 3.1.4, a car velocity greater than zero reduces the total pressure difference, which the fan has to generate for the desired volume flow. The system line hence is shifted to negative direction along the ordinate (See Figure 3.12(a)). The solid line again represents base data from measurements.

4. Determine intersection point between rescaled fan line and adapted air channel pressure drop characteristic (See Figure 3.12(b)).

(a)   (b)
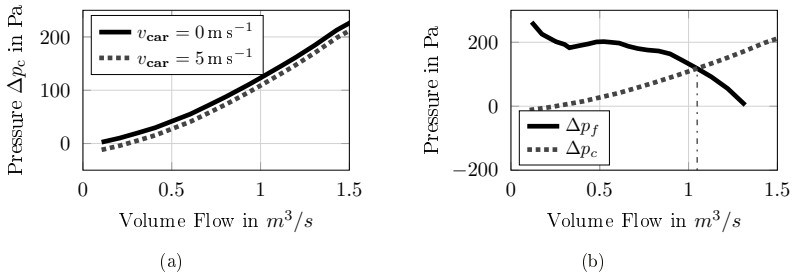
Figure 3.12: (a) Air channel pressure drop over volume flow for two car velocities (measured at $v_{\mathrm{car}} = 0\,\mathrm{m\,s}^{-1}$ and calculated at $v_{\mathrm{car}} = 5\,\mathrm{m\,s}^{-1}$). (b) Finding current operating point by intersecting fan and air channel characteristic curve ($v_{\mathrm{car}} = 5\,\mathrm{m\,s}^{-1}$).

5. Determine load torque from Figure 3.11(b) for given rotational speed with result obtained from step 4.

3.1.5   Validation of the Simulation Model

The accuracy of the derived simulation model was verified by comparison with measurements undertaken with the series ECU of the engine cooling fan. A simplified schematic of the model is illustrated in Figure 3.13. The individual blocks are based on the equations derived in Section 3.1.
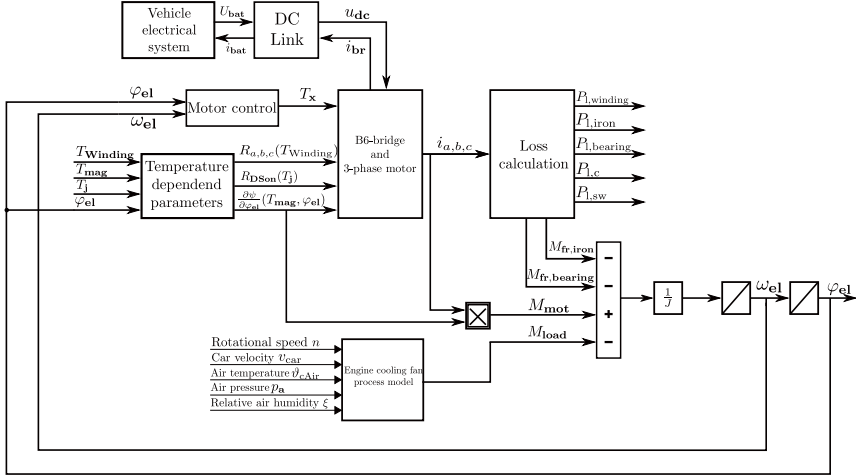

Figure 3.13: Simplified schematic of simulation model

Unfortunately, only few data was available for comparison. Shape of the function over time and rms-values of the line currents were compared for a rotational speed of $2200\,\text{min}^{-1}$ and a load torque of $1.22\,\text{N\,m}$. The corresponding results are displayed in Figure 3.14 and Table 3.2.

The simulated waveform by using (3.6) covers the measurement results quite well. It has to be noted, however, that minor differences do exist, mainly at the peaks of the current. These are due to nonlinearities of the magnetic motor iron circuit, which are not considered in the simulation model. More important than a exact congruence of the waveforms is the rms value, as mean power losses and resulting temperatures are defined by them. As Table 3.2 shows, the relative error (defined as „(measured - calculated)/measured") of the rms values for the line currents are smaller than $|5\,\%|$, which is in consistency with the accuracy demanded from the simulation model. Measurements of the rms values for the DC-link currents were available for a rotational speed of $2500\,\text{min}^{-1}$ with a load torque of $1.22\,\text{N\,m}$, results of the comparison can also be found in Table 3.2. Although performing worse compared to the line current calculations, the values are still within an accuracy limit of $10\,\%$.
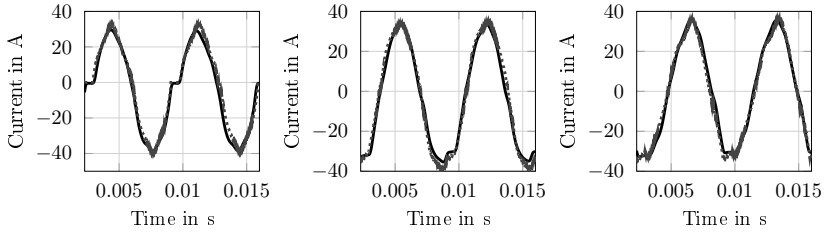
Figure 3.14: Comparison between simulation and measurement for line currents u (left),v (middle) and w (right). Solid black line: measurement, dashed grey line: simulation. Operating point $2200\,\text{min}^{-1}$@$1.22\,\text{N m}$.

Table 3.2: Comparison between measurement and simulation for selected quantities. [*1]: operating point $2200\,\text{min}^{-1}$@$1.22\,\text{N m}$, [*2]: operating point $2500\,\text{min}^{-1}$@$1.22\,\text{N m}$.

Quantity	rms value measurement in A	rms value simulation in A	relative error in %
$i_u^{(*1)}$	24.52	23.58	3.96
$i_v^{(*1}$	25.52	26.68	−4.37
$i_w^{(*1)}$	24.30	23.60	2.93
$i_{\text{bat}}^{(*2)}$	30.04	32.38	−7.24
$i_{\text{dc}}^{(*2)}$	12.77	11.79	8.35

3.2 Test Bench

The design of the test bench was driven by a trade-off that had to be made due to differing requirements of the examined topics. One common requirement is the possibility to arbitrarily change the operating point parameters, i.e. the rotational speed and the load torque. In addition, evaluation of the algorithms for online parameter measurement demands continuous measurement of currents, voltages, the torque delivered by the electric motor, the current rotor angle and various temperatures. For development of the thermal network a temperature chamber is desirable to heat up the motor to arbitrary temperatures. The field of fault detection and diagnosis demands the possibility for artificially introducing faults into the system, such as a motor blockage or motor eccentricities. This, however, demands operation of the fully assembled engine cooling fan module, i.e. including the shroud and the fan.

These differing requirements could not be fulfilled with only one test bench. Operation of the drive in the temperature chamber is not possible in the fully assembled configuration. Furthermore, the used infrared thermometer for measurement of the rotor temperature has a limited temperature range it can be operated in, restricting its usage to a maximum ambient air temperature of $60\,°\text{C}$. Moreover, arbitrarily setting the current operating point with the fan attached to the rotor requires a complex mechanical setup and comprehensive

safety precautions. Hence, the test bench does not offer the possibility to assemble the shroud or the fan.

The resulting setup of the test bench is illustrated in Figure 3.15, corresponding datasheet parameters for selected components are listed in Appendix D. The test bench as depicted in Figure 3.16 is composed of the engine cooling fan motor, an inertia, a torque sensor, an incremental encoder, a load machine and clutches to connect the different components. The engine cooling fan motor is assembled without the series ECU, and no possibility exists to connect the fan or shroud to it. As the design of the test bench does not allow for the assembly of fan or shroud components, a metal cylinder can be coupled, yielding the same moment of inertia as the original fan. The torque sensor and the incremental encoder allow for measurement of the current torque and the rotational speed, respectively. The main datalogging and control device is a dSpace 1103 card. It gathers temperature data from the Keithly datalogger and acquires torque and the rotor angle from the corresponding sensors. It also runs the process model in real-time and transmits the desired load torque to the load machine. This offers the possibility to arbitrarily set the current load torque. The dSpace 1103 can be controlled by a graphical user interface, which is accessible on the operator PC. The dSpace 1103 and the operator PC are connected by Ethernet, which allows for a fast transfer of the acquired measurement data from the dSpace card to the PC.
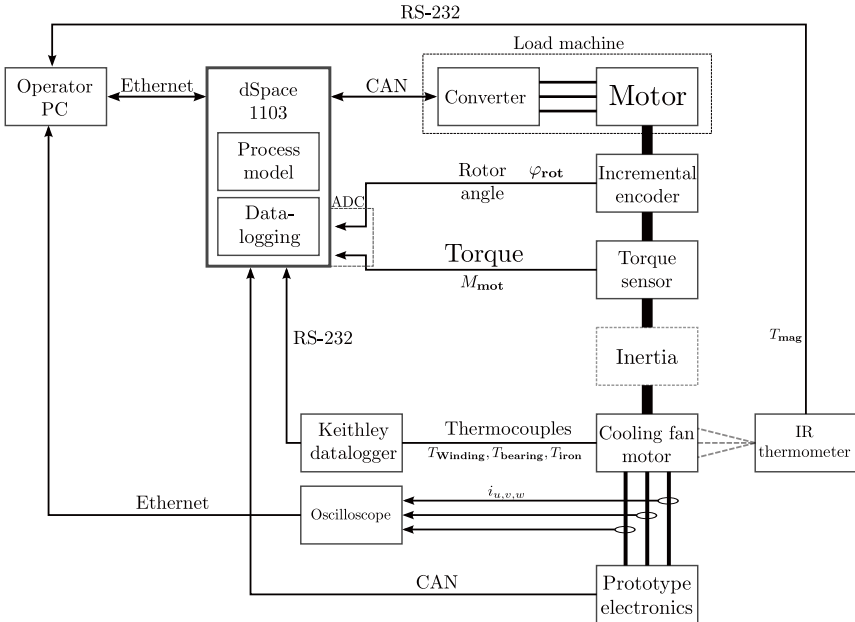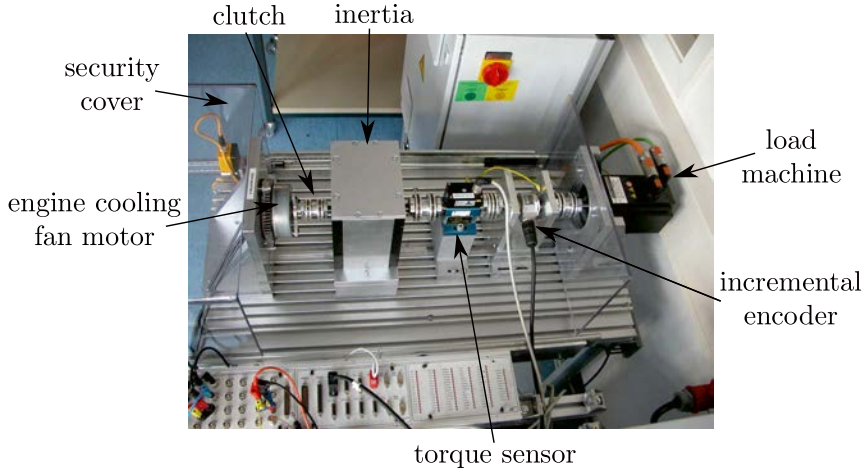

Figure 3.15: Test bench setup

Figure 3.16: Picture of the test bench. The engine cooling fan motor is assembled with the parts as illustrated in Figure 3.4. To account for the missing fan, a inertia can be assembled (large metal cylinder).

Line currents and voltages are measured with an oscilloscope (type LeCroy WaveRunner 6030A) and transferred to the operator PC via an Ethernet interface. The rotor temperature is measured with an infrared thermometer, which is connected to the operator PC with an RS-232 interface.

The test bench allows for measurement of all required variables, such as phase currents, terminal voltages, torque and rotational speed. Unfortunately, an external heat source can not be applied, limiting evaluations concerning the thermal behavior of the motor, as the only heat source is the motor itself. Furthermore, as no fan or shroud can be attached, possibilities for artificially introducing faults are also limited. Nevertheless, due to the process model simulated in real-time on the dSpace 1103 (see Section 3.1.4), parameters such as air temperature, pressure, relative humidity and car velocity, can easily be modified.

On the test bench, all relevant quantities can easily be measured. However, due to cost reasons, the algorithms presented in Section 4 can only utilize a limited number of measured quantities. Figure 3.17 illustrates an electrical setup with measurement possibilities, which are assumed to be feasible with future microcontrollers. A comparison of the measurement possibilities of the series product with the measurement possibilities on the test bench and the assumed future measurement possibilities, which are available for the developed algorithms, is presented in Table 3.3.
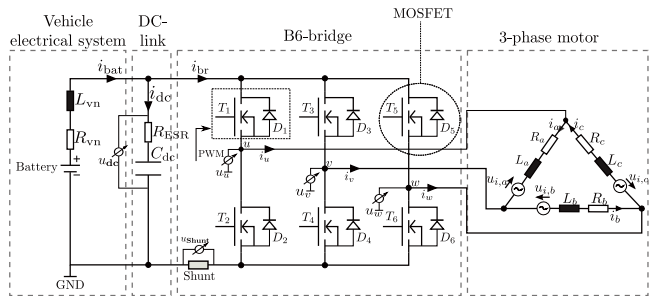
Figure 3.17: Electrical setup of engine cooling fan with measurement possibilities assumed to be feasible with future microcontrollers

Table 3.3: Comparison of measurement possibilities of the series product with measurement possibilities on the test bench and future measurement possibilities available for the developed algorithms.

Quantity	Series product	Test-bench	Assumed for developed fault detection algorithms
Line currents $i_{u,v,w}$	Can not be mesured	Measured by oscilloscope	Reconstructed from shunt measurement
Line voltages $u_{u,v,w}$	Measured by A/D converter on microcontroller	Measured by oscilloscope	Measured by A/D converter on microcontroller
DC link voltage u_{dc}	Can not be measured	Measured by oscilloscope	Measured by A/D converter on microcontroller
Torque M_{mot}	Can not be measured	Measured with torque sensor	Can not be measured
Rotational speed n	Reconstructed by blanking interval	Measured with incremental encoder	Reconstructed by observer / blanking interval
Rotor angle φ_{rot}	Reconstructed by blanking interval	Measured with incremental encoder	Reconstructed by observer / blanking interval

3.3   Conclusion

In this chapter, the engine cooling system, and in particular, the engine cooling fan was described. Equations were given for modeling the electronical, the electromagnetic and the

mechanical part of a permanent magnet synchronous machine. Furthermore, the process model for the engine cooling fan was derived, and a description of the implementation on the test bench was given. The simulation model was validated by comparison with measurements from the series engine cooling fan module, and the test bench setup was described. The elements covered in this chapter are highlighted in Figure 3.18. The next chapter will deal with the extensive topic of online parameter acquisition.
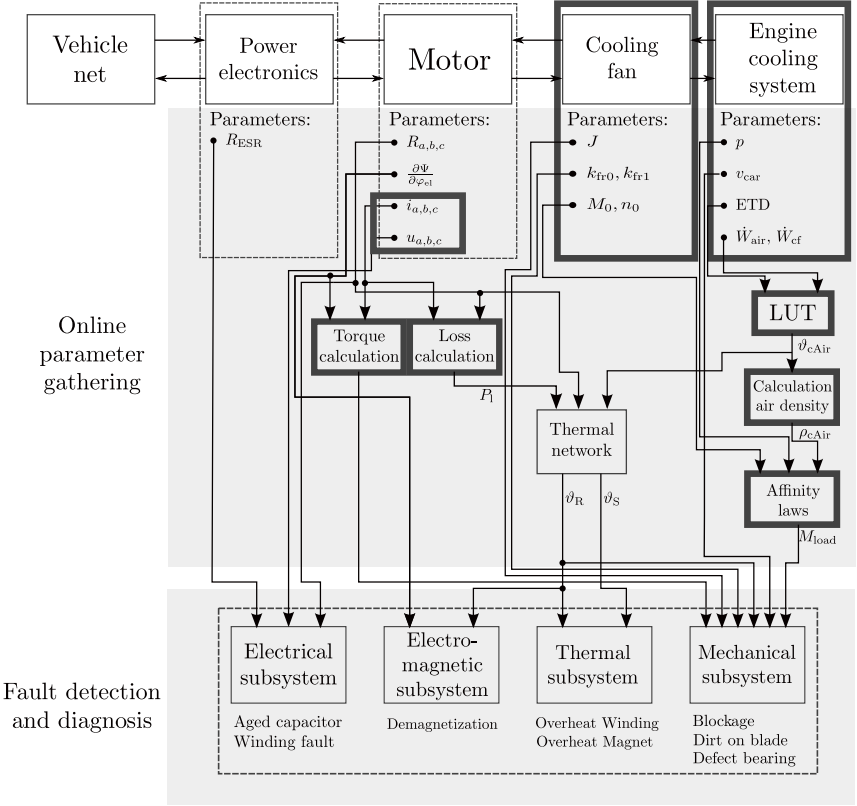

Figure 3.18: Covered elements in this chapter (marked with bold lines).

4 Fault Detection and Diagnosis of the electrical motor: Online Parameter Acquisition

Knowledge of internal states and parameters of the electrical machine is of high importance for a model-based fault detection and diagnosis. With determination of nominal parameters by End-of-Line (EoL) testing, the parameters can be adapted to the individual fan during operation of the drive.

Applying parameter estimation techniques is not always possible, as this demands injection of specific test sequences, such as step functions, sinusoidal waves or Pseudo Random Binary Sequences (PRBS) (see Isermann and Münchhof (2011)). Utilization of a PRBS leads to a disturbance of the normal drive operation, which can not be tolerated in most cases. Furthermore, in the production site short injection pulses are preferred to avoid an increase of the cycle time, as e.g. shown by Kowalczyk et al. (2013).

The techniques presented in this chapter are therefore based on the indirect measurement principle, which utilizes physical relationships between known or measurable quantities and unknown variables. The methods for determination of the winding resistance $R_{a,b,c}$ and the equivalent series resistance R_{ESR} both inject a pulse of short duration, measure the resulting currents and voltages and, based on these measurements, determine the unknown quantities $R_{a,b,c}$ and R_{ESR}, respectively. A similar principle applies for acquisition of the flux linkage over angle, which is determined during a power-off run of the engine cooling fan by measurement of the line-to-line voltages and the rotational speed.
The thermal network presented in Section 4.4 is based on an observer structure, that takes the winding and ambient air temperature as an input to derive the current magnet temperature.

4.1 Winding Resistance

The winding resistance of an electrical machine is an important parameter, which does not stay constant during operation of the drive. Among others, it changes depending on the current winding temperature. The temperature change is due to power loss, which occurs in the windings by the current flowing through them. The relationship between the current resistance and the corresponding winding temperature is given as (Kallenbach et al., 2012)

$$R(T_{winding}) = R(T_{winding,0})(1 + \gamma(T_{winding} - T_{winding,0})), \tag{4.1}$$

with $T_{winding}$ the current winding temperature, $R(T_{winding,0})$ the reference resistance at a given temperature and γ the temperature coefficient of the winding material. For copper,

it holds $\gamma = 0.39\,\%\,\mathrm{K}^{-1}$.

Knowledge of the initial value and development of the resistance during operation gives possibilities for online thermal monitoring of the winding temperature according to (4.1) and for detection of winding faults. Furthermore, it can be used for tuning control of the drive, as these algorithms mostly depend on accurate machine parameters to achieve maximum robustness, respectively output power, for each operating point.

This section outlines a method for reliable winding resistance measurement during standstill as well as during normal operation of the drive. As will be outlined in Section 4.4, this measurement serves as a temperature sensor inside the motor and is the basis for adaptive parametrization of the developed thermal network.

4.1.1 DC Injection Method

Several methods for determination of the winding resistance of electronically commutated drives are covered in the literature. The techniques described can be clustered into three groups: determination via parameter estimation or by injection of an AC (Alternating Current)- respectively DC (Direct Current)-component on the driving motor voltage. As the available literature is very extensive only an exemplary overview can be given.

Velez-Reyes et al. (1989), Souza Ribeiro et al. (1999), Jacobina et al. (2000) and Gorter et al. (1995) use both linear and nonlinear models which serve as a basis for estimation of various motor parameters. Disadvantageous about these models is the presence of more than one varying parameter in the parameter vector. The resistance and the flux linkage both depend on temperature. The self and mutual motor inductances can only be considered as current-invariant for magnetic circuits which do not operate in saturation. Isermann and Münchhof (2011) show that the parameter estimator can only track one time-invariant parameter and thus independent identification of all motor parameters is not possible. The above-mentioned publications circumvent this problem by using several operating points including standstill or require additional hardware for measurement.

The approach to inject a high-frequency carrier signal onto the normal operating voltage and to evaluate the injection frequency component of the phase currents by perfoming a Fourier transform is covered by Wilson et al. (2005) and Wu and Gao (2006). This method was also evaluated during the course of this work, but was found to be unsuitable for the used motor. As no DC components are considered for evaluation, the dq reference frame (see Schröder (2009) and Binder (2012)) has to be utilized. This, however, requires exact knowledge of the rotor field and additional computational effort for the transformations from the stationary three-phase system to the rotor-oriented dq frame. As the typical microcontroller employed for small low-cost drives like the engine cooling fan is almost utilized to full capacity during normal motor operation, the additional resources required for performing a Fourier transform cannot be provided. Furthermore, the results obtained by the AC injection method were not accurate enough for determination of the winding temperature which is due to saturation effects resulting in nonlinear inductance values.
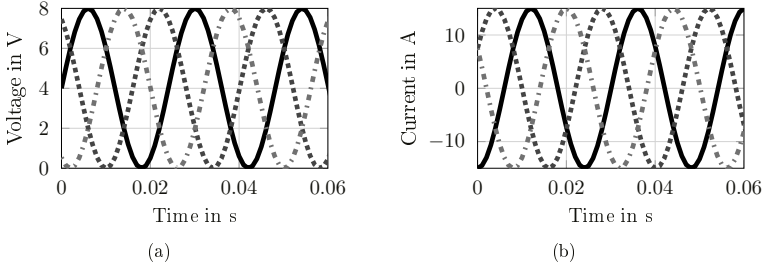
Figure 4.1: Terminal voltages and phase currents during normal motor operation (simulation). (a) Terminal voltages (b) Phase currents

The DC injection method is similar to the AC injection described above, only that DC quantities are superimposed on the motor voltages instead of AC quantities. The general principle of this method is outlined in Stiebler and Plotkin (2005). Implementation of this method is very simple, as only DC quantities are considered, which does not require an exact rotor position measurement and hence does not indicate the utilization of the dq frame. Due to its simplicity and low computational demand, the DC method is the preferred choice for determination of the winding resistance.

However, as will be shown in this section, in its original form the algorithm has some limitations, that render it unsuitable for series implementation. In the following, the base method developed by Stiebler and Plotkin (2005) is presented together with an extension which overcomes the limitations set by the algorithm originally developed.

Principle of operation

The principle of the DC method is the superposition of a DC voltage U_{inj} to one phase of the motor. The injection takes place either in standstill or during normal operation of the motor. In the latter case, the DC voltage is superimposed on the driving AC voltage. The injected DC voltage leads to an asymmetry of the motor currents, causing an offset on all three phases. The current of the phase that the DC voltage is being injected to is shifted by $I_{\text{res,inj}}$, the other two phase-currents by $-\frac{1}{2}I_{\text{res,inj}}$. Simultaneous injection on all motor terminals would result in no additional DC-offset of the phase currents. For sinusoidal motor currents, the process of an injection during normal operation is illustrated in Figure 4.1. The motor terminal voltages and the phase currents for normal operation of the drive are shown in Figure 4.1(a) and Figure 4.1(b), the voltages and currents during injection are illustrated in Figure 4.2(a) and Figure 4.2(b).
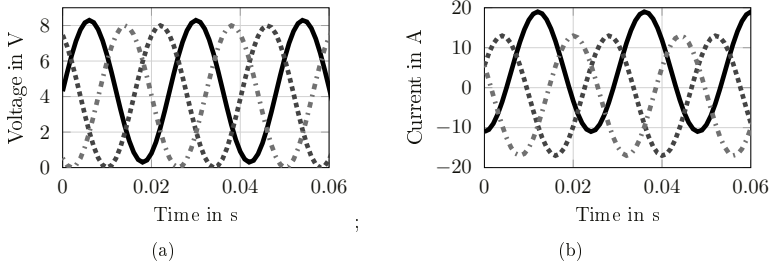
Figure 4.2: Terminal voltages and phase currents during injection period (simulation). The DC offset U_{inj} is injected onto terminal u. (a) Terminal voltages. The voltage u_u is shifted by U_{inj}. (b) Phase currents. i_u is shifted by $I_{\text{res,inj}}$, $i_{v,w}$ by $-\frac{1}{2}I_{\text{res,inj}}$.

Mathematical illustration of the base DC-method is performed by extending (3.13) with the DC injection voltage, exemplary for phase a, leading to

$$
\begin{aligned}
u_a + U_{\text{inj}} &= R_a(i_a + I_{\text{res,inj}}) + \frac{\partial \Psi_{a,\text{R}}}{\partial \varphi_{\text{el}}}\omega_{\text{el}} + \sum_{j=a,b,c}\left(\frac{\partial \Psi_{a,\text{S}}}{\partial i_j}\right)\frac{\mathrm{d}(i_j + I_{\text{res,inj}})}{\mathrm{d}t} \\
&= R_a i_a + R_a I_{\text{res,inj}} + \frac{\partial \Psi_{a,\text{R}}}{\partial \varphi_{\text{el}}}\omega_{\text{el}} + \sum_{j=a,b,c}\left(\frac{\partial \Psi_{a,\text{S}}}{\partial i_j}\right)\frac{\mathrm{d}i_j}{\mathrm{d}t} + \sum_{j=a,b,c}\left(\frac{\Psi_{a,\text{S}}}{\partial i_j}\right)\frac{\mathrm{d}I_{\text{res,inj}}}{\mathrm{d}t},
\end{aligned}
\tag{4.2}
$$

with U_{inj} the injected voltage and $I_{\text{res,inj}}$ the resulting current. As assumed during deduction of the motor equations, the magnetic circuit is considered to be linear. The AC and DC voltage sources can then be described as acting independent from each other, i.e. their responses can be simply added. Assuming further that $\frac{\mathrm{d}I_{\text{res,inj}}}{\mathrm{d}t} = 0$ and subtracting (4.2) from (3.13) gives

$$
U_{\text{inj}} = R_a I_{\text{res,inj}}.
\tag{4.3}
$$

In steady state, the resulting DC current is thus only depending on the injected DC voltage. Furthermore, the winding resistance of one phase can easily be obtained by dividing the injection voltage by the resulting DC-current

$$
R_a = \frac{U_{\text{inj}}}{I_{\text{res,inj}}} = \frac{U_{\text{dc}}\chi_{\text{inj}}}{I_{\text{res,inj}}},
\tag{4.4}
$$

with $\chi_{\text{inj}} \in [0,1]$ the duty cycle superimposed on the normal motor operation, and U_{dc} the voltage of the intermediate circuit („DC-link") capacitor.

Applying the aforementioned procedure to the engine cooling fan requires the actual motor topology to be taken into account. The DC injection voltage is generated with the B6-bridge by adding χ_{inj} to the duty cycle demanded from the controller for the respective phase. Consequently, the measurement path has to be extended by the MOSFET
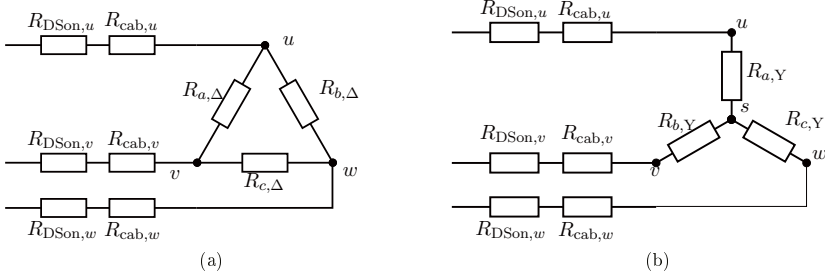
Figure 4.3: Measurement path for DC-injection: (a) Delta configuration, (b) Equivalent star configuration

resistances R_{DSon} and the connecting copper line resistances on the PCB R_{cab} (see Figure 4.3(a)), as the generated voltage is influenced by the voltage drops across the respective resistances. Despite the engine cooling fan being a motor with the windings in delta configuration, derivation of (4.4) is performed using the equivalent star configuration as illustrated in Figure 4.3(b). The resulting star resistance can then easily be transformed to its delta correspondence. The star-delta transformation is covered thoroughly in Appendix B.

It is assumed that the stator winding, the MOSFET and the copper line resistances of all three phases have the same values. The total resistance of each phase can thus be expressed as

$$R_{\text{Y}}^* = R_{\text{DSon}} + R_{\text{cab}} + R_{\text{Y}} \,. \tag{4.5}$$

The resulting setup is depicted in Figure 4.4(a). As the DC injection takes only place on one motor terminal and as the superposition theorem is applied, the impact of the DC source can be evaluated by setting all AC voltage sources to zero (see Figure 4.4(b)). Further on, the parallel circuit consisting of the resistances from phases b and c can be combined to one single resistance (illustrated in Figure 4.4(c)).

When superimposing the DC voltage on line u, the voltage U_{um} yields

$$U_{um} = \chi_{\text{inj}} U_{\text{dc}} \,. \tag{4.6}$$

The voltage U_{us} can then be derived as

$$\begin{aligned} U_{us} &= \frac{R_{\text{Y}}^*}{R_{\text{Y}^*} + \frac{1}{2} R_{\text{Y}}^*} U_{um} = \frac{2}{3} U_{um} \\ &= \frac{2}{3} \chi_{\text{inj}} U_{\text{dc}} \,. \end{aligned} \tag{4.7}$$

With (4.7) and the DC-current $I_{\text{res,inj}}$, the total resistance in star configuration can then be expressed as

$$R_{\text{Y}^*} = \frac{U_{us}}{I_{\text{res,inj}}} = \frac{2}{3} \chi_{\text{inj}} \frac{U_{\text{dc}}}{I_{\text{res,inj}}} \,. \tag{4.8}$$
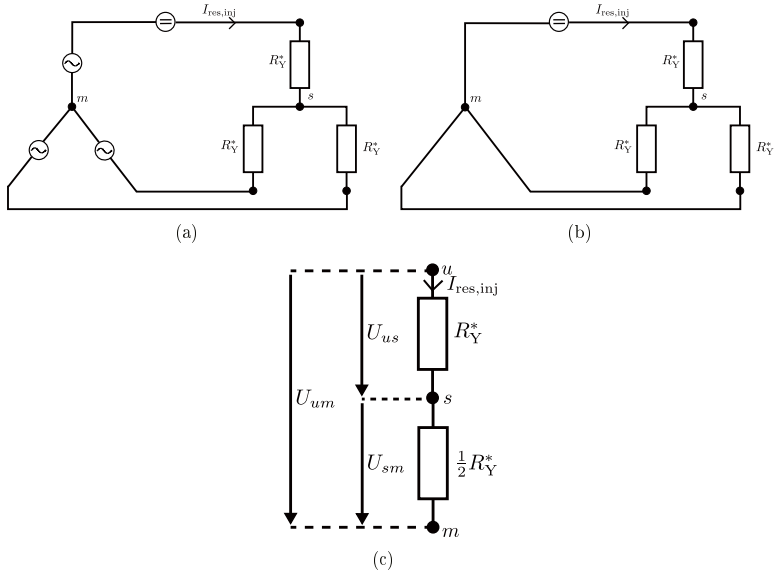
Figure 4.4: (a) AC and DC voltage sources combined, (b) Setting AC voltage sources to zero, (c) Combining resistances from phases b and c

Substitution of (4.5) in (4.8) finally yields for one phase resistance

$$R_{\mathrm{Y}} = \frac{2}{3} \frac{\chi_{\mathrm{inj}} U_{\mathrm{dc}}}{I_{\mathrm{res,inj}}} - (R_{\mathrm{DSOn}} + R_{\mathrm{cab}}). \tag{4.9}$$

The approach described by Stiebler and Plotkin (2005) assumes that the intended DC voltage, which is superimposed onto the normal control voltages is exactly applied on the motor terminals. This, however, cannot be achieved due to a voltage drop across the B6-bridge and nonlinearities inherent in the MOSFETs' switching process. The voltage drop is caused by the on-resistance of an enabled MOSFET and the copper line on the PCB which connects the MOSFETs' to the corresponding motor terminals. The nonlinearities are caused by deadtimes that have to be adhered to prevent a short-circuit in the bridge. In addition the switching process has to be considered, i.e. the time that elapses between the arrival of the switching signal at the bridge driver and the fully interconnected state of the MOSFET. Even with knowledge of the current MOSFET temperature, the load dependent effects cannot be compensated properly.

An exemplary switching process of the used B6-bridge is illustrated in Figure 4.5. During the deadtime, the resulting mean voltage is distorted by the clamping voltage of the freewheeling-diode. In addition, the terminal voltage shows oscillations which are due to
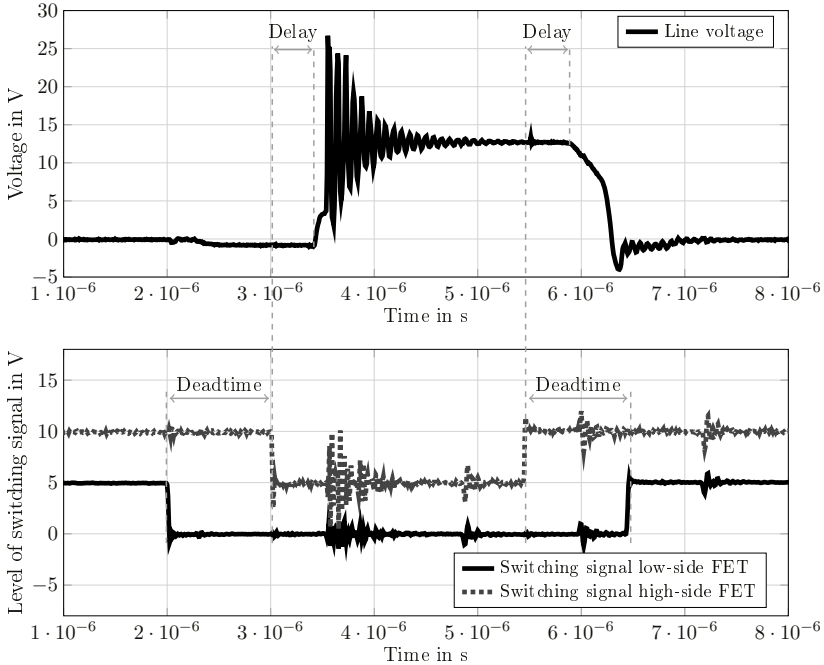
Figure 4.5: Exemplary switching process (measurement). Please note that the high-side switching signal was offset by 5 V for better visibility.

the absence of a damping network. The time delay after the switching process, until the line voltage starts rising or falling, can also be clearly seen. These effects lead to a terminal voltage which is different from the targeted one. This in turn results in a wrong resistance calculation, as the DC-current does not fit with the assumed duty-cycle in (4.4).

This effect is demonstrated in Figure 4.6, which shows the deviation of the measured DC-current to the one expected from theory for different injection duty cycles. As can be seen, the higher the duty cycle, the lower the deviation becomes. Considering above explanations and Figure 4.5, this seems comprehensible. The lower the duty cycle, the higher the influence of switching delays and the settling-in process on the resulting mean voltage.

In Plotkin et al. (2008), a deadtime compensation method is proposed for increasing accuracy of the DC method. The described compensation, however, relies on an operating-point dependent Look-up-table (LUT). The steps required for acquisition of the LUT table data are contradictory to the goal of minimizing the application effort set forth by this work. In addition, the temperature- and load-dependent switching cycles are not taken into account by the method, which render it unsuitable for series implementation.
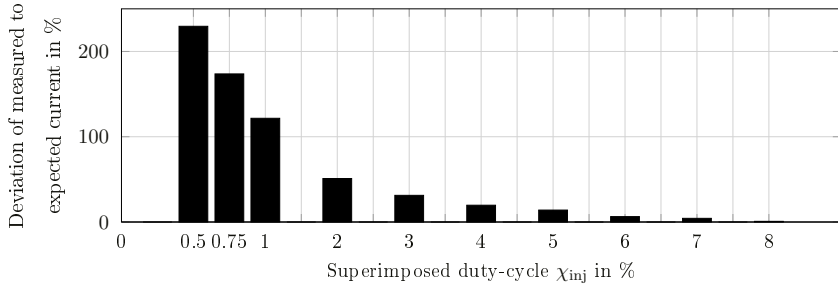
Figure 4.6: Deviation of measured DC-current to current expected from theory for different injection duty cycles

The method was thus enhanced with a voltage measurement at the motor terminal. Due to the high switching-frequency of $20\,\text{kHz}$, two filters were implemented. The first filter is a hardware low-pass filter with a cutoff frequency of $250\,\text{Hz}$. Aim of this filter is to eliminate most of the frequencies above the fundamental wave frequency (e.g. $167\,\text{Hz}$ for an operating point with a rotational speed of $2500\,\text{min}^{-1}$). Output of this stage is a smoothed signal of the motor driving voltage. For extraction of the DC offset, a second filter is required, which is implemented in software. This is a simple average filter which detects the mean of the input signal. This 2-phase approach allows for short injection times, as the settling-in process of the hardware low-pass filter is very fast due to the low cutoff frequency. Utilization of a filter, outputting the DC component of the motor terminal voltage, would result in a long settling-in process, requiring long injection times as well. However, the longer the injection time, the longer the normal operation is disturbed and the more additional power loss is generated. The mean current is extracted with the same 2-phase filter structure. The proposed configuration is illustrated in Figure 4.7.
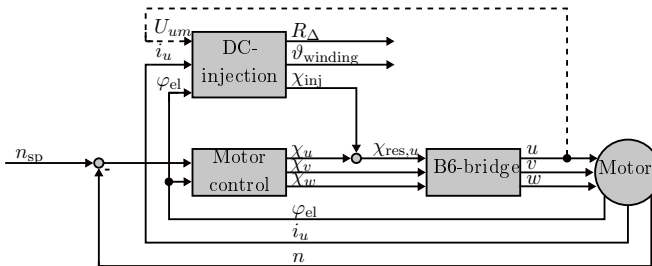

Figure 4.7: Block diagram of DC-injection method with terminal voltage measurement u_{um}

In case the motor terminal voltage U_{um} is measured (see Figure 4.4), the phase resistance in star configuration can easily be calculated and (4.9) becomes

$$R_{\mathrm{Y}} = \frac{2}{3} \frac{U_{um}}{I_{\mathrm{res,inj}}} \,.$$
(4.10)

4.1.2   Implementation and Results

Both the standstill-measurement and the measurement during operation were implemented as state machines. The two execution sequences are constructed similar with the sole difference, that the state advancement is time-driven for the standstill measurement and depends on the number of detected electrical periods for the measurement during operation. The timing diagram for the standstill measurement is illustrated in Figure 4.8. Once the measurement procedure is activated, the mean of the line current without any
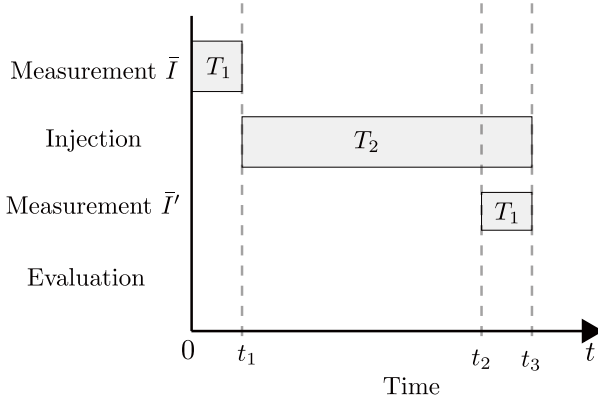
Figure 4.8: Timing diagram for standstill measurement.

injection voltage is determined for a time-period of length T_1. This step is performed, as, depending on the control strategy, the base duty-cycle can be set to 50 %, which can lead to a non-zero line-current in idle-state due to nonlinearities and component tolerances in the B6-bridge. The injection takes place for a time-period of length T_2. The injection time should be kept at a minimum so that power loss is minimized, yet be long enough for the system to settle in. The electric time constant for the engine cooling fan is given as

$$\tau_{\mathrm{el}} = \frac{L}{R} = 2.94 \times 10^{-3}\,\mathrm{s}\,.$$
(4.11)

The minimum injection time can thus be derived as

$$T_{2,\mathrm{min}} = 3\tau_{\mathrm{el}} = 8.842 \times 10^{-3}\,\mathrm{s}\,.$$
(4.12)

Starting from t_2 in Figure 4.8, the mean of the line-current again is determined for a time-period of length T_1. The resulting DC current is then calculated as

$$I_{\text{res,inj}} = \bar{I}' - \bar{I}\,. \tag{4.13}$$

T_2 should be chosen large enough for the rotor field to be in mechanical alignment with the resulting field from the injected DC current. In practice, an injection for a time period of $T_{2,\text{min}}$ is not sufficient and results in measurement errors due to the movement of the rotor. An injection time of 40×10^{-3} s was determined to yield a good performance. For applications that have a rotor angle measurement available during standstill, the state machine could also check for the rotor angle and dynamically adapt T_2 such, that the measurement is started only, when the rotor is not moving anymore.

The timing diagram for the injection during normal operation is shown in Figure 4.9. As the mean value is taken for the current, it is important to use data for full electrical cycles. When deciding, how many electrical cycles should be used for data evaluation, it has to be taken into account that a partially demagnetized rotor results in p electrical cycles which are not identical. p is the pole-pair number and is four for the used engine cooling fan. The number of electrical cycles during measurement of mean values hence should be chosen as a complete multiple of four.
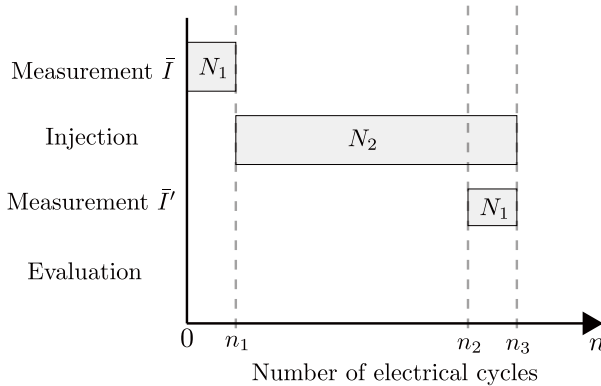

Figure 4.9: Timing diagram for measurement during operation.

Choosing an appropriate injection magnitude and time strongly depends on the type of application the method is to be used for. Under high-load conditions, the DC bias, caused by the injection, produces an additional flux component, which results in unbalanced magnetic saturation during each electrical cycle. As shown by Zhang et al. (2011), this unbalanced saturation causes multiple harmonics at even orders. They interact with the fundamental wave and generate torque ripples, which in turn create additional noise. However, for the engine cooling fan this torque ripple is considered uncritical, as the

mechanical damping is very strong due to the high inertia of the fan.
Furthermore, the DC-bias induces additional copper losses in the windings

$$P_{\text{winding,inj}} = U_{\text{inj}} I_{\text{res,inj}} . \tag{4.14}$$

With a magnitude of 5 % of the superimposed injection duty cycle χ_{inj} and a DC-link
voltage of 13 V, the resulting DC-current is approximately 27 A (assuming a phase winding
resistance of $37.5 \times 10^{-3} \, \Omega$). This leads to an additional power loss of 13.5 W, decreasing
the maximum efficiency by around 5 %. Due to the long thermal time constant of the motor
(see Section 4.4, approximately between 400 s and 500 s), an injection interval between
60 s and 120 s is sufficient, rendering the increasing power loss negligible.

In order to further improve the robustness of the presented approach, the terminal voltage
measurement was supplemented with a differential amplifier to allow for a differential
voltage measurement. With the measurement of the differential voltage U_{uv} between lines
u and v, following equation can be derived from Figure 4.3(b)

$$U_{uv} = U_{us} + U_{sv} = R_{\text{Y}} I_{\text{res,inj}} + \frac{1}{2} R_{\text{Y}} I_{\text{res,inj}} = \frac{3}{2} R_{\text{Y}} I_{\text{res,inj}} . \tag{4.15}$$

From (4.15) it follows that

$$R_{\text{Y}} = \frac{2}{3} \frac{U_{uv}}{I_{\text{res,inj}}} , \tag{4.16}$$

and transforming to the delta configuration

$$R_{\Delta} = 3R_{\text{Y}} = 2 \frac{U_{uv}}{I_{\text{res,inj}}} . \tag{4.17}$$

Both the implementation as described by Stiebler and Plotkin (2005) and the method
enhanced with a terminal voltage measurement were evaluated at the test bench. The
method originally proposed did neither produce satisfactory results for the standstill nor
the measurement during operation of the drive. Results for an injection during operation
are shown in Figure 4.10. The winding temperature used for comparison was retrieved
with several temperature sensors mounted on the surface of all three motor windings.
The temperature dependent voltage drops across the B6-bridge and the PCB were com-
pensated. As can be seen in Figure 4.10, even with this compensation, the determined
winding temperature is only accurate for operating points with a high load torque. For
lower loads, lower duty-cycles are required, which exacerbate the effects shown in Fig-
ure 4.5 and demonstrated in Figure 4.6.

Results for an injection during operation with the enhanced method with the terminal
voltage measurement are illustrated in Figure 4.11. For the shown operating points, the
mean relative error between the DC injection value and the temperature gathered with a
sensor is 5.9 % and a maximum deviation of 7 °C can be observed. The waveforms of the
filtered current and line-to-line voltage during an injection cycle are shown in Figure 4.12.
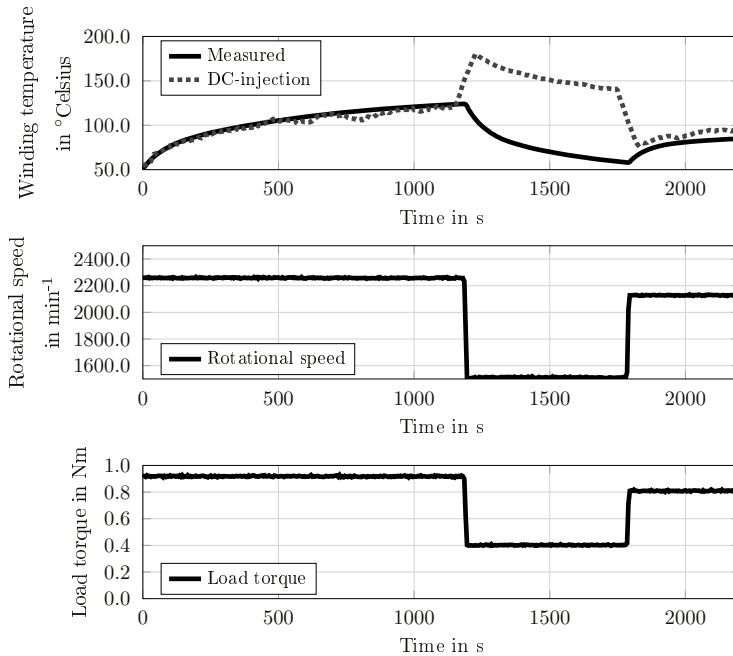The offset shift of the current, after the injection started, can clearly be seen between

Figure 4.10: Comparison of measured winding temperature with temperature retrieved with DC-injection method without terminal voltage measurement for different operating points. In the top illustration the dotted line represents the winding temperature determined with the DC injection and the straight line the mean of the measured winding temperature.

0.1 s and 0.28 s. The voltage signal, however, changes only a little. In addition, a small oscillation can be seen on the voltage signal, which is due to an improper damping of the test bench.

The voltage and current waveforms for an injection during standstill are depicted in Figure 4.13, results for a standstill measurement with an injection every 10 s are illustrated in Figure 4.14. Please note, that, due to the injection, the temperature increases slightly for the measurement period. The standard deviation for the shown measurement is 3.8 °C and the mean relative error is 11.3 %.

4.1.3 Conclusion

It can be concluded, that the method originally proposed by Stiebler and Plotkin (2005) does not give satisfactory results for series implementation. As shown in this section,
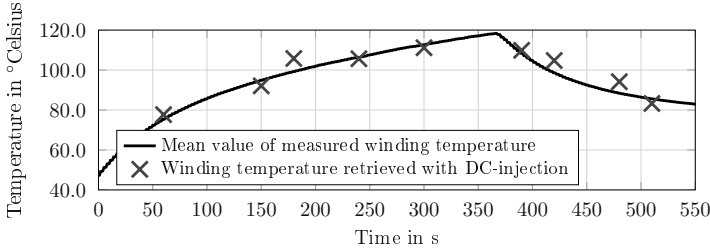
Figure 4.11: Comparison of measured winding temperature with temperature retrieved with DC-injection method with terminal voltage measurement for the same operating points as shown in Figure 4.10
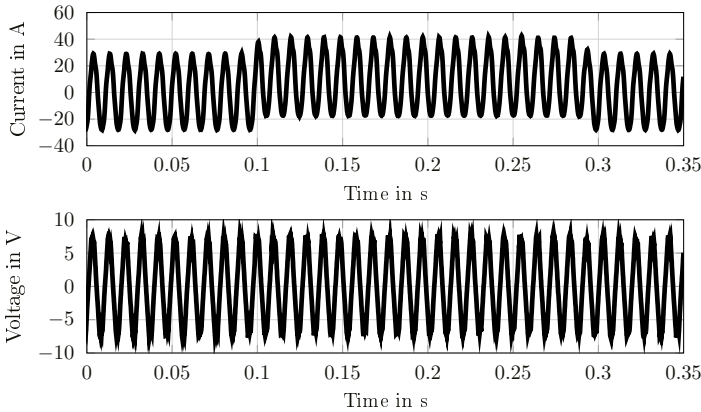

Figure 4.12: Line current and line-to-line voltage during an injection at $t = 0.1\,\mathrm{s}$ (measurement)

the measurement accuracy can be increased by utilization of an additional hardware filter for determination of the injected DC offset. The software filter that calculates the mean of the signal is not computational intensive, which allows for implementation of the enhanced method on the microcontrollers typically utilized for small electrical drives. The described method shows a standard deviation of 3.8 °C for standstill measurement, and, for the tested operating points, a maximum deviation to the value measured with a sensor during operation of 7 °C.

The resistance is used for calculation of the power loss induced in the winding. It is furthermore utilized for detection of a winding fault (see Section 5.1). Deriving the winding temperature from the winding resistance constitutes a virtual temperature sensor inside the motor, which is of benefit to the thermal network presented in Section 4.4. Further-
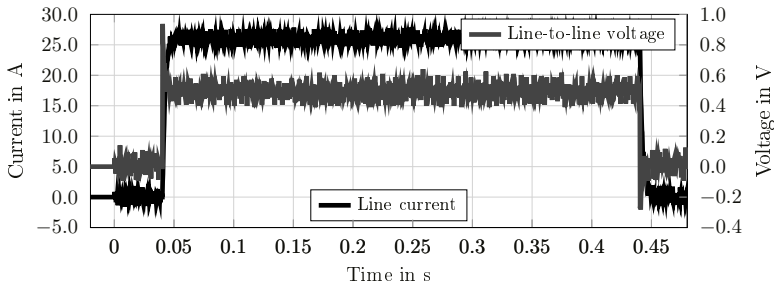
Figure 4.13: Line-to-line voltage and line-current for standstill-measurement. Please note that the base duty-cycle during idle-phase was set to 0.
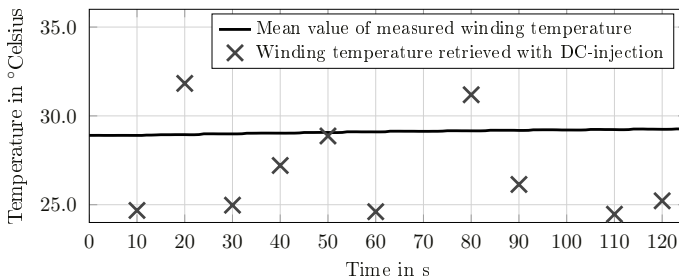

Figure 4.14: Results for standstill measurement. Injection was carried out every 10 s with an injection duty-cycle of 5 %.

more, the standstill measurement offers the possibility to acquire a winding temperature before starting the motor, which was so far only possible with a dedicated temperature sensor.
In the next section the determination of the flux linkage over angle is presented, which is an important quantity for diagnosing a demagnetization event and for calculating the torque delivered by the electrical motor.

4.2   Flux Linkage over Angle

Similar to the winding resistance, the flux linkage of an electrical machine is an important variable during motor design and one of the main parameters describing properties of the machine. The resulting flux linkage can either be calculated by simulation or directly measured at the test bench. For determination at the test bench the induced voltages on

the three motor terminals are measured and the flux linkage is calculated according to

$$\frac{\partial \Psi_k}{\partial \varphi_{\mathrm{el}}} = -\frac{u_{\mathrm{i},k}}{\omega_{\mathrm{el}}}, \tag{4.18}$$

with $u_{\mathrm{i},k}$ the measured induced voltage, ω_{el} the electrical angular velocity of the rotor and $\frac{\partial \Psi_k}{\partial \varphi_{\mathrm{el}}}$ the corresponding change of the flux linkage. For this measurement, it is necessary that no current flows through the motor coils and that ω_{el} stays constant. To achieve these conditions the motor under test is driven by an external machine.

A method which allows for determination of the current flux linkage of a machine used in the field is highly desirable, as knowledge of the flux linkage in the software allows for

1. torque calculation according to (3.19)

$$M_{\mathrm{mot}} = p \sum_{k=a,b,c} \frac{\partial \Psi_{k,\mathrm{R}}}{\partial \varphi_{\mathrm{el}}} i_k, \tag{4.19}$$

2. demagnetization or improper magnetization detection and,

3. adaption of the control algorithm to the machine.

Point one requires a detailed knowledge of the shape and amplitude of the flux linkage over one electrical cycle. The required information could be gathered with the above described measurement on a test bench or with an EoL equipment. However, the constraint that the drive has to be kept at a constant speed for a certain amount of time is contradictory to short cycle times demanded by production. Measuring the flux linkage for some samples on the test bench and using this measurement for torque calculation does not account for changes in the flux linkage due to a demagnetization or tolerances of the magnet properties. It is therefore required to update the information about the flux linkage at regular intervals in the field.

Operating a magnet above the maximum rated operating point in a counter-acting field leads to a demagnetization event. Irreversible loss of magnetization can result from elevated temperatures and strong opposing magnetic fields. A uniform or partial demagnetization of the magnets requires more current in the machine to deliver the desired output power, which induces more thermal stress in the motor and the connected electronics. As will be shown in Section 5.2, knowledge about the development of certain harmonics, which are machine dependent, is sufficient for demagnetization detection using the flux linkage over angle.

Determination of the shape and amplitude of the flux linkage also allows for adaption of the control algorithm to a specific machine. As the topic of adaptive control is not covered in this work, this point will not be discussed in more detail.

In the following, an algorithm is presented which allows for reliable determination of the induced voltage at an EoL run and in the field. The flux linkage over angle gathered

with the described method can be used for torque calculation (see Section 5.4) and for demagnetization detection (see Section 5.2).

4.2.1   Proposed Method

The method proposed here performs a measurement of the induced voltages and reconstructs the flux linkage over angle according to (4.18). The induced voltage can only be measured during a no-load operation of the drive. Taking the engine cooling fan, three scenarios result from this requirement allowing for its determination:

1. Strong deceleration during power-off due to very low rotor inertia (no fan attached) and active braking by the EoL equipment for reduction of the cycle-time (EoL parameterization in the plant of the supplier of the electrical motor).

2. Slow deceleration during power-off in the car with high inertia due to the attached fan.

3. Acceleration/deceleration in the car due to the airstream caused by changing car velocity (generator operation).

Scenario one thus aims at reconstruction of the flux linkage at the EoL with no fan attached to the electrical motor (resulting in a very low inertia), while scenario two and three refer to the normal operation in the car with the whole assembly consisting of electrical motor and fan attached to it. For subsequent considerations, only point one and two are considered here, as point three would demand constant operation of the engine cooling fan ECU to monitor the level of the induced voltage.

Exemplary shapes of the induced voltages for scenarios one and two are depicted in Figure 4.15. As can be seen, the slow deceleration during power-off caused by the high fan inertia is the least critical case, as the velocity for the first mechanical period can be considered as constant. In contrast, the power-off during the EOL test shows a strongly varying velocity for the first mechanical period of the signal.
 Basis for reconstruction of the flux linkage over angle is the measurement of the terminal voltages $u_{\mathrm{u}}, u_{\mathrm{v}}$ and u_{w}. During a no-load operation, no current is flowing through the motor coils. Thus, the observer utilized for reconstruction of the rotor angle and rotor angular velocity (see Section 3) is not functional. After measurement of the terminal voltages, the reconstruction procedure consists of the following steps:

1. Reconstruction of $\hat{\varphi}_{\mathrm{el}}(t)$ and $\hat{\omega}_{\mathrm{el}}(t)$ for the first mechanical period based on the zero-crossings of the induced voltage.

2. Based on $\hat{\omega}_{\mathrm{el}}(t)$, rescaling of the measured voltage to a signal with constant velocity.
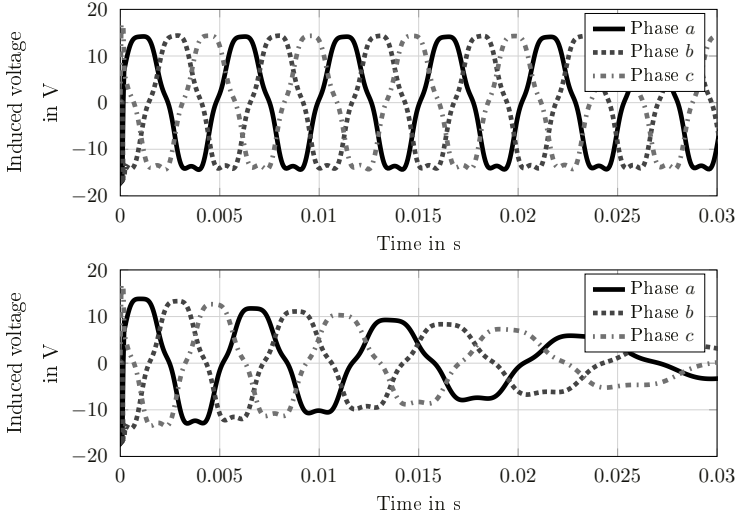
Figure 4.15: Measurement of induced voltage during power-off with inertia of fan (top) and with sole rotor inertia and active braking by the EoL equipment (bottom).

3. Fitting of the original, equidistant time axis to the signal with constant velocity, leading to a not equally spaced time axis.

4. Interpolation to the required sampling rate.

5. Performing of a Fast-Fourier-Transform (FFT) to obtain the spectrum of the flux linkage over angle.

In the following, equations for a power-off operation of the engine cooling fan are derived. Based on these equations, exemplary shapes of the induced voltage are determined and utilized for demonstration of the above described steps.

Basis for derivation is (3.26), which describes the mechanical part of the engine cooling fan by the equation of motion as

$$J\dot{\omega}_{\mathrm{rot}} = M_{\mathrm{mot}} - (M_{\mathrm{load}} + M_{\mathrm{fr,bearing}} + M_{\mathrm{r,iron}}) . \tag{4.20}$$

Setting M_{mot} to zero and assuming no friction and no rotational iron losses ($M_{\mathrm{fr,bearing}} = M_{\mathrm{r,iron}} = 0$) yields

$$J\dot{\omega}_{\mathrm{rot}} = -M_{\mathrm{load}} . \tag{4.21}$$

Approximating the load with a square of ω_{rot} and introducing a proportionality constant k_{fan} gives

$$J\frac{\mathrm{d}\omega_{\mathrm{rot}}}{\mathrm{d}t} = -k_{\mathrm{fan}}\omega_{\mathrm{rot}}^2 . \tag{4.22}$$

Solving this differential equation by separation of the variables yields

$$-\frac{1}{\omega_{\mathrm{rot}}} + C = -\frac{1}{J}k_{\mathrm{fan}}t\,. \tag{4.23}$$

By setting $t = 0$, one can derive a value for the constant C as

$$C = \frac{1}{\omega_{\mathrm{rot}}(0)}\,, \tag{4.24}$$

with $\omega_{\mathrm{rot}}(0)$ the initial angular velocity before powering off the drive. Solving for ω_{rot} finally yields

$$\omega_{\mathrm{rot}}(t) = \frac{J \cdot \omega_{\mathrm{rot}}(0)}{k_{\mathrm{fan}} \cdot \omega_{\mathrm{rot}}(0) \cdot t + J}\,. \tag{4.25}$$

With $\omega_{\mathrm{rot}} = \frac{\omega_{\mathrm{el}}}{p}$, (4.25) becomes

$$\omega_{\mathrm{el}}(t) = \frac{J \cdot p \cdot \omega_{\mathrm{el}}(0)}{k_{\mathrm{fan}} \cdot \omega_{\mathrm{el}}(0) \cdot t + J \cdot p}\,. \tag{4.26}$$

Integration of (4.26) yields

$$\varphi_{\mathrm{el}}(t) = \int \omega_{\mathrm{el}}(t)\mathrm{d}t = \frac{Jp}{k_{\mathrm{fan}}}\ln\left(k_{\mathrm{fan}}\omega_{\mathrm{el}}(0)t + Jp\right) + C\,. \tag{4.27}$$

By assuming $\varphi_{\mathrm{el}}(0) = 0$ as an initial condition, C can be calculated as

$$0 = \frac{J \cdot p}{k_{\mathrm{fan}}} \cdot \ln\left(p \cdot J\right) + C \tag{4.28}$$

$$C = -\frac{J \cdot p}{k_{\mathrm{fan}}} \cdot \ln\left(p \cdot J\right)\,. \tag{4.29}$$

Assuming a sinusoidal shape of the induced voltage, $u_{\mathrm{i}}(t)$ can then be derived as

$$u_{\mathrm{i}}(t) = \frac{u_{\mathrm{i}}(0) \cdot \omega_{\mathrm{el}}(t)}{\omega_{\mathrm{el}}(0)} \cdot \sin(\varphi_{\mathrm{el}}(t))\,, \tag{4.30}$$

with $u_{\mathrm{i}}(0)$ the induced voltage at $t = 0$.

As no rotor angle measurement is available, the zero-crossings of the induced voltages are the only indicator available for capturing the velocity characteristic of the motor during the measurement cycle. The first step therefore includes determination of the zero-crossings and saving of the corresponding times. An exemplary shape of the induced voltage during a power-off with low inertia, created with (4.30), is shown in Figure 4.16. The zero-crossings are marked in the figure as well.

For the exemplary sine wave, the distance between two zero-crossings marks exactly 180°. Therefore, a diagram depicting the electrical angle depending on the times of the zero-crossings can be drawn by multiplication of the number of zero-crossings found with π (See Figure 4.17). When using all three motor phases, the distance between two zero-crossings reduces to 60°, as illustrated in Figure 4.18.

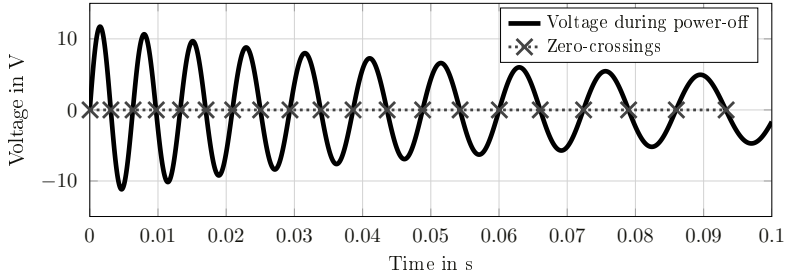By approximating this relationship with a polynomial of degree n according to

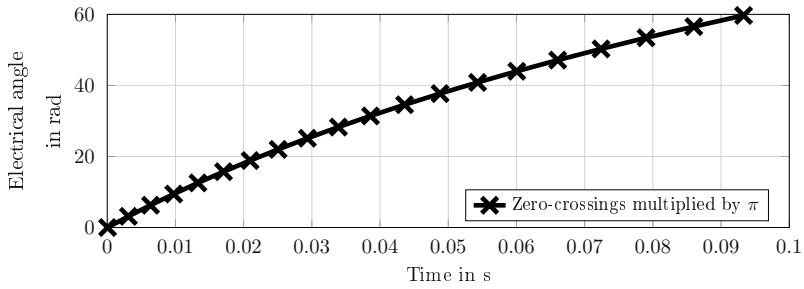Figure 4.16: Simulated induced voltage during power-off with marked zero-crossings

Figure 4.17: Electrical angle over time based on the detected zero-crossings

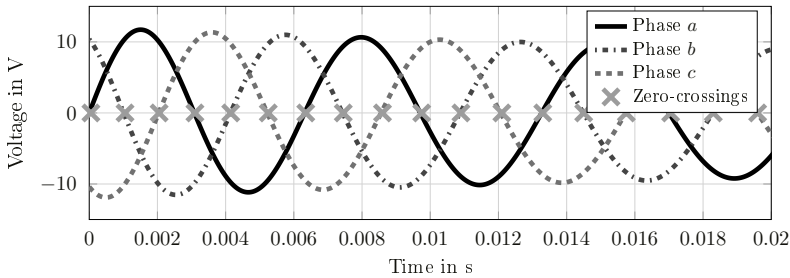$$\hat{\varphi}_{\text{el}}(t) = \sum_{i=0}^{n} a_i t^i, \tag{4.31}$$

Figure 4.18: Induced voltage during power-off for three phases with marked zero-crossings

with $i \in [0,n] \in \mathbb{N}_0$ and $n \in \mathbb{N}_0$, one can easily determine the velocity for the measured period by differentiating (4.31), yielding

$$\hat{\omega}_{\mathrm{el}}(t) = \frac{\mathrm{d}}{\mathrm{d}t}\hat{\varphi}_{\mathrm{el}}(t) = \sum_{i=1}^{n-1} i a_i t^{i-1} \, . \tag{4.32}$$

The angular velocity at time $t = 0$ is given as

$$\hat{\omega}_{\mathrm{el}}(0) = \frac{\mathrm{d}}{\mathrm{d}t}\hat{\varphi}_{\mathrm{el}}(0) = a_1 \, . \tag{4.33}$$

Utilizing (4.32) and (4.33), the measured voltage can be rescaled to a corresponding signal with the velocity $\hat{\omega}(0)$

$$\hat{u}_{\mathrm{i},\hat{\omega}_{\mathrm{el}}(0)}(t) = u_{\mathrm{i}}(t)\frac{\hat{\omega}(0)}{\hat{\omega}_{\mathrm{el}}(t)} \, , \tag{4.34}$$

and a period length of

$$T_{\hat{\omega}_{\mathrm{el}}(0)} = \frac{2\pi}{\hat{\omega}_{\mathrm{el}}(0)} \, . \tag{4.35}$$

Last step consists in fitting the original time-axis to a time-axis consistent with $\hat{\omega}_{\mathrm{el}}(0)$ as

$$t_{\hat{\omega}_{\mathrm{el}}(0)} = T_{\hat{\omega}_{\mathrm{el}}(0)}\frac{\hat{\varphi}_{\mathrm{el}}(t)}{2\pi} \, . \tag{4.36}$$

Due to the fact that the new time axis $t_{\hat{\omega}(0)}$ is not equally spaced, $\hat{e}_{\hat{\omega}(0)}(t)$ has to be interpolated to an equidistant time axis before performing an FFT of the signal. Requirements regarding sampling rate for this time-axis are outlined in the following section.

During idle time of the controller, a FFT of (4.34) can be performed, yielding the amplitude a_{n} and phase angle φ_{n} of the n-th harmonic.

4.2.2 Implementation

Several factors have to be considered for series implementation of the described algorithm. Different requirements regarding computing power and additional hardware can be derived, depending on what application the method is used for, and for which of the aforementioned scenarios it is employed.
The results of the algorithm were evaluated by comparison of the determined induced voltage shape with a reference signal measured with a 12-bit oscilloscope at the test bench. For graphical illustration, the residual between the reference and the reconstructed signal was built. In addition, the root mean square of both signals were compared to each other.

Several issues have to be dealt with, when implementing the described algorithm. First of all, due to possible asymmetries attached to the electromagnetic circuit, the shape of the flux linkage over angle can vary between the three phases. The rms-values of one complete electrical period for each phase (measured with an oscilloscope) are shown in Table 4.1. As can be seen, they differ slightly. The difference, however, is very small and is thus

Table 4.1: Measured rms-value of induction voltage over one electrical period for all phases.

Phase	a	b	c
rms in V	8.97	8.98	9.02

neglected. Furthermore, the zero-crossing during one electrical period can be at a position slightly different than 180°, which can result from a misaligned magnetization head. This, as a consequence, reduces the available number of zero-crossings for the polynomial approximation according to (4.31). The relative angle between two phases, however, is fixed to 60°, i.e., starting from the first zero-crossing found, the following angles can be used for approximation: 0°, 60°, 120°, 360°, 420°, 480°...

For determination of the induced phase voltages at the test bench a differential measurement of the motor terminal voltages is carried out. Retrieving the phase voltages u_{uv}, u_{vw} and u_{wu} requires subtraction of the corresponding terminal voltages in software. During the measurement procedure at the test bench the associated electronic unit is disconnected from the motor. This is obviously not possible during measurement in the field. Despite all six MOSFETS of the B6-bridge being open, the anti-parallel diodes interfere with the voltage measurement by clamping negative voltages below the corresponding threshold voltage. This results in distorted measurements, as depicted in Figure 4.19. As this effect is symmetrical for all three phases it is canceled-out by the subtraction required for determination of the phase voltages.
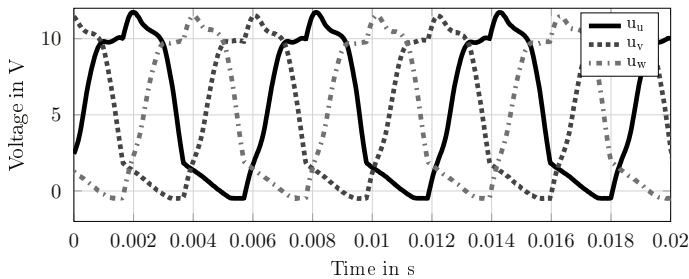

Figure 4.19: Terminal voltages distorted by connected electronics unit

The used Analog-to-Digital (A/D)-converter, however, cannot deal with negative voltages which requires a slight modification of the hardware setup used for measurement as shown in Figure 4.20. For a more compact illustration, the required layout is only shown for one terminal voltage. The MOSFET's are not shown in the figure as they are in high-impedance state during measurement. The proposed modification adds a constant offset of 1V to the measurement resulting in the ability to measure voltages in the range of $-1\,\mathrm{V}$ to $u_{i,max}$. The additional offset can be switched on and off with the DSP, resulting in a low bias-current when the measurement is disabled.
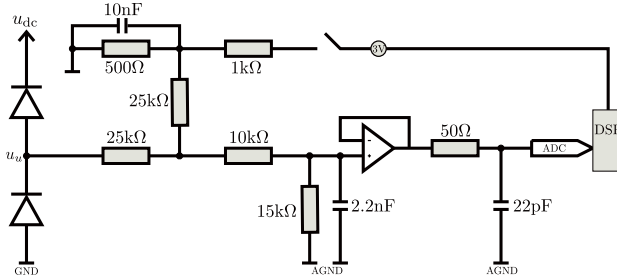
Figure 4.20: Hardware setup for voltage measurement

Table 4.2: Frequency response of first order low-pass filter used for measurement. Base angular frequency $\omega = 1048\,\mathrm{rad\,s^{-1}}$.

Harmonic	Damping	Phase shift in °
1	1.000	-1.18
2	1.000	-2.37
5	0.995	-5.90
7	0.990	-8.23

From Figure 4.20, the cutoff-frequency of the first-order low-pass filter before the A/D-converter can be calculated to $f_\mathrm{c} = 8\,\mathrm{kHz}$. The corresponding damping ratio and phase shift for relevant frequencies are shown in Table 4.2, the voltage amplitude fraction of the harmonics with reference to the fundamental voltage wave for the used motor are illustrated in Figure 4.21. Besides the fundamental voltage wave, the fifth voltage harmonic
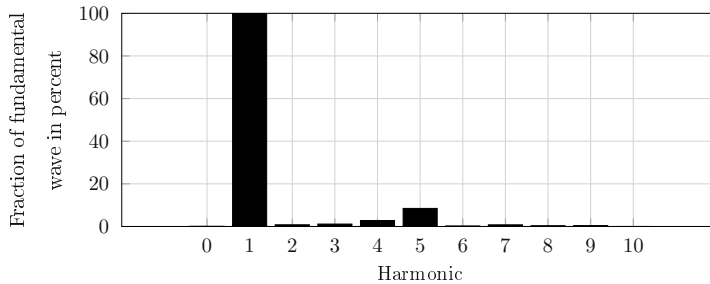

Figure 4.21: FFT voltage spectrum of (4.34): Amplitudes of voltage harmonics as fractions with reference to fundamental wave amplitude

gives a contribution to the amplitude of the induced voltage. However, despite the phase shift of $-5.90°$ for the fifth harmonic caused by the low-pass filter, its influence was neglected for the proposed method. Due to component tolerances, the real values for damping and phase shift can differ from the ones given in Table 4.2. Furthermore, the

values change over temperature, resulting from changed resistance values. Accounting for these changing values would require a large application effort, which poses contradictory to the goal which states the reduction of application costs.

4.2.3 Results

Results for scenario one (strong deceleration during power-off due to very low rotor inertia and active braking) and scenario two (slow deceleration during power-off in the field with high inertia due to fan attached) are depicted in Figure 4.22 and Figure 4.23. The top plot of the figures displays the first and fourth electrical period during the power-off procedure. The second plot shows the recorded signal and the signal converted to constant speed according to (4.33). The third and fourth plot give a comparison between a reference signal measured with a drive operated under constant speed and the reconstructed waveform. The reference signal was acquired on the test-bench with a 12-bit oscilloscope and a sampling rate of 5 µs

The strong deceleration can clearly be observed in the first plot in Figure 4.22, which shows a higher cycle time for the fourth compared to the first period. In comparison, the first and the fourth period in Figure 4.23 have almost the same cycle time. This results in the signal converted to constant speed in the second plot of Figure 4.23 being fully covered by the shape of the recorded waveform.

Evaluation of the algorithm revealed, that phase angles determined for the harmonics show a large deviation to the reference values acquired on the test-bench with an oscilloscope. Furthermore, the deviation between the three phases a, b and c is different, caused by different frequency responses of the low-pass filters shown in Figure 4.20. Due to the low reliability of the phase angle determination, only the amplitudes of the different harmonics will be considered in the following. This also applies to the demagnetization detection, which solely relies on the amplitudes and does not evaluate any changes of the phase angles (see Section 5.2).

The rate, with which the sampling of the measurements is performed, has a strong influence on the accuracy of the results. The illustrations in Figure 4.23 and Figure 4.22 are both based on measurements with a sampling rate of 10 µs. For both cases, the exact zero crossing times are reconstructed with linear interpolation.

The higher the sampling rate, the higher the consumed memory space. The deterioration of the rms-value, when reducing the number of required points by 5, i.e. sampling with 50 µs, is illustrated in Table 4.3. For scenario 2, i.e. a power-off procedure in the field with a high inertia attached, the deviation of the rms-values is acceptable for both sampling rates. However, determination of the flux linkage over angle with an EoL-test with active braking (scenario 1), shows a deviation of 9.2 % for a sampling rate of 50 µs. Diagnosing a demagnetization is still possible when measuring with a sampling rate of 50 µs (as demonstrated in Section 5.2), however, a deviation of 9.2 % makes a torque calculation as required for detection of unusual load conditions very inaccurate. For applications requir-
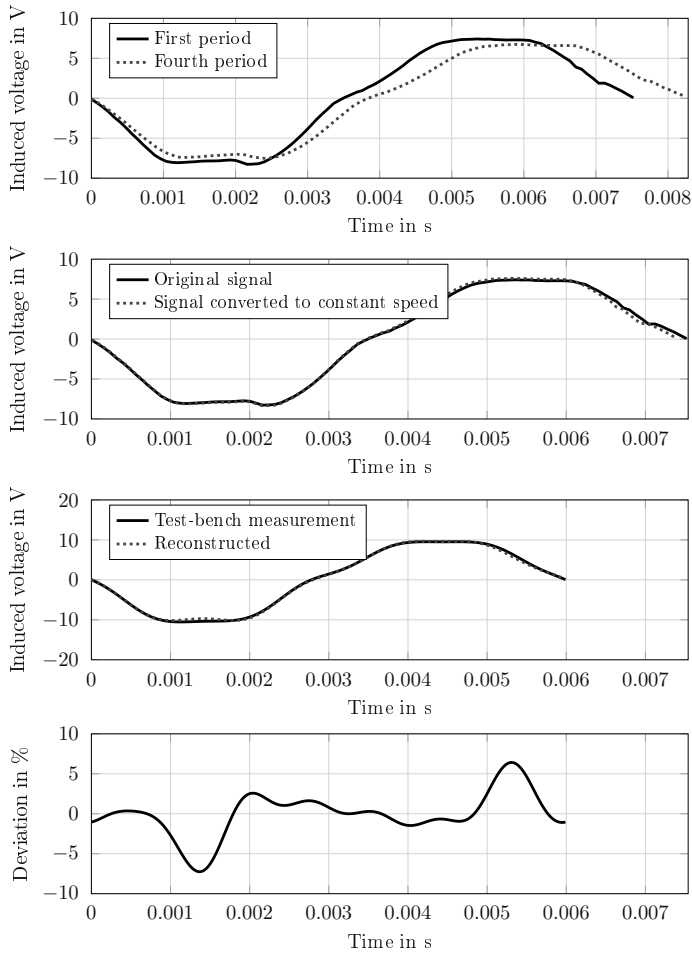
Figure 4.22: Results of a reconstruction of the induced voltage for a strong deceleration with active braking (scenario 1). Deceleration was set to $8000\,\mathrm{min}^{-1}\,\mathrm{s}^{-1}$. First plot: First and fourth period during power-off procedure. Second plot: Recorded signal and signal converted to constant speed. Third and fourth plot: Comparison between reference signal and reconstructed waveform.
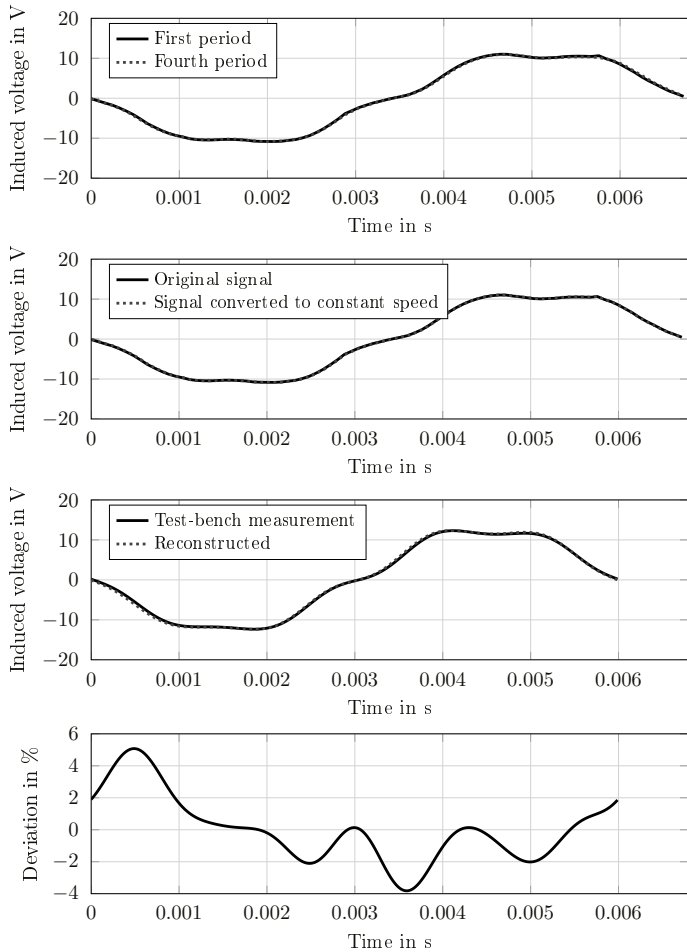
Figure 4.23: Results of reconstruction of the induced voltage for a slow deceleration in the field with high inertia (scenario 2). First plot: First and fourth period during power-off procedure. Second plot: Recorded signal and signal converted to constant speed. Third and fourth plot: Comparison between reference signal and reconstructed waveform.

Table 4.3: Deviation of rms-value of induced voltage to reference with different sampling rates.

	Scenario 1		Scenario 2	
Sampling rate	$10\,\mu s$	$50\,\mu s$	$10\,\mu s$	$50\,\mu s$
Deviation of rms to reference in percent	2.9 %	9.2 %	0.3 %	0.8 %

ing torque calculation, it is thus recommended to use a sampling rate of $10\,\mu s$. As only three voltage values have to be acquired and stored in the memory for each time step, this does not place great demand on computing power, but it increases the required memory space.

4.2.4 Conclusion

A method was presented for determination of the flux linkage over angle by measurement of the induced voltage during a no-load operation of the drive, which can be used for torque calculation and demagnetization detection. The algorithm is able to cope with typical power-off scenarios of the engine cooling fan and the sole electrical motor, i.e. it can be used for reconstruction of the flux linkage with and without an attached fan. The demonstrated scenarios include an EoL-run with active braking (only electric motor, no fan attached) and a normal power-off in the car with high inertia due to the attached fan. Despite neglection of damping and phase shift caused by the filtering process, the presented method shows a good accuracy for the reconstructed induced voltage. It has to be noted, though, that only the amplitudes of the harmonics could be reliably determined. The phase angles showed a large deviation between the individual phases, which is due to the different frequency responses of the low-pass filters used for measurement of the line-to-line voltage.

As is illustrated in Table 4.3, the sampling rate does not have a significant impact on the results for scenario 2. In contrast, the deviation of the reconstructed rms-value to the reference rises to 9.2 % for a sampling rate of $50\,\mu s$, when considering scenario 1. The sampling rate should thus be chosen according to the specified application. For an accurate torque calculation a sampling rate of $10\,\mu s$ is recommended, whereas, as will be demonstrated in Section 5.2, for detecting a demagnetization event a lower sampling rate is sufficient.

4.3   Equivalent Series Resistance of the DC-Link Capacitor

Main function of the DC-link capacitor of the B6-bridge (see Figure 3.5) is the storage of energy, the quick delivery of high currents and smoothing of the DC-bus voltage. Due to its high capacity per volume and low cost, electrolytic capacitors are usually employed for low-voltage automotive applications (Ma and Wang, 2005). They do, however, have some disadvantages like high sensitivity to excessive temperature and low reliability (Lee et al., 2008). Compared to other electronic devices, the electrolytic capacitor has the shortest lifespan and is the most frequent cause of failure (Harada et al., 1993; Ma and Wang, 2005; Wechsler et al., 2012). As Lee et al. (2008) point out, operation of a weakened capacitor implicates an increased risk of further deterioration up to complete failure or, in some cases, rupture or explosion. A method, which is capable of determining the current health status of the capacitor in the field, is therefore highly desirable.

The following section describes the structure and the equivalent circuit model of an electrolytic capacitor, gives an explanation of the wear-out mechanism that leads to failure of the capacitor and presents a method suitable for determination of the equivalent series resistance during standstill of the drive.

4.3.1   Structure and Degradation Mechanism of the Electrolytic Capacitor

The structure of an aluminum electrolytic capacitor is shown in Figure 4.24 (based on Kim et al., 2012). It is composed of two electrodes in the form of aluminum foils. Both the anode and the cathode are etched to increase the effective surface area. The dielectric is a thin layer of aluminum oxide AL_2O_3 and is chemically grown on the anode by a process called formation. Between the anode and the cathode a paper is inserted which is soaked with the electrolyte, an ionic solution.

The first capacitance is between the anode foil and the electrolyte. Just as the dielectric insulates the anode from the electrolyte, so the cathode is insulated as well from the electrolyte by a thin oxide layer, which is formed on the surface of the cathode. The second capacitor therefore is between the electrolyte and the cathode foil (CDM Cornell Duilier, 2013). The total capacitance is the series connection of the two described capacitors.

Based on Figure 4.24, a equivalent circuit model of the capacitor can be derived as depicted in Figure 4.25(a). In Figure 4.25(a), R_{sp} is the resistance due to the liquid electrolyte and the ohmic losses of the connecting wires, R_p models the resistance caused by the dielectric loss and L_{ESL} is the equivalent series inductance induced by connecting wires and coiled aluminum foliage. Due to its small value (typical less than 2 nH), the equivalent series inductance can be neglected (CDM Cornell Duilier, 2013) and a simplified equivalent
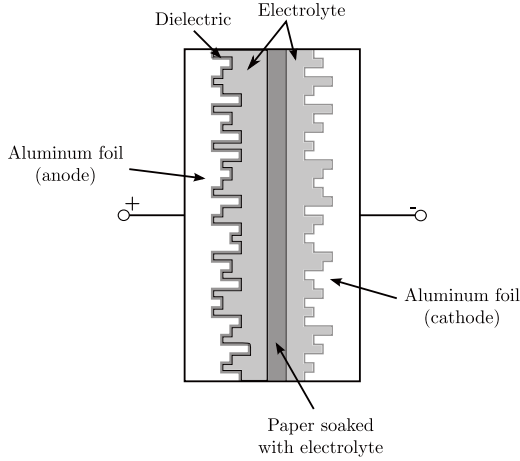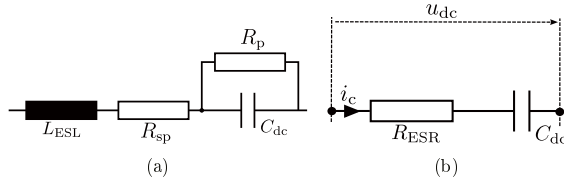
Figure 4.24: Schematic of electrolytic capacitor

Figure 4.25: Equivalent circuit of electrolytic capacitor

circuit model for the capacitor can be drawn (see Figure 4.25(b)). The resistance R_{ESR} is the equivalent series resistance and models all ohmic losses of the capacitor. The equivalent series resistance depends on frequency and temperature according to (see Gasperi (1996))

$$R_{ESR} = R_\sigma(f) + R_{sp}(T) \,, \tag{4.37}$$

with R_σ the equivalent series resistance of dielectric loss

$$R_\sigma(f) = \frac{DF}{2\pi f C} \tag{4.38}$$

and

$$R_{sp}(T) = R_{sp,25°C} 2^{-((\vartheta - 25°C)/A_1)^{B_1}} \,. \tag{4.39}$$

DF is the dissipation factor, which is defined as the ratio between the resistance R_{ESR} and the capacitive reactance X_{dc}

$$DF = \frac{R_{ESR}}{X_{dc}} \,. \tag{4.40}$$

A typical value for the dissipation factor is given in Parler and Macomber (1999) as 0.015. The constants A_1 and B_1 are depending on the used electrolyte. The constants are only known to the manufacturer of the electrolytic capacitor, exemplary values are given in Parler and Macomber (1999) for a 400 V electrolytic capacitor as 40 °C for constant A_1 and 0.6 for constant B_1. The 3d-plane showing the equivalent series resistance in dependence of frequency and temperature is displayed in Figure 4.26. From (4.38), (4.39) and Figure 4.26,
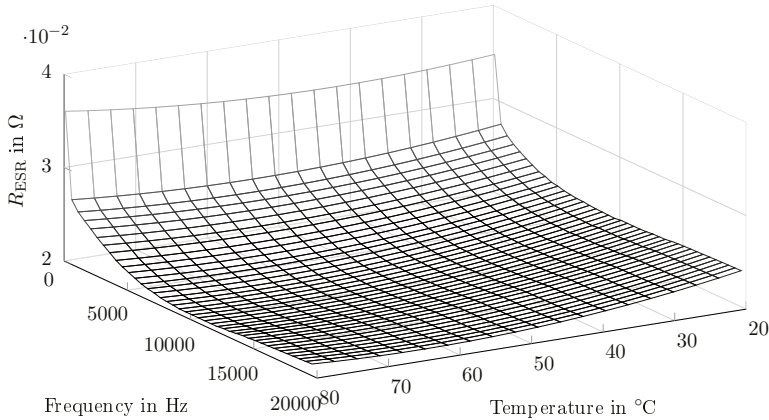

Figure 4.26: Measured frequency and temperature dependence of the equivalent series resistance R_{ESR} (electrolytic capacitor type: Elna RKD 25 V 125°)

it can be seen that the equivalent series resistance decreases with increasing frequency and temperature. This is due to the increased mobility of the ions dissolved in the electrolyte and an increase in the effective surface area, which is caused by the expansion of the electrolyte (Lee et al., 2008).

However, considering a longer time scale, high temperatures lead to the main wear-out mechanism of electrolytic capacitors, which is the vaporization of the electrolyte and loss through the end seals. According to Gasperi (1996), the rate of loss of electrolyte is in direct proportion to its vapor pressure, which is depending on temperature and chemical properties of the electrolyte. The loss of electrolyte increases both the equivalent series resistance and the capacitance. Ripple currents, caused by the high inverter switching frequency, lead to an accelerated wear-out process due to increased heating of the capacitor. In Gasperi (1996), the relationship between the electrolyte volume V and the equivalent series resistance is given as

$$\frac{R_{\text{ESR}}}{R_{\text{ESR,0}}} = \left(\frac{V_0}{V}\right)^2 . \tag{4.41}$$

According to Ma and Wang (2005), a capacitor has reached the end of its life when 40 %
of the electrolyte are lost. Application to (4.41) yields

$$R_{\text{ESR,EndOfLife}} = \left(\frac{V_0}{0.6V_0}\right)^2 \cdot R_{\text{ESR,0}} \approx 2.8 R_{\text{ESR,0}} \,, \tag{4.42}$$

which corresponds to a triplication of the initial value ($R_{\text{ESR,0}}$) of the equivalent series
resistance. Determination of the equivalent series resistance while operating in the car
and comparing to the healthy value measured at the end-of-line, thus is a good indicator
for predicting the current health status of the capacitor.

In the following, a method for determination of the equivalent series resistance is ex-
plained, along with results showing the accuracy of this approach. Results concerning
health diagnosis are outlined in Section 5.1.

4.3.2 Proposed method

The algorithm proposed here is based on the same principle as the injection technique put
forward by Lee et al. (2008). During motor standstill, a short voltage pulse is injected onto
one motor terminal. Due to the configuration of the circuit employed by Lee et al. (2008),
the battery current is zero during discharge of the capacitor, which allows for evaluation
of the equivalent series resistance and capacitance without a sensor measuring the battery
current. However, the circuit topology at hand does not prevent a current flowing from
the battery to the capacitor, so a new approach is presented here.

The switching states for all six transistors during the measurement cycle are shown in
Figure 4.27. During injection ($t \in [t_0, t_1[$), transistors T_1 and T_6 are switched on, resulting
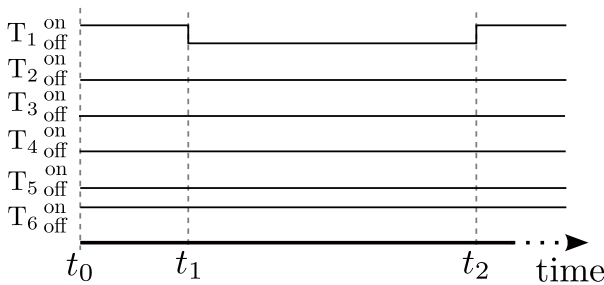

Figure 4.27: Switching states of all six transistors during the measurement cycle

in a current flow i_u as depicted in Figure 4.28. After switching off T_1, the current is
freewheeling through transistor T_6 and diode D_2 (see Figure 4.29). When considering only
the transistors and diodes involved during the measurement cycle, a simplified equivalent
circuit can be derived (see Figure 4.30). The voltage u_{dc}, displayed in Figure 4.25(b), is
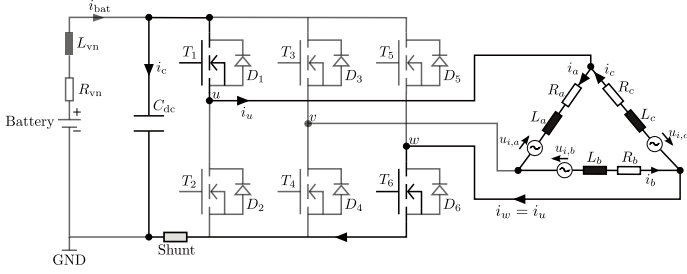
Figure 4.28: Current path during injection ($t \in [t_0, t_1[$)
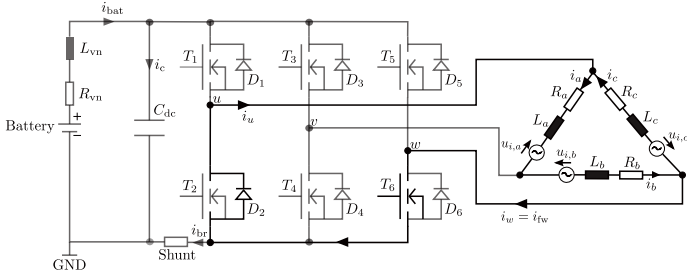
Figure 4.29: Current path during freewheeling ($t \in [t_1, t_2[$)

given as

$$u_{\mathrm{dc}}(t) = R_{\mathrm{ESR}} i_{\mathrm{c}}(t) + \frac{1}{C} \int_{\tau_1}^{\tau_2} i_{\mathrm{c}} dt . \tag{4.43}$$

At time t_1, the capacitor current is reversing, resulting in a voltage jump across the equivalent series resistance (see Figure 4.31). Differentiating (4.43) and evaluating at time t_1 gives

$$\left. \frac{\mathrm{d}u_{\mathrm{dc}}}{\mathrm{d}t} \right|_{t=t_1} = R_{\mathrm{ESR}} \left. \frac{\mathrm{d}i_{\mathrm{c}}}{\mathrm{d}t} \right|_{t=t_1} + \underbrace{\frac{\mathrm{d}}{\mathrm{d}t} \left(\frac{1}{C} \int_{\tau_1=t_1}^{\tau_2=t_1} i_{\mathrm{c}} dt \right)}_{=0} . \tag{4.44}$$

R_{ESR} can then be determined as

$$R_{\mathrm{ESR}} = \left. \frac{\mathrm{d}u_{\mathrm{dc}}}{\mathrm{d}i_{\mathrm{c}}} \right|_{t=t_1} . \tag{4.45}$$

Two problems arise when trying to solve (4.45):

1. Determination of the capacitor current i_{c}, as only the line current i_u can be measured.

2. Sampling of the differential values of $\mathrm{d}u_{\mathrm{dc}}$ and $\mathrm{d}i_{\mathrm{c}}$ at time t_1.
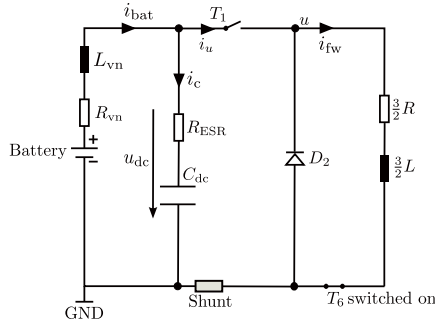
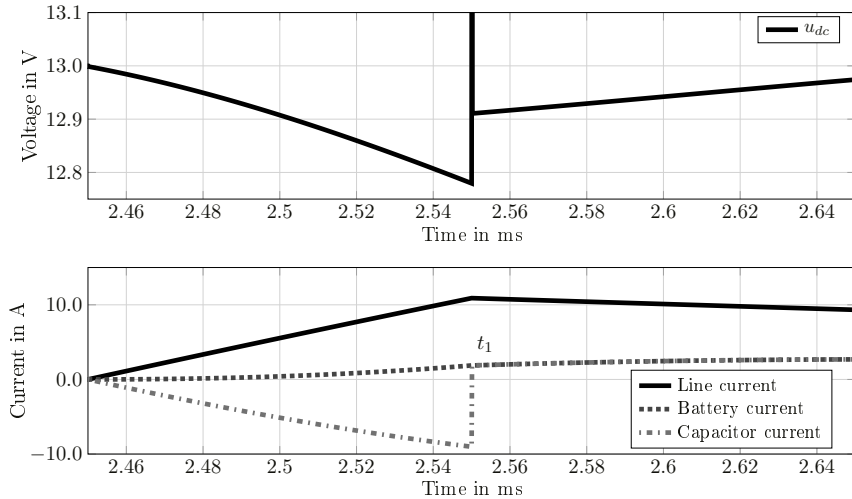Figure 4.30: Equivalent circuit of the inverter during measurement cycle

Figure 4.31: Simulated line, battery and capacitor currents during measurement cycle. Please note that the freewheeling current after t_1 cannot be measured with the circuit topology at hand.

Figure 4.32 displays the association between the battery current i_{bat}, the capacitor current i_{c} and the line current i_u. A simulation result showing the respective currents during the measurement cycle is depicted in Figure 4.31. The switch-off time of transistor T_1 is marked in the figure. It has to be noted, that, due to the position of the „Shunt" (see Figure 4.29), the line current i_u can not be measured for the time interval $t \in [t_1, t_2[$. From Figure 4.32 and Figure 4.28, the capacitor current for $t \in [t_0, t_1[$ can be derived as

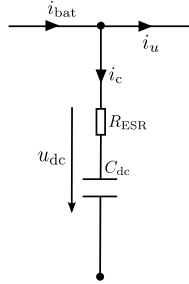$$i_{\mathrm{c}}(t) = i_{\mathrm{bat}}(t) - i_u(t) \,. \tag{4.46}$$

Figure 4.32: Current node of the dc-link

After switching off transistor T_1, the line current freewheels through T_6 and D_2 (see Figure 4.29 and i_{fw} in Figure 4.30), and no current flows from the capacitor to the motor, hence

$$i_c(t) = i_{bat}(t) \qquad \text{for } t \in [t_1, t_2[. \tag{4.47}$$

As can be seen in Figure 4.31, the capacitor current abruptly reverses direction when T_1 is switched off. In comparison, the battery current shows a continuous progression, which leads to the assumption, that the battery current at time t_1 has barely changed compared to point in time $t_1 - \mu$, with μ being an infinitisemal time-step:

$$i_{bat}|_{t_1} \approx i_{bat}|_{t_1 - \mu} , \tag{4.48}$$

and, with (4.47), it follows that

$$i_{bat}|_{t_1} = i_c|_{t_1} \approx i_{bat}|_{t_1 - \mu} . \tag{4.49}$$

Inserting (4.49) into (4.46) yields

$$i_c|_{t_1 - \mu} = i_{bat}|_{t_1 - \mu} - i_u|_{t_1 - \mu} , \tag{4.50}$$

and, with (4.49)

$$i_c|_{t_1 - \mu} = i_{bat}|_{t_1} - i_u|_{t_1 - \mu} . \tag{4.51}$$

With (4.48), (4.51) becomes

$$i_c|_{t_1 - \mu} = i_c|_{t_1} - i_u|_{t_1 - \mu} . \tag{4.52}$$

With

$$\mathrm{d}i_c = i_c|_{t_1} - i_c|_{t_1 - \mu} , \tag{4.53}$$

the capacitor current at time t_1 can thus be expressed by sole measurement of the line current at time $t_1 - \mu$ according to

$$\mathrm{d}i_c|_{t=t_1} = i_u(t_1 - \mu) . \tag{4.54}$$

As can be seen in Figure 4.31, the capacitor inductance L_{ESL} causes a voltage spike when i_c is reversing direction. This spike and the noise caused by the concurrent switching

process of transistor T_1 make it impossible to directly measure du_{dc}. In the following, the technique for determination of the required voltage du_{dc} is described.

The voltage across the transistor is periodically measured during the measurement cycle. Both the voltages before and after switching off transistor T_1 are approximated with a polynomial according to

$$u_{dc,t-}(t) \quad = \quad \sum_{i=0}^{i=n} a_i t^i \qquad \text{for } t \leq t_1 \tag{4.55}$$

$$u_{dc,t+}(t) \quad = \quad \sum_{i=0}^{i=n} b_i t^i \qquad \text{for } t \geq t_1 \,. \tag{4.56}$$

The voltage jump across the transistor caused by the equivalent series resistance is then given as

$$u_{dc}(t_1) = u_{dc,t+}(t_1) - u_{dc,t-}(t_1) \,. \tag{4.57}$$

But still the problem remains, how to determine the switch-off time of transistor T_1. The switching signals are issued by the ECU and, hence, the corresponding times t_0 and t_1 should be known exactly. However, due to the signal propagation time from ECU to the MOSFET gate via the bridge driver and the load and temperature dependent switching behavior of the MOSFETs', the real switching times are attached with uncertainty. A slight deviation in determination of the time t_1 leads to a significant change of the calculated voltage $u_{dc}|_{t_1}$ as shown in Figure 4.33.

The procedure for determination of time t_0 is illustrated in Figure 4.34. The line-current
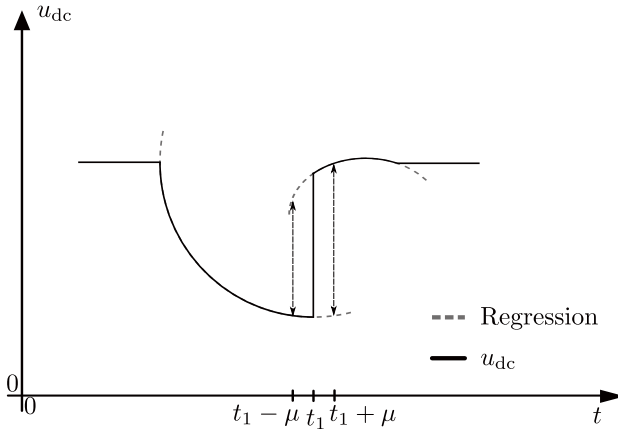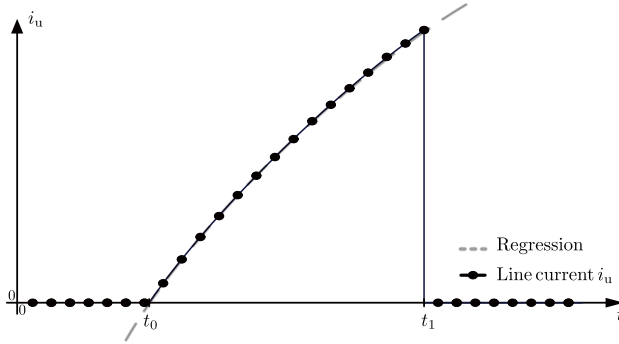

Figure 4.33: Demonstration of error in determination of voltage jump across the transistor due to switching time uncertainty

is periodically sampled during the injection cycle. Based on these measurements, a poly-

Figure 4.34: Curve fitting of line-current for determination of t_0 and t_1

nomial approximation of the line current according to

$$i_u(t) = \sum_{i=0}^{i=n} c_i t^i \qquad \text{for } t_0 \leq t < t_1 \tag{4.58}$$

can be derived. Assuming, that

$$i_u = 0 \qquad \text{for } t < t_0 \,, \tag{4.59}$$

the switch-on time of the transistor can be found by solving

$$0 = \sum_{i=0}^{i=n} c_i t^i \,. \tag{4.60}$$

Assuming further, that the switching delay for the switch-on process equals the delay for the switch-off process, the time t_1 can be calculated with

$$t_1 = t_0 + \chi T \,, \tag{4.61}$$

with χ the duty cycle and T the period length.

4.3.3   Implementation and Results

The correct functioning of the algorithm described was first evaluated by simulation. In the second step, the voltage impulse was injected into a real system on the test-bench. The resulting signals were recorded with an oscilloscope and fed into the algorithm. In the last step, the algorithm was implemented on the microcontroller and evaluated on the test-bench.

Several aspects have to be considered when implementing the algorithm on the microcontroller. As is shown by (4.38), (4.39) and in Figure 4.26, the equivalent series resistance

depends on the frequency that is applied to the capacitor. Furthermore, the injection time has to be chosen such, that the resulting line current does not get too large. The sampling rate of the capacitor voltage and line current also have to be considered in terms of a trade-off between sampling capabilities of the utilized microcontroller on the one hand, and accuracy of the ESR determination on the other hand.

The course of R_{ESR} over frequency for a constant temperature is displayed in Figure 4.35. The values were retrieved by measurement with an RLC-meter Fluke 6304 (test equipment for measuring the inductance, resistance and capacitance of a component). Aging of the capacitors was simulated by drilling holes in the ceramic body of the capacitor to allow for faster vaporization of the electrolyte. For a frequency higher than $\approx$ 10 kHz, the value of the equivalent series resistance stays constant. Considering the application of this method for health diagnosis, a measurement in this frequency area would be the a suitable choice, as a sole offset of the equivalent series resistance compared to the healthy state is an indicator for an aged capacitor. In contrast, determination of the ESR in the falling part of the curve always requires a measurement at exactly the same frequency, as each deviation leads to a different result.
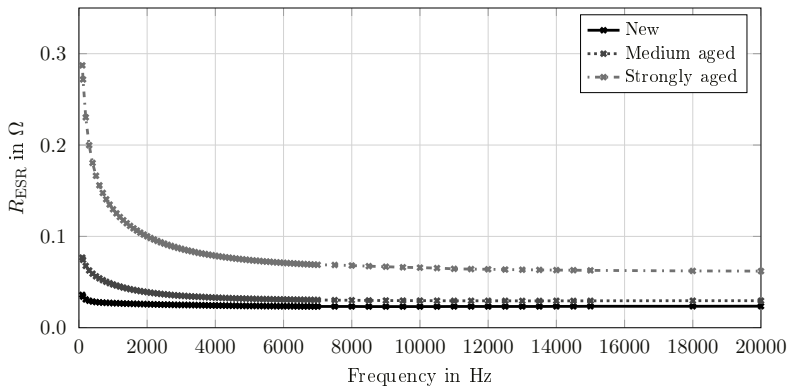
Figure 4.35: Measured equivalent series resistance over frequency for constant temperature (20°)

Times for t_0, t_1 and t_2 have to be chosen such, that the resulting line current does not grow too large, but on the other hand has to be large enough, so that the voltage drop across the transistor is measurable by the microcontroller. For implementation on the utilized hardware an on-time of transistor T_1 was set to 100 µs, the off-time to 4.9 ms. The resulting duty cycle of 2 % allows for the freewheeling current to completely decline between two consecutive measurements. Furthermore, the on-time of transistor T_1 of 100 µs guarantees a measurement with a resulting frequency of 10 kHz.

Voltage and current for a measurement with the parameters described above and evaluated with the microcontroller are shown in Figure 4.36. The corresponding results of the

polynomial approximation are also shown. To eliminate measurement uncertainty, several samples were taken and the mean value was calculated (see Figure 4.37).
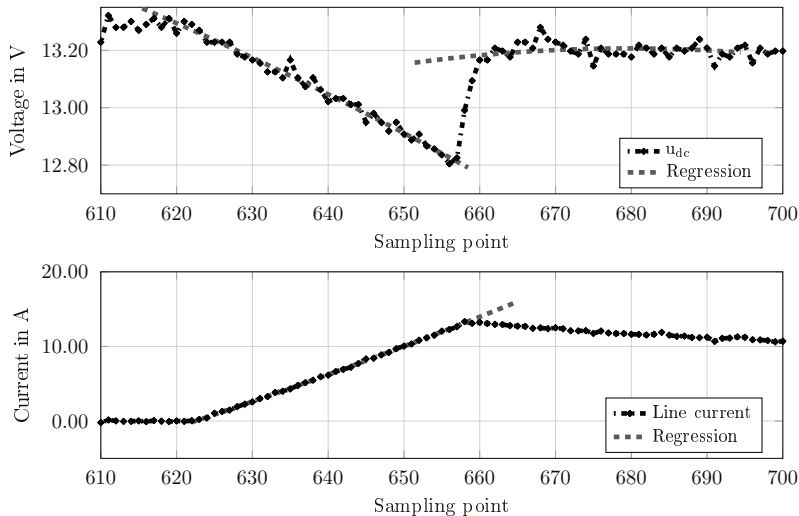
Figure 4.36: Measured line current and DC-link voltage during measurement cycle
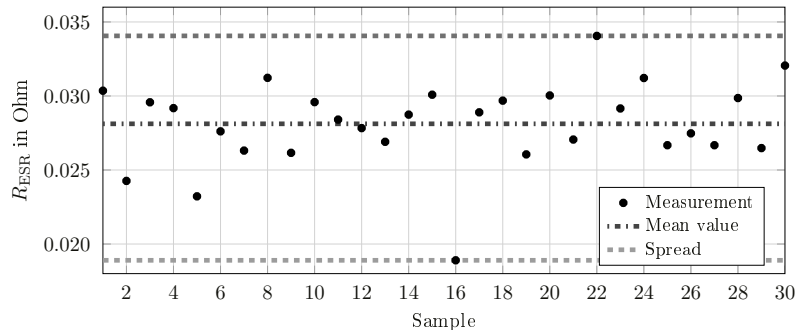
Figure 4.37: Results for several ESR measurements, corresponding mean value, resulting spread and standard deviation

Choice of a proper sampling time is a trade-off between accuracy and hardware limitations set by the used microcontroller. Results for different sampling rates are given in Table 4.4. The obtained result was compared to the measurement conducted with an RLC-meter (type Fluke 6304). It can be seen, that increasing the sampling rate also significantly increases the relative error of the measurement. However, considering (4.41), and, as will

Table 4.4: Comparison of R_{ESR} calculation performed with microcontroller (DSP) to measurement with RLC-meter for different sampling times

Sampling time	RLC-meter	DSP	Absolute deviation	Relative error
4 µs	$0.0296\,\Omega$	$0.0286\,\Omega$	$1.0\,\mathrm{m}\Omega$	$3.37\,\%$
10 µs	$0.0296\,\Omega$	$0.0312\,\Omega$	$1.6\,\mathrm{m}\Omega$	$5.12\,\%$
15 µs	$0.0296\,\Omega$	$0.0332\,\Omega$	$3.6\,\mathrm{m}\Omega$	$10.84\,\%$
20 µs	$0.0296\,\Omega$	$0.0348\,\Omega$	$5.2\,\mathrm{m}\Omega$	$14.94\,\%$

be shown in Section 5.1, even a sampling rate of 20 µs is sufficient for the determination of the health status of the capacitor.

4.3.4   Conclusion

A method suitable for the determination of the equivalent series resistance of the DC-link capacitor was presented in this chapter. The algorithm relies on measuring the voltage across the capacitor and solely utilizes the measurement of the line current. It is characterized by a low computing effort, as only simple polynomial functions have to be approximated. Similar to the method for reconstruction of the flux linkage over angle, described in Section 4.2, the sampling rate determines the accuracy of the result. The higher the sampling rate, the more accurate the result. The relative error for a measurement with a sampling rate of 4 µs is only 3.37 %, whereas a measurement with a sampling rate of 20 µs shows a relative error of 14.94 % compared to a measurement with an RLC-meter (type Fluke 6304). As is illustrated in Figure 4.53, the value of the equivalent series resistance will be utilized for detection of an aged or damaged capacitor (see Section 5.1).

4.4   Thermal Network for Determination of Magnet Temperature

The trend towards reduction of volume and cutting back of used material implicates smaller thermal capacities for storage of dissipated heat and dissemination to the surrounding environment. A proper thermal management and knowledge about temperatures of critical machine parts is thus highly important. The winding temperature can be determined with the method described in Section 4.1. It can be used to avoid an over-temperature of the windings and for tuning the control algorithm. However, sole knowledge of the winding temperature is not sufficient for proper protection of the electrical machine. The magnet is another critical component, which has to be guarded against a demagnetization event. Depending on the type of magnet used, large currents in connection with low (in case of a ferrite magnet) respectively high (in case of a rare earth magnet) magnet temperature can lead to an irreversible demagnetization. Furthermore, the magnet temperature is required for reliable diagnosis of a demagnetization (see Section 5.2), for proper calculation of the hysteresis losses according to (3.21) and for calculation of the machine torque (see (3.19)).

In the following, the path of the airflow through the engine cooling fan is described and methods for determination of machine temperatures currently employed or described in the literature are explained. Subsequently, a new approch for determination of the magnet temperature is presented, which is based on a continuous online determination of the heat transfer coefficients.

4.4.1   Airflow Through the Engine Cooling Fan

The airflow through the engine cooling fan is very complex and driven by the requirement to cool the major components, which are heat sources, such as the electronics package and the motor stator. A cross section of the stator and rotor including the resulting airflow is illustrated in Figure 4.38 and Figure 4.39, respectively.

The fan air flow and two airflow paths through the cooling fan can be recognized. Airflow path one is required for stator cooling, whereas path two is an additional airflow for cooling of the heatsink of the electronics package. The airflow inside the motor is driven by a radial blower, which is comprised of the rotor and the fan hub. The radial blower itself is constituted of small fins on the inner surface of the fan hub (not shown in Figure 4.39). Together with the rotation of the fan hub, this assembly creates an air pressure difference resulting in the two airflow paths as depicted in Figure 4.39. The motor cooling principle thus is a forced convection cooling of the motor driven by a radial blower inside the fan hub.

Due to the limitations set forth by the test bench (see Section 3.2), the assembly described above could not be exactly emulated on the test bench. For the radial blower principle
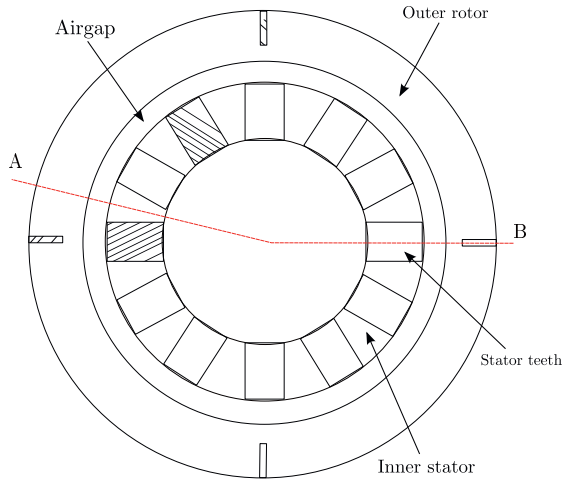
Figure 4.38: Cross section of motor
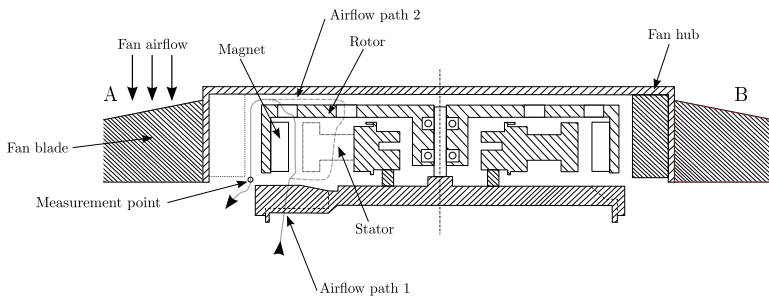
Figure 4.39: Cross section of motor including airflow

to work, the fan hub would have to be assembled, which is not possible, as it makes a permanent measurement of the rotor temperature impossible. Nevertheless, to create a forced convection inside the airgap and the stator, a fan was assembled in front of the motor as illustrated in Figure 4.40. One part of the airflow created by the fan flows around the rotor, the other part enters the rotor through the openings on the outer surface. Measurements were made with an anemometer on an original engine cooling fan with shroud and fan hub attached and on the test bench for comparison of the respective air flow velocities. Measurement points are illustrated in Figure 4.39 and Figure 4.40, measured air velocities are depicted in Table 4.5. The air velocity measured for a fully assembled engine cooling fan is slightly higher than the air velocity measured on the test bench. Furthermore, the direction of the air travelling through the stator and the airgap is different. Although the test bench assembly does not resemble the original setup, it still

causes an airflow in the stator and airgap, resulting in a heatflow influenced by forced convection.
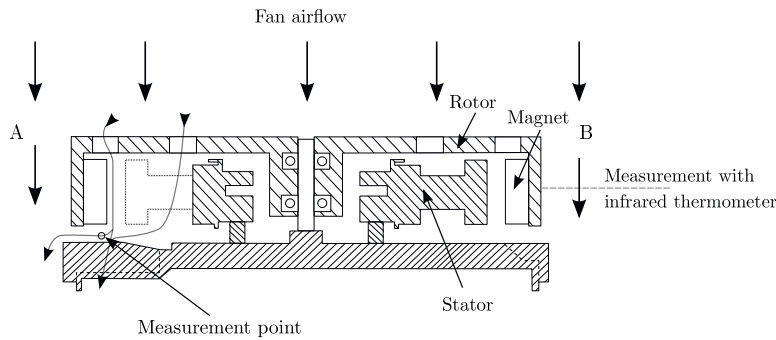
Figure 4.40: Cross section of rotor and stator including airflow as assembled on the test bench (i.e. without shroud and fan hub). The airflow is caused by an additional small fan assembled on the test bench instead of the inertia.

The rotor temperature is measured with an infrared thermometer (see Figure 4.40). The temperature of the magnets, however, cannot directly be measured. In spite of that, the magnet temperature is assumed to equal the rotor temperature, as the heat conductivity between the magnet and the rotor body is very high.

Table 4.5: Measured airflow velocity for engine cooling fan and test bench assembly

Rotational speed (in $\mathrm{min^{-1}}$)	Air velocity, engine cooling fan (in $\mathrm{m\,s^{-1}}$)	Air velocity, test bench (in $\mathrm{m\,s^{-1}}$)
1000	2.3	2.1
1300	3.5	3.1
1800	5.4	4.9
2000	6.2	5.4
2200	7.3	5.8

4.4.2 Thermal Modeling of Electrical Machines

The literature describes two main methods for thermal modeling of electrical machines, analytical lumped-circuit modeling and numerical methods. The latter one can be divided into Finite Element Methods (FEM) and Computational Flow Dynamics (CFD). As is pointed out by Boglietti et al. (2009), both FEM and CFD suffer from a long model setup

and high computational demand. Another disadvantage of FEM is, that the accuracy of its results strongly depends on the assumptions made for the algorithms covering convection boundaries. Main advantage of FEM, according to Boglietti et al. (2009), is its ability to give highly accurate results for solid component conduction. The prediction of flow in complex regions, like the end-windings, is an area strongly suited for CFD. The results obtained from CFD-simulations can be used for tuning the underlying assumptions made for setting up the FEM-model.

The analytical approach lumps together areas of the machine with the same temperature. A node is assigned to each of these areas, and they are interconnected by thermal resistances representing the heat flow between the nodes. Lumped circuit models are computationally less expensive compared to the numerical methods, but require much experience for suitable discretization of the electrical machine into thermal nodes. Furthermore, the results depend on the correct parametrization of the resistances. Boglietti et al. (2008) and Staton et al. (2005) give advice on correct determination of resistance values for some challenging parts of the machine, like the convection from the housing to the surface or the heat transfer in the air-gap. Both papers assume a model discretization suitable for machine simulation during design phase, i.e. a network with fifty or more nodes. Computation of these networks is still too demanding for online implementation in a microcontroller. A more simplified network is presented in Chowdhury and Baski (2010), which use 21 nodes for modeling of the machine, which is still too large for simulation on a controller.

A model suitable for online implementation is given in Duran and Fernandez (2004), Vetter (1988), Wolfram (2002), Schröder (2009) and Leonhard (2001). All references mentioned above assume a model with only two nodes, one for the stator and one for the rotor. While the usage of constant values for the thermal resistances is prevalent, Duran and Fernandez (2004) describe a model with speed-dependent resistance values ($R = \frac{1}{G}$) according to

$$G = G_0(1 + b\omega),\tag{4.62}$$

with G the thermal conductance, b the variation coefficient with motor speed and ω the motor speed. For determination of the corresponding parameters, six tests have to be conducted, as outlined in Moreno et al. (2001). Although determination of the parameters is straightforward, it nevertheless represents an additional application effort. More significant, however, is the fact that lumped circuit models suitable for online implementation do not account for forced convection in the air-gap, which render them unsuitable for thermal modeling of an engine cooling fan. As illustrated in Figure 4.39, a constant axial throughflow is present in the air-gap and inside the stator due to the radial blower in the fan hub.

Literature about forced convection in the air-gap is very scarce. Based on experiments with hot wire anemometry and flow visualization, Becker and Kaye (1962) reported, that a configuration with a rotating inner cylinder yields four different modes of flow. The first mode represents a purely laminar flow, the second mode a laminar flow with Taylor

vortices, the third one a turbulent flow with vortices and the fourth mode a purely tur-
bulent flow. For a detailed description of Taylor vortices see Taylor (1923). Calculation of
the thermal resistance values for each of the modes is given in Howey et al. (2012). The
boundaries of the individual modes are defined by the Reynolds-number, which depends
on the rotational speed, the kinematic viscosity and the axial velocity of the air. Further-
more, Howey et al. (2012) point out, that the transition between the individual modes is
also depending on the machine design, e.g. if there are salient poles or not. Determination
of the resistance values covering forced convection in the air-gap thus requires extensive
and laborious experiments, which have to be repeated for each new application or motor
design (Benecke (1966)).

4.4.3   MIMO Model with Observer Structure

A simplified schematic of the motor is illustrated in Figure 4.41, modeling the inner stator,
the outer rotor and the airgap as single thermal masses. When modeling the airgap as a
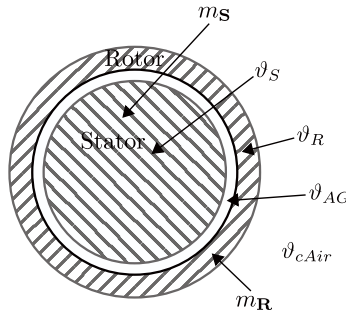
Figure 4.41: Schematic view of motor

thermal mass, the simplified thermal behavior of the system, given in Figure 4.41, can be
split-up into three subparts. The heatflow to the airgap, which originates from the power
loss in the stator (mainly the windings) can be described by

$$
\begin{aligned}
m_{\mathrm{S}}c_{\mathrm{S}}\frac{d\vartheta_S}{dt} &= \dot{Q}_{in} - \dot{Q}_{out} = \\
&= P_{\ell}(t) - \gamma_{\mathrm{S,AG}}A_{\mathrm{S}}(\vartheta_{\mathrm{S}} - \vartheta_{\mathrm{AG}}),
\end{aligned}
\tag{4.63}
$$

with $P_{\ell}(t)$ the copper losses incurred in the stator, $\gamma_{\mathrm{S,AG}}$ the heat transfer coefficient from
the windings to the air inside the airgap, ϑ_{S} the stator temperature, ϑ_{AG} the temperature
of the air in the airgap, m_{S} the mass of the stator, c_{S} the corresponding specific thermal
heat and A_{S} the effective contact area. For the given derivation, heat transfer by means
of radiation was neglected. The heatflow from the airgap to the rotor and from the rotor

Figure 4.42: Block diagram of simplified thermal network for determination of rotor temperature based on measurement of $\vartheta_{\mathrm{cair}}$ and calculation of winding loss P_ℓ

to the ambient air can be described accordingly, and one obtains

$$m_{\mathrm{AG}} c_{\mathrm{AG}} \frac{d\vartheta_{\mathrm{AG}}}{dt} = \gamma_{\mathrm{S,AG}} A_{\mathrm{S}}(\vartheta_{\mathrm{S}} - \vartheta_{\mathrm{AG}}) - \gamma_{\mathrm{AG,R}} A_{\mathrm{Ri}}(\vartheta_{\mathrm{AG}} - \vartheta_{\mathrm{R}}) \tag{4.64}$$
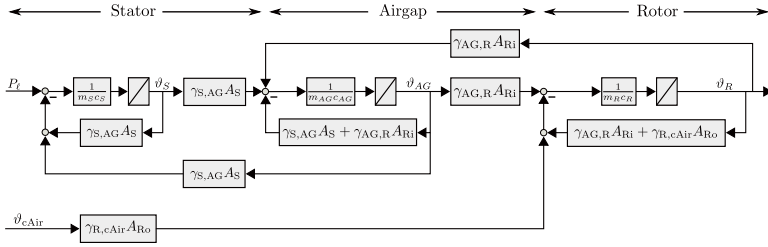
$$m_{\mathrm{R}} c_{\mathrm{R}} \frac{d\vartheta_{\mathrm{R}}}{dt} = \gamma_{\mathrm{AG,R}} A_{\mathrm{Ri}}(\vartheta_{\mathrm{AG}} - \vartheta_{\mathrm{R}}) - \gamma_{\mathrm{R,cAir}} A_{\mathrm{Ro}}(\vartheta_{\mathrm{R}} - \vartheta_{\mathrm{cAir}}) \,, \tag{4.65}$$

with m_{AG}, c_{AG} and m_{R}, c_{R} the mass and specific thermal heat of the air in the airgap and rotor, respectively, $\gamma_{\mathrm{AG,R}}$ the heat transfer coefficient from the airgap to the rotor, $\gamma_{\mathrm{R,cAir}}$ the heat transfer coefficient from rotor to ambient and A_{Ri}, A_{Ro} the effective contact area on the inner and outer side of the rotor, respectively. The corresponding block diagram is displayed in Figure 4.42. For each heatflow a transfer function of first order can be derived as

$$F_{\mathrm{P,S}}(s) = \frac{\vartheta_{\mathrm{S}}(s)}{P_\ell(s)} = \frac{K_{\mathrm{P,S}}}{1 + T_{\mathrm{P,S}} s} \tag{4.66}$$

$$F_{\mathrm{S,AG}}(s) = \frac{\vartheta_{\mathrm{AG}}(s)}{\vartheta_{\mathrm{S}}(s)} = \frac{K_{\mathrm{S,AG}}}{1 + T_{\mathrm{S,AG}} s} \tag{4.67}$$

$$F_{\mathrm{AG,R}}(s) = \frac{\vartheta_{\mathrm{R}}(s)}{\vartheta_{\mathrm{AG}}(s)} = \frac{K_{\mathrm{AG,R}}}{1 + T_{\mathrm{AG,R}} s} \,, \tag{4.68}$$

with $F_{\mathrm{P,S}}$ the transfer function from the power loss source to the stator temperature rise, $F_{\mathrm{S,AG}}$ the transfer function from the stator temperature to the temperature of the air in the airgap and $F_{\mathrm{AG,R}}$ the transfer function from the air temperature in the airgap to the rotor temperature. From (4.63) to (4.65), the corresponding gains and time constants can be derived as

$$K_{\mathrm{P,S}} = \frac{1}{\gamma_{\mathrm{S,AG}} A_{\mathrm{S}}} \tag{4.69}$$

$$T_{\mathrm{P,S}} = \frac{m_{\mathrm{S}} c_{\mathrm{S}}}{\gamma_{\mathrm{S,AG}} A_{\mathrm{S}}} \tag{4.70}$$

$$K_{\mathrm{S,AG}} = \frac{1}{\gamma_{\mathrm{S,AG}} A_{\mathrm{S}} + \gamma_{\mathrm{AG,R}} A_{\mathrm{Ri}}} \tag{4.71}$$

$$T_{\mathrm{S,AG}} = \frac{m_{\mathrm{AG}} c_{\mathrm{AG}}}{\gamma_{\mathrm{S,AG}} A_{\mathrm{S}} + \gamma_{\mathrm{AG,R}} A_{\mathrm{Ri}}} \tag{4.72}$$
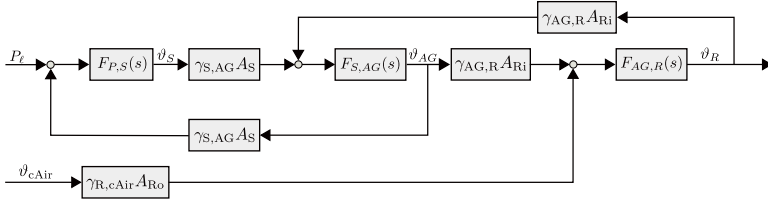
Figure 4.43: Merged block diagram of simplified thermal network

$$K_{\mathrm{AG,R}} = \frac{1}{\gamma_{\mathrm{AG,R}}A_{\mathrm{Ri}} + \gamma_{\mathrm{R,cAir}}A_{\mathrm{Ro}}} \tag{4.73}$$

$$T_{\mathrm{AG,R}} = \frac{m_{\mathrm{R}}c_{\mathrm{R}}}{\gamma_{\mathrm{AG,R}}A_{\mathrm{Ri}} + \gamma_{\mathrm{R,cAir}}A_{\mathrm{Ro}}} \,. \tag{4.74}$$

The merged block diagram is shown in Figure 4.43.

The effective contact areas and the thermal capacities can be obtained from geometry and material properties. Making a test-run on the test bench with measurement of the stator, the airgap and the rotor temperatures only leaves the heat transfer coefficients $\gamma_{\mathrm{S,AG}}$, $\gamma_{\mathrm{AG,R}}$ and $\gamma_{\mathrm{R,cAir}}$ unknown. Estimation of the unknown coefficients based on test-bench measurements and (4.63) to (4.65) results in a very low time constant $T_{\mathrm{S,AG}}$, which is around eight thousand times smaller than $T_{\mathrm{P,S}}$ and $T_{\mathrm{AG,R}}$ for stator and rotor mass. Due to this large imbalance the resulting system is stiff and hence difficult to simulate and unsuitable for parameter estimation.

For subsequent considerations the airgap thermal capacity is thus neglected, resulting in a two-mass model of the electrical machine. Similar to (4.66) to (4.68), the heat flows can be described as

$$m_{\mathrm{S}}c_{\mathrm{S}}\frac{d\vartheta_{\mathrm{S}}}{dt} = P_{\ell}(t) - \gamma_{\mathrm{S,AG}}A_{\mathrm{S}}(\vartheta_{\mathrm{S}} - \vartheta_{\mathrm{AG}}) \tag{4.75}$$

$$0 = \gamma_{\mathrm{S,AG}}A_{\mathrm{S}}(\vartheta_{\mathrm{S}} - \vartheta_{\mathrm{AG}}) - \gamma_{\mathrm{AG,R}}A_{\mathrm{Ri}}(\vartheta_{\mathrm{AG}} - \vartheta_{\mathrm{R}}) \tag{4.76}$$

$$m_{\mathrm{R}}c_{\mathrm{R}}\frac{d\vartheta_{\mathrm{R}}}{dt} = \gamma_{\mathrm{AG,R}}A_{\mathrm{Ri}}(\vartheta_{\mathrm{AG}} - \vartheta_{\mathrm{R}}) - \gamma_{\mathrm{R,cAir}}A_{\mathrm{Ro}}(\vartheta_{\mathrm{R}} - \vartheta_{\mathrm{cAir}})\,, \tag{4.77}$$

Taking ϑ_{S} and ϑ_{R} as system states, and setting P_1 and $\vartheta_{\mathrm{cAir}}$ as inputs, a MIMO state space representation can be derived as

$$\begin{bmatrix} \dot{\vartheta}_{\mathrm{S}} \\ \dot{\vartheta}_{\mathrm{R}} \end{bmatrix} = \begin{bmatrix} a_{11} & a_{12} \\ a_{21} & a_{22} \end{bmatrix} \begin{bmatrix} \vartheta_{\mathrm{S}} \\ \vartheta_{\mathrm{R}} \end{bmatrix} + \begin{bmatrix} b_{11} & 0 \\ 0 & b_{22} \end{bmatrix} \begin{bmatrix} P_{\mathrm{ell}} \\ \vartheta_{\mathrm{cAir}} \end{bmatrix} \tag{4.78}$$

$$y = \begin{bmatrix} 1 & 0 \\ 0 & 1 \end{bmatrix} \begin{bmatrix} \vartheta_{\mathrm{S}} \\ \vartheta_{\mathrm{R}} \end{bmatrix}\,, \tag{4.79}$$

with

$$a_{11} = \frac{1}{m_S c_S} \left(\frac{(\gamma_{S,AG} A_S)^2}{\gamma_{S,AG} A_S + \gamma_{AG,R} A_{Ri}} - \gamma_{S,AG} A_S \right) \tag{4.80}$$

$$a_{12} = \frac{1}{m_S c_S} \left(-\frac{\gamma_{AG,R} A_{Ri} \gamma_{S,AG} A_S}{\gamma_{S,AG} A_S + \gamma_{AG,R} A_{Ri}} \right) \tag{4.81}$$

$$a_{21} = \frac{1}{m_R c_R} \left(\frac{\gamma_{AG,R} A_{Ri} \gamma_{S,AG} A_S}{\gamma_{S,AG} A_S + \gamma_{AG,R} A_{Ri}} \right) \tag{4.82}$$

$$a_{22} = \frac{1}{m_R c_R} \left(\frac{(\gamma_{AG,R} A_{Ri})^2}{\gamma_{S,AG} A_S + \gamma_{AG,R} A_{Ri}} - \gamma_{R,cAir} A_{Ro} - \gamma_{AG,R} A_{Ri} \right) \tag{4.83}$$

$$b_{11} = \frac{1}{m_S c_S} \tag{4.84}$$

$$b_{22} = \frac{\gamma_{R,cAir} A_{Ro}}{m_R c_R} . \tag{4.85}$$

The corresponding block diagram is displayed in Figure 4.44. For determination of the
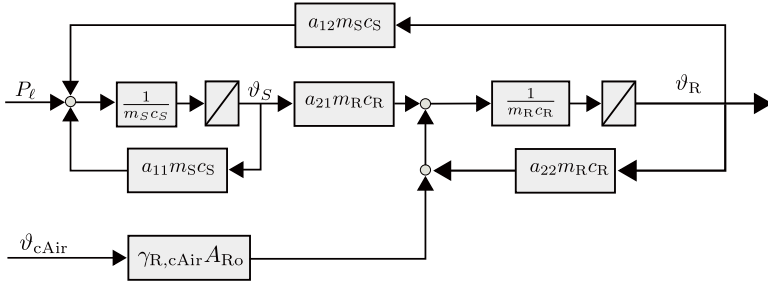
Figure 4.44: Block diagram of the MIMO system, describing the thermal behavior of the stator-rotor system

unknown rotor temperature, the method for measurement of the winding temperature as described in Section 4.1 is exploited. As the copper losses P_ℓ, which serve as an input to the model according to (4.78), are directly incurred in the windings, the winding temperature is assumed to accurately represent the stator temperature. Furthermore, it is assumed that a mean temperature of the air behind the cooler is available, which can be calculated with the equations given in Section 3.1.4.

Taking the Laplace-transform of (4.78), and eliminating the rotor temperature ϑ_R gives the equation

$$s^2 \vartheta_S k_1 + s \vartheta_S k_2 + \vartheta_S k_3 + \vartheta_{cAir} k_4 + s P_l k_5 = P_l , \tag{4.86}$$

with

$$k_1 = -b_{11} a_{22} \tag{4.87}$$

$$k_2 = \frac{-a_{22} - a_{11}}{-b_{11} a_{22}} \tag{4.88}$$

$$k_3 = \frac{a_{11}a_{22} - a_{12}a_{21}}{-b_{11}a_{22}} \tag{4.89}$$

$$k_4 = \frac{-a_{12}b_{22}}{-b_{11}a_{22}} \tag{4.90}$$

$$k_5 = \frac{1}{a_{22}} . \tag{4.91}$$

Transforming (4.86) back into the time domain yields

$$\ddot{\vartheta}_S k_1 + \dot{\vartheta}_S k_2 + \vartheta_S k_3 + \vartheta_{cAir} k_4 + \dot{P}_l k_5 = P_l . \tag{4.92}$$

Only known system states and inputs appear in (4.92), i.e. the stator respectively winding temperature, the temperature of the ambient air and the power loss induced in the windings. The power loss can be calculated with

$$P_l(t) = R_a i_{\mathrm{rms,a}}^2 + R_b i_{\mathrm{rms,b}}^2 + R_c i_{\mathrm{rms,c}}^2 . \tag{4.93}$$

The first and second derivatives required in (4.92) can be determined with a state variable filter (see Appendix C). Based on (4.92), a parameter estimation can then be carried out with the data matrix

$$\mathbf{\Psi} = \begin{bmatrix} \ddot{\vartheta}_S & \dot{\vartheta}_S & \vartheta_S & \vartheta_{cAir} & \dot{P}_l & P_l \end{bmatrix} , \tag{4.94}$$

and the parameter vector

$$\mathbf{\Theta} = \begin{bmatrix} k_1 & k_2 & k_3 & k_4 & k_5 \end{bmatrix} . \tag{4.95}$$

For determination of the magnet temperature ϑ_R, the system given in (4.78) has to be simulated online using the parameters gained from the parameter estimation. Setting $a_{21} = -a_{12}$ (see (4.78)), the parameters of the system and input matrix can be reconstructed as

$$a_{22} = \frac{1}{k_5} \tag{4.96}$$

$$b_{11} = \frac{-k_1}{a_{22}} \tag{4.97}$$

$$a_{11} = k_2 b_{11} a_{22} - a_{22} \tag{4.98}$$

$$b_{22} = \frac{-k_4 b_{11} a_{22}}{a_{11}} \tag{4.99}$$

$$a_{21} = (-k_3 b_{11} a_{22} - a_{11} a_{22}) \frac{1}{a_{11}} . \tag{4.100}$$

With the parameters gained from (4.96) to (4.100), the state space system can be simulated for determination of the unknown rotor temperature ϑ_R. However, besides the input $u(t)$, the state of a system also depends on the initial system state x_0. For the given system,

$$x_0 = \begin{bmatrix} \vartheta_{S,0} \\ \vartheta_{R,0} \end{bmatrix} , \tag{4.101}$$

with $\vartheta_{S,0}$ being the initial stator temperature and $\vartheta_{R,0}$ the initial rotor temperature. The initial stator temperature can be determined with the method described in Section 4.1, but the initial rotor temperature is unknown and cannot be measured. Thus, an observer structure has to be utilized for estimation of the not measurable rotor temperature. The resulting block diagram illustrating the approach is depicted in Figure 4.45.

The system and input matrix $\mathbf{A}$ and $\mathbf{B}$, equal those of the thermal system given in (4.78). Since

$$e = \vartheta_S - \hat{\vartheta}_S \,, \tag{4.102}$$

with $\hat{\vartheta}_S$ the stator temperature estimated by the observer, the observer output matrix is given by

$$\mathbf{C}_{\mathrm{obs}} = \begin{bmatrix} 1 & 0 \\ 0 & 0 \end{bmatrix} \,. \tag{4.103}$$

From Figure 4.45, following equations can be determined:

$$\dot{\hat{\mathbf{x}}} = \mathbf{A}\hat{\mathbf{x}} + \mathbf{B}\mathbf{u} + \mathbf{L}e \tag{4.104}$$

$$e = \vartheta_S - \hat{\vartheta}_S = \vartheta_S - \mathbf{C}_{\mathrm{obs}}\hat{\mathbf{x}} \,, \tag{4.105}$$

which yields for the observer equation

$$\dot{\hat{\mathbf{x}}} = (\mathbf{A} - \mathbf{L}\mathbf{C}_{\mathrm{obs}})\,\hat{\mathbf{x}} + \mathbf{B}\mathbf{u} + \mathbf{L}\vartheta_S \,. \tag{4.106}$$

The same quantities used as inputs for the parameter estimation serve as inputs to the observer, i.e. $\vartheta_{\mathrm{cAir}}$ and P_ℓ. $\vartheta_{\mathrm{cAir}}$ is the mean temperature of the air behind the cooler, which can be calculated with the equations given in Section 3.1.4, P_ℓ is the power loss incurred in the windings according to (4.93).

The underlying principle of the block diagram illustrated in Figure 4.45 thus consists of the following steps:

1. Continuously apply a parameter estimation according to (4.92) to determine the unknown coefficients k_1 to k_5.

2. Based on the determined coefficients k_1 to k_5, calculate the parameters of the system and input matrix ($\mathbf{A}$ and $\mathbf{B}$), i.e. a_{11}, a_{12}, a_{21}, a_{22}, b_{11} and b_{22} as given in (4.96) to (4.100).

3. Recalculate the observer feedback matrix $\mathbf{L}$ based on the new system and input matrices $\mathbf{A}$ and $\mathbf{B}$ by using pole placement (see below).

4. Simulate the observer to determine the not measurable system state ϑ_R.

The observer used here serves as a simulation system and is not used in a closed loop control system. The dynamics of the observer thus should be higher compared to the process itself, resulting in observer poles placed left from the eigenvalues of the process. In the examples given here, the observer poles in the s-plane were placed according to

$$\kappa_{\mathrm{obs}} = 10\kappa_A \,, \tag{4.107}$$

with κ_{obs} the observer eigenvalues, and κ_{A} the eigenvalues of the system matrix $\mathbf{A}$. The eigenvalues of the system matrix $\mathbf{A}$ can be derived by solving

$$\left| s\mathbf{I} - \mathbf{A} \right| = 0\,. \tag{4.108}$$

The parameters of the observer matrix $\mathbf{L}$ are determined with the pole placement technique. As is derived in Föllinger et al. (2008), the poles can be placed by solving

$$\left| s\mathbf{I} - \mathbf{A}^T + \mathbf{C}_{\mathrm{obs}}^T \mathbf{L}^T \right| = (s - \kappa_{\mathrm{obs},1})(s - \kappa_{\mathrm{obs},2})\,, \tag{4.109}$$

with $\kappa_{\mathrm{obs},1}$ and $\kappa_{\mathrm{obs},2}$ the desired observer poles. Since

$$\mathbf{C}_{\mathrm{obs}} = \begin{bmatrix} 1 & 0 \\ 0 & 0 \end{bmatrix}\,, \tag{4.110}$$

the term $\mathbf{C}_{\mathrm{obs}}^T \mathbf{L}^T$ yields an observer matrix of the form

$$\mathbf{L} = \begin{bmatrix} l_{11} & 0 \\ l_{21} & 0 \end{bmatrix}\,. \tag{4.111}$$

Solving (4.109) yields for the observer parameters

$$l_{11} = a_{22} + a_{11} - (\kappa_{\mathrm{obs},1} + \kappa_{\mathrm{obs},2}) \tag{4.112}$$

$$l_{21} = \frac{\kappa_{\mathrm{obs},1}\kappa_{\mathrm{obs},2} - a_{11}a_{22} + l_{11}a_{22} + a_{12}a_{21}}{a_{12}}\,. \tag{4.113}$$

This approach will only work, if the estimator is able to track the parameter changes fast
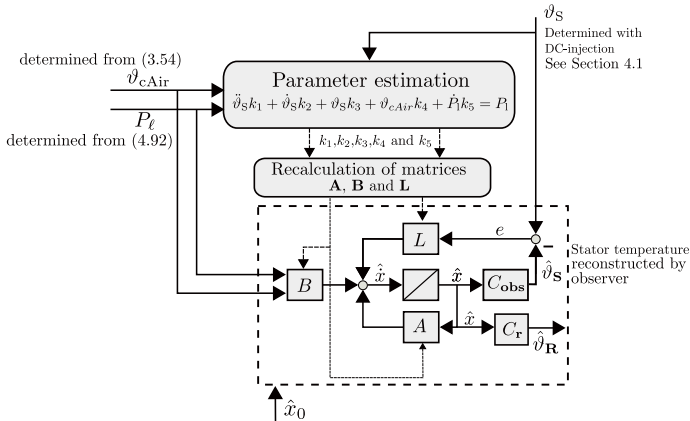

Figure 4.45: Block diagram illustrating MIMO observer with parameter estimation. Aim of the observer is to estimate the not measurable system state ϑ_{R}.

enough. The forgetting factor λ employed within the parameter estimator was thus set to a value smaller than one to allow for a continuous adaption to the changing parameters.

So far, the described approach was presented for the continuous case. Considering the complex observer structure, discretizing the system (4.78) and the estimation equation (4.92) would allow for an easier implementation on a microcontroller. Discretization of (4.92) using a bilinear transformation, which introduces the mapping valid for small sampling times

$$s = \frac{2(z-1)}{T_{\mathrm{s}}(z+1)} , \tag{4.114}$$

with T_{s} the sampling rate and z the z-operator, yields

$$\frac{\zeta_1}{\zeta_7}\vartheta_{\mathrm{S}} z^{-2} + \frac{\zeta_2}{\zeta_7}\vartheta_{\mathrm{S}} z^{-1} + \frac{\zeta_3}{\zeta_7}\vartheta_{\mathrm{S}} z + \tag{4.115}$$
$$\frac{\zeta_4}{\zeta_7}P_{\mathrm{l}} z^{-2} + \frac{\zeta_5}{\zeta_7}P_{\mathrm{l}} z^{-1} + \frac{\zeta_6}{\zeta_7}P_{\mathrm{l}} z =$$
$$= \vartheta_{\mathrm{cAir}} z^{-2} + 2\vartheta_{\mathrm{cAir}} z^{-1} + \vartheta_{\mathrm{cAir}} z ,$$

with

$$\zeta_1 = 4 - 2T_{\mathrm{s}}(-a_{22} - a_{11}) + T_{\mathrm{s}}^2(a_{11}a_{22} - a_{12}a_{21}) \tag{4.116}$$
$$\zeta_2 = -8 + 2T_{\mathrm{s}}^2(a_{11}a_{22} - a_{12}a_{21}) \tag{4.117}$$
$$\zeta_3 = 4 + 2T_{\mathrm{s}}(-a_{22} - a_{11}) + T_{\mathrm{s}}^2(a_{11}a_{22} - a_{12}a_{21}) \tag{4.118}$$
$$\zeta_4 = 2T_{\mathrm{s}}b_{11} + Ts^2 b_{11}a_{22} \tag{4.119}$$
$$\zeta_5 = 2T_{\mathrm{s}}^2 b_{11}a_{22} \tag{4.120}$$
$$\zeta_6 = T_{\mathrm{s}}^2 b_{11}a_{22} - 2T_{\mathrm{s}}b_{11} \tag{4.121}$$
$$\zeta_7 = -a_{12}b_{22} . \tag{4.122}$$

Unfortunately, no closed-form solution for determination of $a_{11}, a_{12}, a_{21}, a_{22}, b_{11}, b_{22}$ can be derived from (4.116) to (4.122), only an iterative solution, which is unsuitable for online implementation. Due to these difficulties, a discrete implementation was not further considered, and the approach was evaluated using the continuous equations.

4.4.4 Results

Several test-runs were conducted on the test bench to evaluate the method explained above. Figure 4.46 shows the measured thermal behavior of the electrical drive on the test-bench for different constant operating points with an additional fan attached to the motor shaft. Along with the stator and rotor temperature also the power loss incurred in the windings and the ambient temperature are displayed. In Figure 4.46 and all subsequent illustrations, the mean winding temperature, determined with thermocouple measurements of all three phases, represents the stator temperature. The rotor temperature is measured with an infrared thermometer. The power loss is calculated according to (4.93), with the current resistance value determined from the winding temperature measurement according to (4.1). The winding loss displayed in Figure 4.46 is subject to two effects. First effect is the change of the resistance due to a rise in the winding temperature according

to (4.1), the second effect is caused by a decrease of the flux linkage of the permanent magnets due to a rise in magnet temperature. From (3.19), it can be seen, that, with a decreasing flux the current has to rise to deliver a constant torque M_{mot}. As is illustrated in Figure 5.2, the temperature coefficient for the individual harmonics of the flux linkage is not the same. However, for approximation of the relation of the power loss induced in the windings at the beginning to the end of the measurement, it is sufficient to assume a constant temperature coefficient of $\gamma_{\mathrm{br}} = 0.2\,\%\,\mathrm{K}^{-1}$ for all harmonics. The power loss induced in the windings at the beginning of the measurement is given as

$$P_{\ell,0} = R_{a,0}i_{\mathrm{rms},a,0}^2 + R_{b,0}i_{\mathrm{rms},b,0}^2 + R_{c,0}i_{\mathrm{rms},c,0}^2 \,. \qquad (4.123)$$

Assuming that $R_{a,0} = R_{b,0} = R_{c,0}$ and $i_{\mathrm{rms},a,0} = i_{\mathrm{rms},b,0} = i_{\mathrm{rms},c,0}$, (4.123) becomes

$$P_{\ell,0} = 3R_0 i_{\mathrm{rms},0}^2 \,. \qquad (4.124)$$

At the end of the measurement, the winding loss yields

$$P_{\ell,1} = 3R_0(1 + \gamma_{\mathrm{cu}}(T_{\mathrm{winding},1} - T_{\mathrm{winding},0}))\,(i_{\mathrm{rms},0}(1 + \gamma_{\mathrm{br}}(T_{\mathrm{mag},1} - T_{\mathrm{mag},0})))^2 \,, \qquad (4.125)$$

with $T_{\mathrm{winding},0}, T_{\mathrm{mag},0}, T_{\mathrm{winding},1}$ and $T_{\mathrm{mag},1}$ the temperature of the winding and the magnet at the beginning and the end of the measurement, respectively. Setting (4.125) in relation to (4.124) yields

$$\frac{P_{\ell,1}}{P_{\ell,0}} = (1 + \gamma_{\mathrm{cu}}(T_{\mathrm{winding},1} - T_{\mathrm{winding},0}))\,(1 + \gamma_{\mathrm{br}}(T_{\mathrm{mag},1} - T_{\mathrm{mag},0}))^2 \,. \qquad (4.126)$$

Applying (4.126) to the first test-run shown in Figure 4.46 with $T_{\mathrm{winding},1} = 60°$, $T_{\mathrm{winding},0} = 28°$, $T_{\mathrm{mag},1} = 34°$, $T_{\mathrm{mag},0} = 28°$ yields

$$(1 + \gamma_{\mathrm{cu}}(T_{\mathrm{winding},1} - T_{\mathrm{winding},0}))\,(1 + \gamma_{\mathrm{br}}(T_{\mathrm{mag},1} - T_{\mathrm{mag},0}) = 1.1383 \,, \qquad (4.127)$$

Taking the values for the power loss at the beginning and the end of the test-run from the diagram as $P_{\ell,1} = 18.2\mathrm{W}$ and $P_{\ell,0} = 16\mathrm{W}$, results in

$$\frac{P_{\ell,1}}{P_{\ell,0}} = 1.1375 \,, \qquad (4.128)$$

which is in accordance with (4.126).

Looking at Figure 4.46, the shortcomings of the test bench (no assembly of fan possible) used for the measurements can clearly be seen. Despite the large power loss, it takes a considerably amount of time for the stator and rotor to warm up, resulting in large time constants. Furthermore, both the rotor and the stator are far from reaching their maximum rated temperature, which lies at $120\,°\mathrm{C}$ and $180\,°\mathrm{C}$ respectively. Reason for this is the temperature of the ambient air, which only shows a slight deviation from its initial state during the whole test-run. Unfortunately, no additional external heat source could be assembled to increase the temperatures.
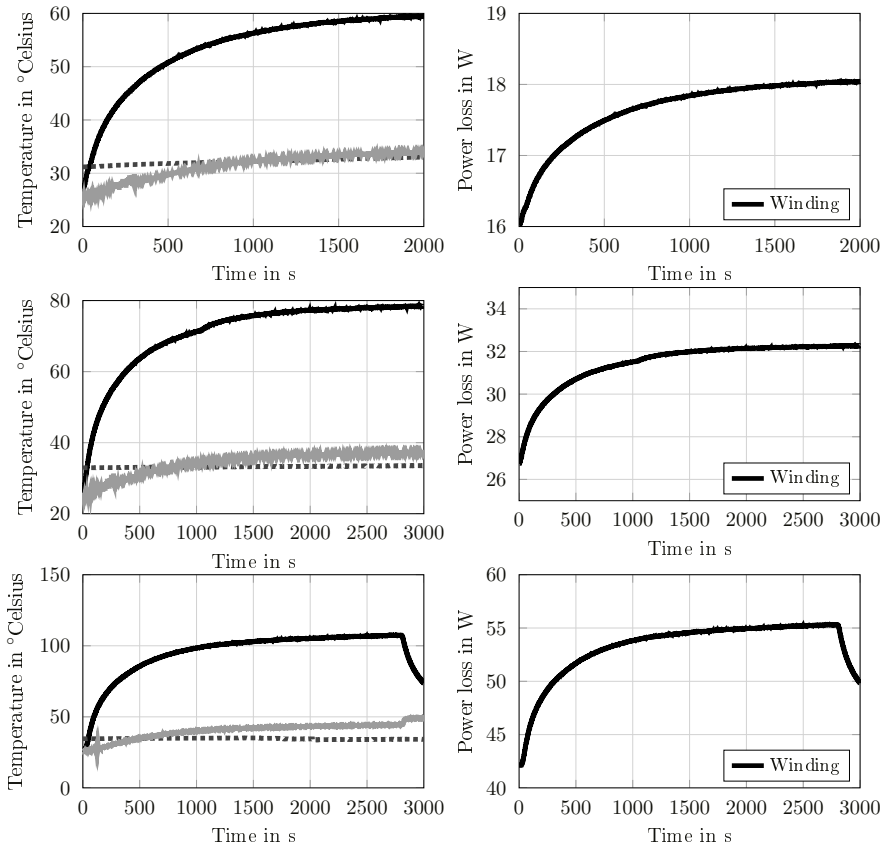
Figure 4.46: Measured temperatures and winding power loss for test-runs on the test bench with different operating points. Top: $1300\,\text{min}^{-1}$@$0.7\,\text{N}\,\text{m}$, middle: $1800\,\text{min}^{-1}$@$1\,\text{N}\,\text{m}$, bottom: $2000\,\text{min}^{-1}$@$1.2\,\text{N}\,\text{m}$. Left-hand diagrams: full black line: stator temperature, straight grey line: rotor temperature, dashed line: ambient air temperature.

Applying the parameter estimation according to (4.92) yields the results illustrated in Figure 4.47, shown for the operating point $2000\,\text{min}^{-1}$@$1.2\,\text{N}\,\text{m}$. Sampling rate for estimation was set to $10\,\text{s}$. It can be seen, that the estimator takes about $300\,\text{s}$ to converge, which is due to the low dynamics inherent to the process.

Deriving the elements of the system and input matrix from the parameter estimates according to (4.96) to (4.100), designing an observer according to (4.107) and feeding the observer with the power loss, the ambient and winding temperature as illustrated in Figure 4.46, yields the results depicted in Figure 4.48. The initial rotor temperature was
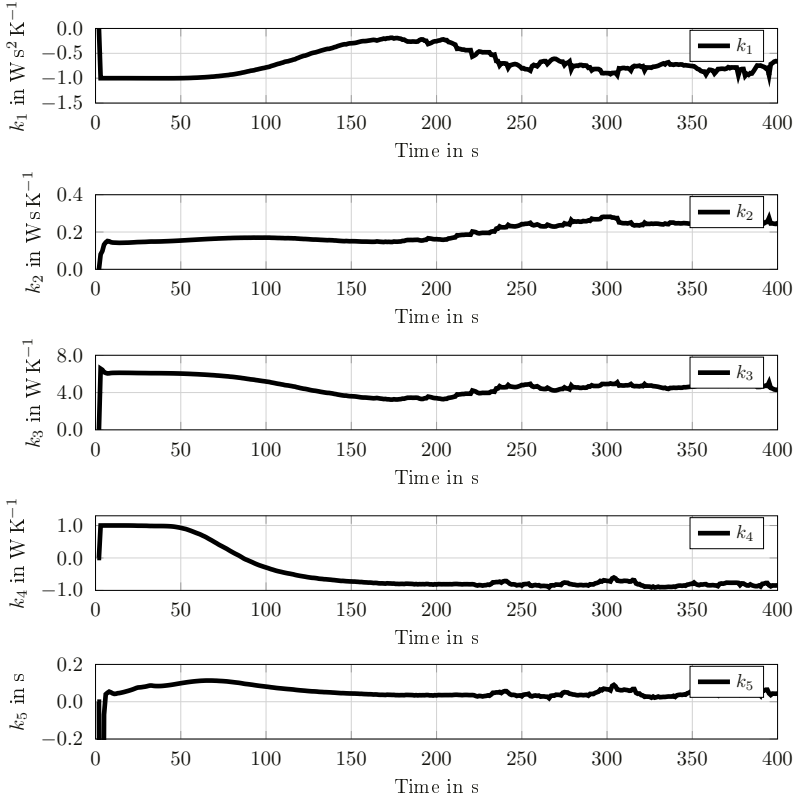
Figure 4.47: Parameter estimates for test-run $2000\,\mathrm{min}^{-1}@1.2\,\mathrm{N\,m}$

deliberately set to a wrong value to demonstrate the effectiveness of the observer. As can be seen, the rotor temperature can be tracked with only minimal deviation of $-4\,\mathrm{K}$ after the observer has settled in.

The effect of a wrong assumption for the initial observer parametrization is illustrated in Figure 4.49. In the beginning, the observer output shows a deviation of around $40\,\mathrm{K}$ compared to the measurement. A new set of parameters for the observer can be calculated after around $350\,\mathrm{s}$, which decreases the deviation to almost zero.

The thermal network as described above is designed for a continuous parameter estimation, i.e. the estimator has to track any parameter changes due to changing input signals instantly. The results displayed in Figure 4.49 indicate, that, for a wrong parametrized estimator, the time required for the parameter estimates to converge is too large to continuously tune the observer. This in turn implies, that, when turning on the engine cooling
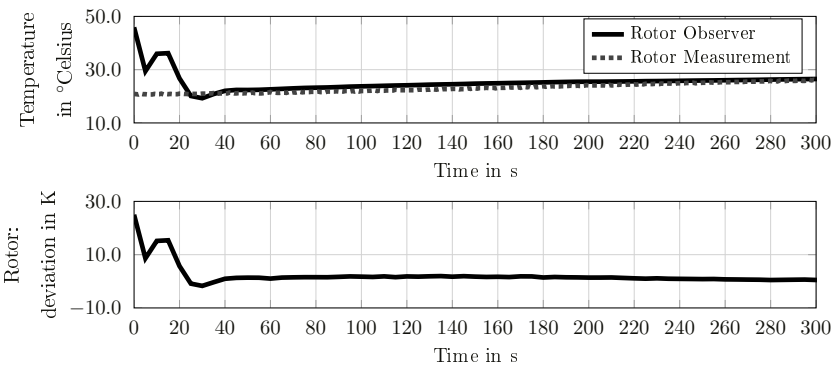
Figure 4.48: Observer output for operating point $2000\,\text{min}^{-1}@1.2\,\text{N m}$. The parameter set for the observer was previously determined, the initial observer state was deliberately set to a wrong value.

fan for the first time, a previously determined parameter set has to be used for the observer. Two disadvantages arise from this necessity. First, the parameter set depends on the operating point and the environmental conditions, such as vehicle speed and ambient air temperature. However, due to the limited memory space, only a small number of parameter sets can be stored in the microcontroller. Consequently, until the estimator has settled in and a new parameter set can be derived, the determined rotor temperature has to be regarded as highly uncertain. Second, the parameter set has to be determined with a test-run in the car, contradicting the initial objective of the presented thermal network, which is to limit application effort to a minimum.
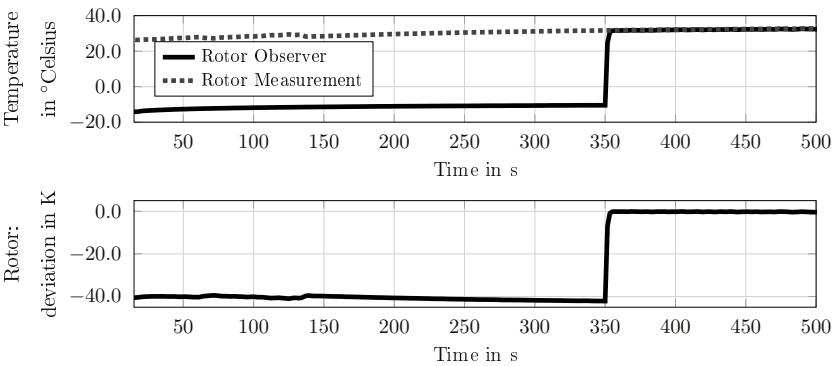

Figure 4.49: Results for determination of magnet temperature with wrong inital parameter set for observer

The principle of the thermal network is to continuously determine new process parameters, based on a parameter estimation according to (4.92). The effects on the parameter estimates after a change of the operating point are illustrated in Figure 4.50. The forgetting factor λ was set to 0.95. Despite the small change in the power loss input, the estimator is significantly disturbed resulting in time spans for convergence equal to the situation depicted in Figure 4.47.
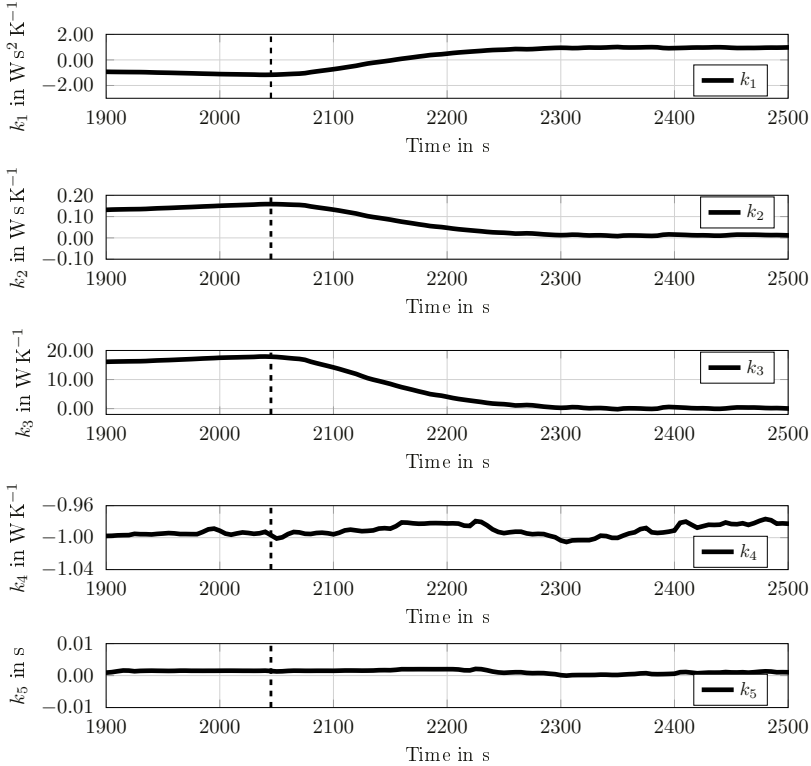
Figure 4.50: Parameter estimates for changing operating point with a forgetting factor $\lambda = 0.95$. The operating point is changed from $1300\,\text{min}^{-1}$@$0.7\,\text{N m}$ to $2000\,\text{min}^{-1}$@$1.0\,\text{N m}$ (time of the operating point change is marked with a vertical line).

The parameter estimates during the settling-in process of the estimator do not yield parameters resulting in a stable observer system. The estimator thus cannot react quickly enough to a change of the operating point, making it impossible to continuously adapt the parameters of the observer. Consequently, the observer parameters can only be adapted to the current operating point after the estimator has converged. Corresponding results are displayed in Figure 4.51.
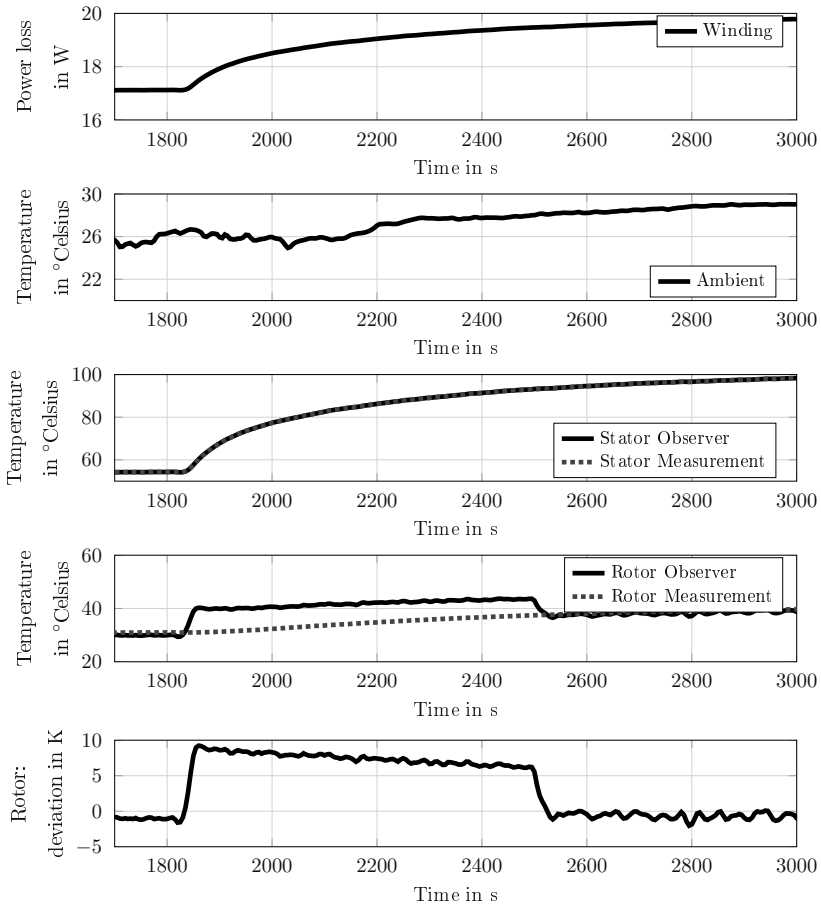
Figure 4.51: Results for adaption of observer parameters after convergence of estimator

It can be seen, that, after a change of the operating point from $1300\,\mathrm{min}^{-1}$@$0.7\,\mathrm{N\,m}$ to $2000\,\mathrm{min}^{-1}$@$1.0\,\mathrm{N\,m}$, tracking of the magnet temperature yields wrong results due to an observer based on a wrong set of parameters. For the shown operating point, the deviation reaches around $10\,\mathrm{K}$. After re-parameterization of the observer, the magnet temperature can again be determined with only a small error. The same approach was used for tracking the magnet temperature in a series of several changes of the operating point as illustrated in Figure 4.52. The same behavior can be observed, however, with a larger deviation of the observer output compared to the measurement during the settling-in process of the estimator.
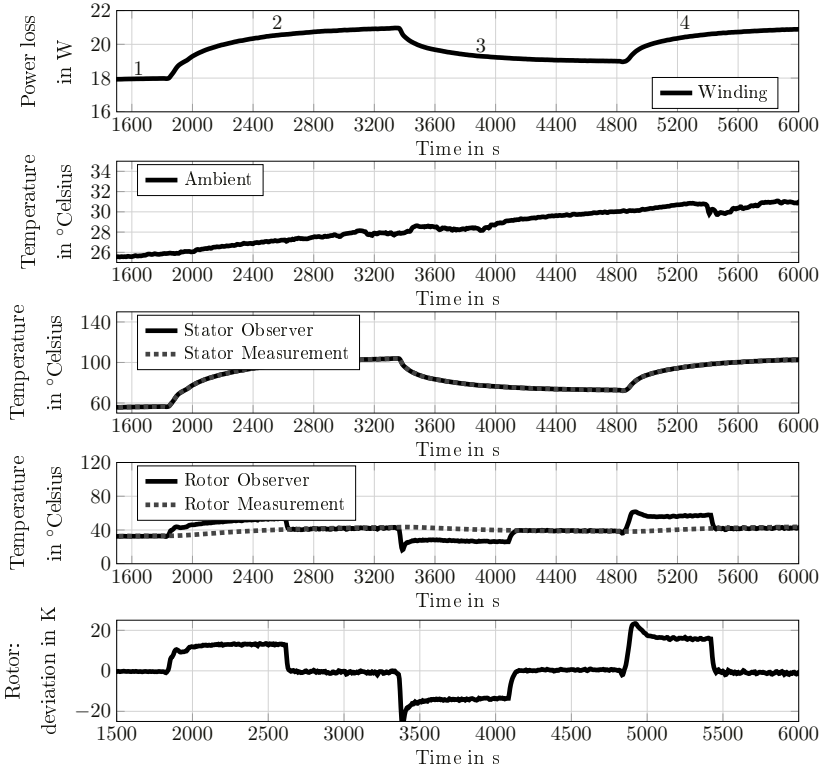
Figure 4.52: Results for adaption of observer parameters after convergence of estimator for different operating points (1: $1300\,\mathrm{min}^{-1}@0.7\,\mathrm{N\,m}$, 2: $1800\,\mathrm{min}^{-1}@1.0\,\mathrm{N\,m}$, 3: $1600\,\mathrm{min}^{-1}@0.8\,\mathrm{N\,m}$, 4: $2000\,\mathrm{min}^{-1}@1.2\,\mathrm{N\,m}$)

4.4.5   Conclusion

This chapter introduced a thermal network, which is based on the continuous estimation of process parameters and the subsequent dynamic tuning of an observer. Settling-in time of the estimator is in the range of some minutes, which is due to the large time-constants inherent to the thermal process and can thus not be increased. Limitations of the used test bench, which cannot be equipped with additional heat sources, prevents speeding up the heating process of the electrical drive.

Once converged, the determined parameter set is suitable for adequately tracking the rotor temperature. For the shown operating point the deviation is smaller than $10\,\mathrm{K}$. It has to be noted, however, that proof for this can only be given for temperature regions observed on the test-bench. These temperatures are far from the rated temperatures of

the stator and rotor. If the presented approach is still suitable for higher temperature regions of the stator and rotor, is a topic for further research.

The presented thermal network poses a valuable contribution to the field of online determination of critical motor temperatures. Together with the DC-injection technique (see Section 4.1), it provides a new approach for determination of the rotor temperature without any application effort. It has to be decided for each application, if the long convergence times are acceptable.
As illustrated in Figure 4.53, the output of the thermal network, i.e. the magnet temperature, has a major role in detecting and diagnosing faults in the electromechanical and the mechanical subsystem. In both systems, it is utilized for adaption of the flux linkage amplitude according to the current magnet temperature.

4.5   Summary

In this chapter, several algorithms were presented suitable for online determination of internal states and parameters. Their significance for the topic of fault detection and diagnosis is illustrated in Figure 4.53.
 A method for determination of the winding resistance was presented, which utilizes an injection technique and a simple two-stage filter. Measurement of the equivalent series resistance is also performed with a short voltage pulse injection. The method presented does not require measurement of the battery current, which makes it cheaper to implement as existing solutions.
Furthermore, a novel algorithm was described for determination of the flux linkage over angle. It can be applied during a power-off scenario both at the EoL with low inertia and in the car with the fan attached. The method is characterized by low computing effort and high accuracy.
The chapter is concluded with a novel approach for determination of the magnet temperature. With utilization of the ambient air temperature and the power loss induced in the windings, the parameters required for the observer structure are constantly updated by an estimator. The presented approach provides good accuracy, however, it suffers from large settling-in times of the estimator. The convergence time cannot be increased though, due to the large thermal time constants inherent to the engine cooling fan motor. However, this is no disadvantage for fault detection during driving.
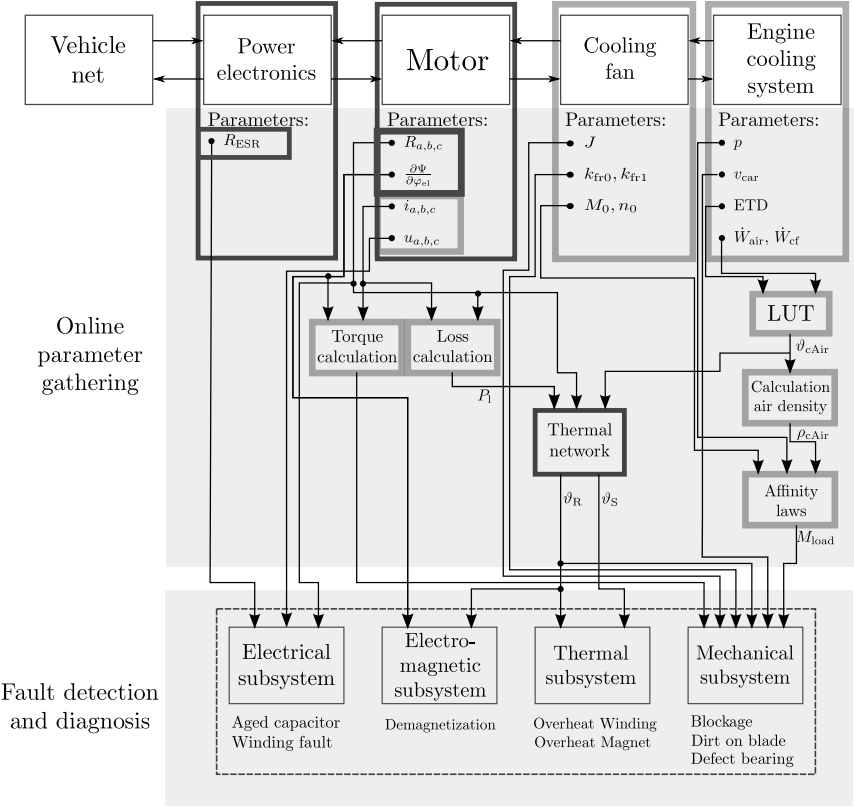
Figure 4.53: Covered topics in chapter four (Marked with a dark bold border, elements marked with a gray bold border were covered in preceding chapters)

5 Fault Detection and Diagnosis: Application

With the introduction of algorithms which provide the possibility to determine important parameters and internal states online, the preceding chapter laid the foundation for the application of fault detection and diagnosis. In the following, the principle of developed algorithms for the detection and diagnosis of selected faults is presented. In the electrical domain, detection of an *aged or damaged capacitor* as well as of *winding faults*, which are caused by resistance changes, was investigated. The electromagnetic subsystem is concerned with the detection of *demagnetization* events. In the thermal domain, the methods for determination of the winding and magnet temperature, as described in Section 4.1 and Section 4.4, are utilized for preventing *overheating* of one of the components. In the mechanical subsystem, detection of *unusual load conditions* are discussed along with *bearing faults*, the detection of a *blockage* and of *dirt on the fan blade*.

The algorithms for fault detection and diagnosis, presented in subsequent sections, rely on EoL-measurements for the determination of parameters in healthy state of the drive. These parameters then serve as a reference for fault detection when the engine cooling fan is operated in the car. In this work, two different EoL-stages of the engine cooling fan are considered.

1. The first stage happens in the plant of the supplier of the electrical motor. At this stage, the ECU is already connected to the electrical motor, but no fan or shroud is assembled. It thus can only be used for determination of parameters concerning the electrical motor, such as winding resistance or flux linkage over rotor position angle.

2. The second stage is in the plant of the car manufacturer with the complete engine cooling fan module (i.e. electrical motor including ECU and fan attached) assembled in the engine compartment of the car. This stage is utilized for the acquisition of process relevant parameters, required for usage of the affinity laws.

In the following, quantities determined in the first stage, i.e. in the plant of the supplier of the electrical motor, are denoted with the subscript *sp* (supplier plant). Parameters acquired in the plant of the car manufacturer are denoted with the subscript *cm* (car manufacturer).

5.1 Electrical Subsystem

In the electrical subsystem, two components were investigated, the winding resistance and the electrolyte capacitor. Values for both are directly measured with the procedures described in Section 4.1 and Section 4.3.

5.1.1 Principle of Operation

For detection of winding resistance faults, an initial value of the winding resistance in healthy state has to be determined. The EoL-stage at the supplier plant of the electrical motor (ECU connected to the electrical motor, but no fan or shroud assembled) is used for that purpose. As described in Section 4.1, an additional voltage is injected onto one motor terminal during standstill of the drive. The winding phase resistance in star configuration is then determined by evaluation of

$$R_{0,\mathrm{sp}}(\tilde{T}_{\mathrm{sp}}) = \frac{2}{3}\frac{U_{\mathrm{um}}}{I_{\mathrm{res,inj}}}\,, \tag{5.1}$$

with U_{um} the motor terminal voltage and $I_{\mathrm{res,inj}}$ the resulting current from the super-imposed voltage. The ambient air temperature $\tilde{T}_{\mathrm{sp}}$ has to be measured externally and supplied by EoL-equipment to the ECU of the electrical motor at this stage. For the measurement it is assumed, that the winding temperature equals the externally supplied ambient air temperature. Please note, that in the following, externally supplied quantities are denoted with a tilde as a superscript and reference quantities with a 0 as subscript.

During operation, detection of winding faults is difficult, as the resistance value strongly depends on the winding temperature. Furthermore, with the method as described in Section 4.1, only a mean resistance value can be determined. However, as the resistance value depends on geometry and material properties, an expected resistance value for a given temperature can be calculated and also supplied to the ECU of the electrical motor. Given this information, a *winding resistance residual* can be derived, comparing the measured with the expected resistance value directly at the EoL of the supplier plant according to

$$r_{\mathrm{el,1,sp}} = R_{0,\mathrm{sp}}(\tilde{T}_{\mathrm{sp}}) - \tilde{R}_{\mathrm{sp}}(\tilde{T}_{\mathrm{sp}})\,. \tag{5.2}$$

In (5.2), $R_{0,\mathrm{sp}}$ denotes the EoL-value of the winding resistance determined with the approach described in Section 4.1, $\tilde{R}_{\mathrm{sp}}(\tilde{T}_{\mathrm{sp}})$ the externally supplied resistance value at the EoL in the supplier plant in healthy state and $\tilde{T}_{\mathrm{sp}}$ the supplied temperature at the EoL.

Fault detection concerning the equivalent series resistance (ESR) is similar to the approach described above. Like for the winding resistance, an initial value of the equivalent series resistance is determined by injection of a short pulse as described in Section 4.3. The ESR-value is then determined by evaluation of

$$R_{\mathrm{ESR,0,sp}} = \frac{\mathrm{d}u_{\mathrm{dc}}}{\mathrm{d}i_{\mathrm{c}}}\,, \tag{5.3}$$

with $\mathrm{d}u_{\mathrm{dc}}$ the voltage across the electrolytic capacitor and $\mathrm{d}i_{\mathrm{c}}$ the capacitor current, both determined at the injection time. Supplying a reference value of the used electrolytic capacitor in healthy state, which can be retrieved from data-sheet parameters or by measurement with an RLC-device, allows for the derivation of a *capacitor resistance* residual directly at the EoL of the supplier plant as

$$r_{\mathrm{el,2,sp}} = R_{\mathrm{ESR,0,sp}} - \tilde{R}_{\mathrm{ESR,sp}} . \tag{5.4}$$

In (5.4), $R_{\mathrm{ESR,0,sp}}$ denotes the EoL-value of the equivalent series resistance and $\tilde{R}_{\mathrm{ESR,sp}}$ the externally supplied resistance value in healthy state.

During operation in the car, a new value for the ESR is determined each time the drive is in standstill (also with the method described in Section 4.3). The newly acquired value is then compared to the reference value $R_{\mathrm{ESR,0,sp}}$, which was determined at the EoL at the supplier plant. A further *capacitor resistance residual* can then be derived as

$$r_{\mathrm{el,3}} = R_{\mathrm{ESR}} - R_{\mathrm{ESR,0,sp}} , \tag{5.5}$$

with R_{ESR} the newly determined value of the equivalent series resistance.

5.1.2 Results

As no motor with a winding fault was available, only simulation results can be given for the detection of a winding fault at the EoL. Both the accuracy of the externally supplied ambient temperature $\tilde{T}_{\mathrm{sp}}$ and the resistance value $\tilde{R}_{\mathrm{sp}}(\tilde{T}_{\mathrm{sp}})$ are assumed to be of high accuracy, leading to a low threshold of $r_{\mathrm{el,1,sp}}$ for the detection of a winding fault. Results for differently aged capacitors are depicted in Table 5.1. As can be seen, the ESR determination performed with the ECU-implementation shows good congruence with the reference measurement performed with an RLC-device.

However, as can be seen in Figure 4.26, the value of the equivalent series resistance decreases with rising temperature. To distinguish between a decrease caused by temperature and an increase caused by an aging capacitor (see Figure 4.35), a temperature information therefore has to be included.

Considering (4.41), however, which states, that a capacitor has reached the end of its lifetime when the equivalent series resistance is three times as high as the initial value, a strongly aged capacitor can also be diagnosed without any temperature information due to the strong change in resistance value. The resulting fault-symptom table for the electrical subsystem is listed in Table 5.2.

5.2 Electromagnetic Subsystem

The literature describes various methods to detect a demagnetization. Rosero et al. (2006), Ruschetti et al. (2010) and Rosero et al. (2007) perform an FFT or a Wavelet transformation on the stator current and the zero sequence current. Their findings suggest, that the

Table 5.1: Equivalent series resistance (ESR) measurements with RLC-meter and with implemeted algorithm on ECU (see Section 4.3) for differently aged capacitor

	RLC-meter	ECU	Absolute deviation	Relative error
New capacitor	$0.0236\,\Omega$	$0.0232\,\Omega$	$0.4\,\mathrm{m}\Omega$	$1.69\,\%$
Medium aged capacitor	$0.0296\,\Omega$	$0.0286\,\Omega$	$1.0\,\mathrm{m}\Omega$	$3.37\,\%$
Strongly aged capacitor	$0.0620\,\Omega$	$0.0555\,\Omega$	$6.5\,\mathrm{m}\Omega$	$10.84\,\%$

Table 5.2: Fault-symptom table for the electrical subsystem (0 no significant change; $+$ increase; $++$ large increase; $-$ decrease; $--$ large decrease)

Fault	$r_{\mathrm{el,1,sp}}$	$r_{\mathrm{el,2,sp}}$	$r_{\mathrm{el,3}}$
Winding fault	$+/-$	0	0
Aged / damaged capacitor	0	$+/++$	$++$

derived symptoms vary depending on the winding configuration as well as the operating point. Casadei et al. (2009) and Khoobroo and Fahimi (2010) both perform the FFT on the shape of the induction voltage waveform. As the form of the induction voltage can only be measured or simulated under a no-load condition, this method is not operating condition dependent. However, it shows, that the winding configuration has to be taken into account as well for determination of suitable symptoms.

5.2.1 Principle of Operation

The approach presented here is based on the reconstruction of the flux linkage as described in Section 4.2. To investigate the potential of the reconstruction for diagnosing a demagnetization event, several motors were subjected to demagnetization currents between 60 A and 140 A.

The decrease of the rms-value of the flux linkage over the demagnetization current for the given motor with ferrite-magnets is shown in Figure 5.1.   Amplitudes of relevant harmonics (the occurence of sub-harmonics was not further investigated in this work) of the induction voltage during power-off compared to the healthy state are displayed in Figure 5.2. A decrease of the amplitude can be observed, but with a different slope for each harmonic. A counter-effect to this trend, however, is shown in Figure 5.3. For ferrite magnets, the harmonics also decrease with rising temperature. Neglecting temperature effects can thus result in wrongly diagnosing a healthy system with a demagnetization.
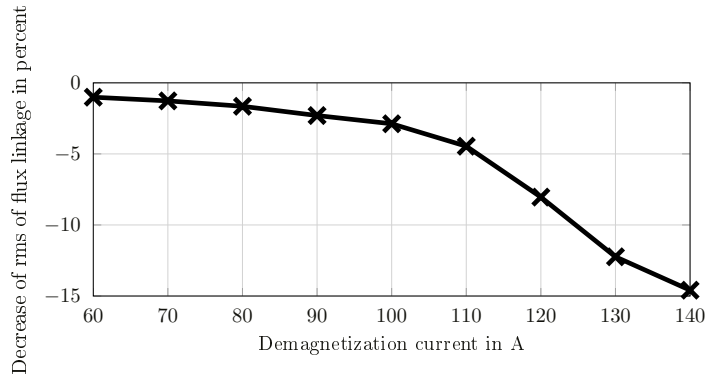
Figure 5.1: Decrease of rms-value of flux linkage over demagnetization current
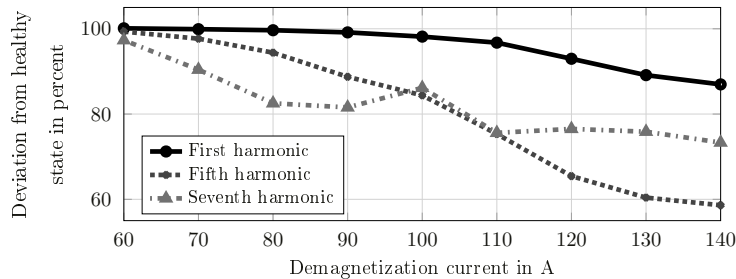

Figure 5.2: Amplitude of different harmonics of induction voltage during power-off at room temperature over demagnetization current

When looking at the second harmonic, however, a temperature-independent symptom can be derived as illustrated in Figure 5.4. The second harmonic shows a steep increase when a demagnetization occurred with currents above 110 A.

Based on the observed effects, several residuals can be derived for diagnosing a demagnetization by comparison of the amplitudes of the harmonics. As pointed out in Section 4.2, due to the different frequency responses of the low-pass filters used for measurement of the line-to-line voltage, the phase angles showed a large deviation between the individual phases, rendering them unsuitable for utilization in fault diagnosis.

The initial values for the individual harmonics are measured with an EoL-test at the supplier plant with the procedure described in Section 4.2. At this stage, only the ECU is connected to the electrical motor, which corresponds to scenario one as described in Section 4.2. In case that values for the healthy state are supplied externally, a first evaluation
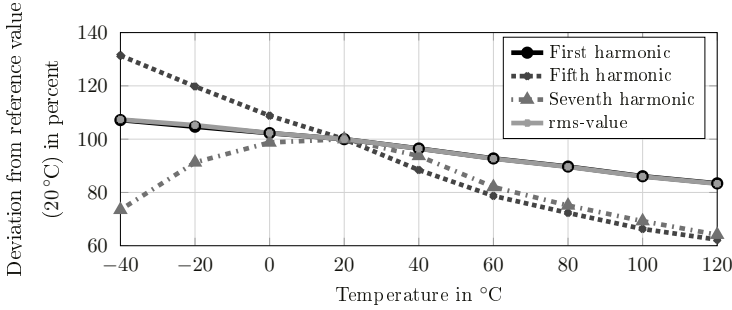
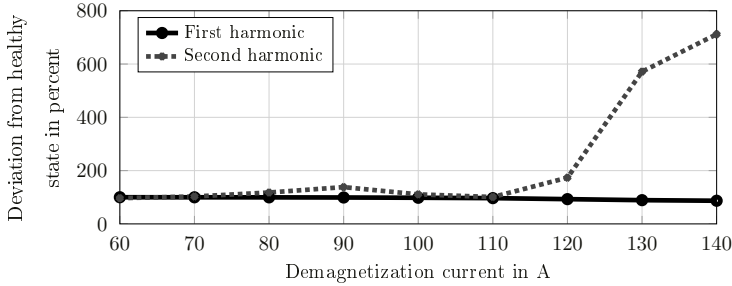Figure 5.3: Amplitude of harmonics over temperature of a healthy motor

Figure 5.4: Amplitude of second harmonic of the flux linkage at room temperature over demagnetization current

of *demagnetization residuals* can take place directly at the EoL:

$$r_{\mathrm{em},i,\mathrm{sp}} = a_{0,i,\mathrm{sp}}(\tilde{T}_{\mathrm{sp}}) - \tilde{a}_{i,\mathrm{sp}} \,, \tag{5.6}$$

with $a_{0,i,\mathrm{sp}}$ the determined amplitude of the i-th harmonic at the EoL of the supplier plant, $\tilde{a}_{i,\mathrm{sp}}$ the externally supplied value for the amplitude of the i-th harmonic in healthy state and $\tilde{T}_{\mathrm{sp}}$ the externally supplied ambient air temperature.

During operation in the car, a new set of amplitudes can be acquired during a power-off procedure. As the fan and hub are attached to the electrical motor, this corresponds to scenario 2 as depicted in Section 4.2. The newly determined parameter set yields a new set of *demagnetization residuals* as

$$r_{\mathrm{em},i} = a_{0,i,\mathrm{sp}}(\tilde{T}_{\mathrm{sp}}) - \frac{a_i}{1 - \gamma_{\mathrm{a},i} \cdot \left(T_{\mathrm{mag}} - \tilde{T}_{\mathrm{sp}}\right)} \,, \tag{5.7}$$

with a_i the amplitude of the i-th harmonic determined during the power-off procedure, $\gamma_{\mathrm{a},i}$ the temperature coefficient of the i-th harmonic and T_{mag} the current magnet temperature (derived with the thermal network as described in Section 4.4).

5.2.2 Results

As can be seen in Figure 5.3, each harmonic has a different temperature coefficient. This is due to saturation effects in the magnetic circuit. Determination of the different coefficients requires measurements in the temperature chamber. To reduce complexity and application effort, the temperature coefficients are set to the value which is supplied with the data-sheet of the used magnet:

$$\gamma_{\mathrm{a},i} = \gamma_{\mathrm{br}}\,. \tag{5.8}$$

As a consequence, the thresholds for diagnosis have to be increased slightly.

In healthy state, the second harmonic is not present in the spectrum of the flux linkage. As illustrated in Figure 5.4, it can be measured when demagnetizing with currents above 110 A, which results in a decrease of the rms-value of approximately 8 % (see Figure 5.1). In case a second harmonic is detected, this is thus a clear and temperature-independent indicator for a demagnetization. When taking other harmonics into account, the temperature has to be considered as well. The fault-symptom table, exemplary for the first, the second, the third and the seventh harmonic, is displayed in Table 5.3.

Table 5.3: Fault-symptom table for electromagnetic subsystem both at EoL of the supplier plant and during operation in the car (0 no significant change; + increase; ++ large increase; − decrease; −− large decrease)

Fault	$r_{\mathrm{em},1\{,\mathrm{sp}\}}$	$r_{\mathrm{em},2\{,\mathrm{sp}\}}$	$r_{\mathrm{em},3\{,\mathrm{sp}\}}$	$r_{\mathrm{em},7\{,\mathrm{sp}\}}$
Strong demagnetization	++	+	++	++
Medium or low demagnetization	+	0	+	+

5.3 Thermal Subsystem

An overheating of the winding and the magnets was investigated in this work. As pointed out in Section 3.2, no external heat source could be assembled on the test bench. Reaching the required temperatures for an overheating of the winding or the magnet on the test-bench was therefore not possible. Evaluation was thus carried out by simulation.

Fault detection for winding and magnet overheating is perfomed, while the engine cooling fan is being operated in the car. Overheating of one of the components is detected by a simple limit checking, requiring the current temperature of the winding and the magnets and maximum rated temperatures of both components.
Based on the measured winding resistance (see Section 4.1), the winding temperature is

retrieved by solving (4.1) for T_{winding}, yielding

$$T_{\text{winding}} = \frac{1}{\gamma} \left(\frac{R_{\text{winding}}}{R_{\text{winding,0}}(T_{\text{winding,0}})} - 1 \right) + T_{\text{winding,0}} \,. \tag{5.9}$$

In (5.9), γ is the temperature coefficient of the winding material (for copper it holds $\gamma = 0.39\,\%\,\text{K}^{-1}$), $R_{\text{winding,0}}(T_{\text{winding,0}})$ the reference resistance at a given temperature, $T_{\text{winding,0}}$ and R_{winding} the currently measured winding resistance. For the reference resistance, the value retrieved at the EoL of the supplier of the electrical motor (see Section 5.1) is used. The current winding temperature is thus determined by evaluation of

$$T_{\text{winding}} = \frac{1}{\gamma} \left(\frac{R_{\text{winding}}}{R_{0,\text{sp}}(\tilde{T}_{\text{sp}})} - 1 \right) + \tilde{T}_{\text{sp}} \,. \tag{5.10}$$

The winding temperature and resistance both serve as an input to the termal network described in Section 4.4. Output of the network is the current magnet temperature T_{mag}. The rated maximum temperatures of the windings and the magnets can either be supplied externally at an EoL-stage or hardcoded into the ECU-firmware. Here it is assumed, that the corresponding values are transferred to the ECU at the EoL of the supplier of the electrical motor.

Winding and magnet overheating residuals can thus be derived as

$$r_{\text{th,1}} = \tilde{T}_{\text{winding,max,sp}} - T_{\text{winding}} \tag{5.11}$$

$$r_{\text{th,2}} = \tilde{T}_{\text{mag,max,sp}} - T_{\text{mag}} \,, \tag{5.12}$$

with $\tilde{T}_{\text{winding,max,sp}}$ the externally supplied maximum temperature of the winding, T_{winding} the current winding temperature determined with the method described in Section 4.1, $\tilde{T}_{\text{mag,max,sp}}$ the externally supplied maximum temperature of the magnet and T_{mag} the current magnet temperature (output of the thermal network described in Section 4.4).

It has to be noted, that the magnet temperature can not be determined as accurate as the winding temperature due to the limitations set forth by the thermal network. The threshold at which a reaction takes place should therefore be chosen much lower than the threshold for the detection of an overtemperature of the winding. The resulting fault-symptom table is shown in Table 5.4.

Table 5.4: Fault-symptom table for the thermal subsystem (0 no significant change; $+$ increase; $++$ large increase; $-$ decrease; $--$ large decrease)

Fault	$r_{\text{th,1}}$	$r_{\text{th,2}}$
Overheat Winding	$-$	$-$
Overheat Magnet	$-$	$-$

5.4   Mechanical Subsystem

Main topic in this work concerning the mechanical subsystem is the identification of *unusual load conditions*. These conditions can be caused by a *blockage* of the fan module by an object (e.g. leaves or whole branches), or by a *stiff bearing* leading to higher friction. Both events shift the operating point to one with a higher torque, resulting in larger currents flowing through the machine. This in turn can lead to a demagnetization event, overheating or in the worst case, to a burning down of the whole device. This is serious, as the thermal event can pass over to the whole vehicle.

The algorithm for identification of *unusual load conditions* currently implemented on the series ECU of the engine cooling fan has several limitations, the most severe among them being:

- High calibration effort in terms of expensive test bench measurements during design phase for parametrization of the algorithm for each different motor/fan combination.

- High error margin due to the lack of information about the system, such as magnet temperature and phase currents.

- No possibility for adaption to changes in machine characteristics due to aging or malfunction.

5.4.1   Principle of Procedure

Aim of the algorithm developed is to overcome the above mentioned shortcomings, with a focus on minimizing application effort and the ability for adaption to machine tolerances and changing motor parameters. The first is accomplished with EoL measurements both in the supplier plant and the production line of the car manufacturer. The adaption to machine characteristics is achieved with an online thermal network (see Section 4.4) and the methods for gathering machine parameters covered in Chapter 4. A simplified topology of the algorithm is depicted in Figure 5.5. Main principle is to determine an expected torque and compare that value with the actually delivered torque of the drive. A value other than zero suggests a possible unusual load condition. For calculation of the currently delivered and the expected torque several drive-specific parameters are required. Some of them, like the actual stator phase current or the actual rotor position angle, are determined during runtime, others, like the flux linkage or process-specific parameters, have to be acquired with an EoL procedure. To achieve a higher degree of robustness more than one residual is evaluated.

The presented structure is twofold. Foundation of the algorithm is the acquisition of a base parameter set with the drive being in a healthy state. This is done with an EoL run of the motor. The actual fault detection and diagnosis during operation of the drive in
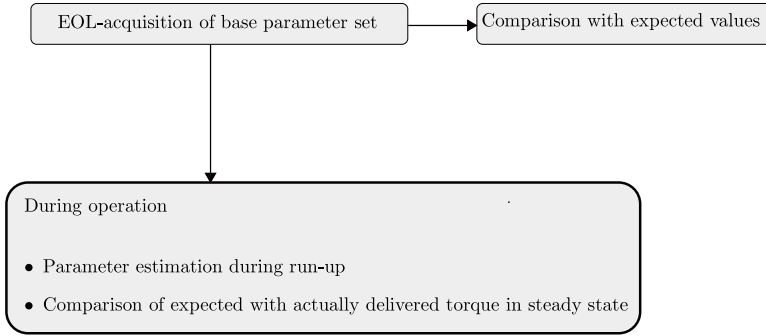
Figure 5.5: Basic topology of the algorithm for detection of unusual load conditions

the car is done by calculation and evaluation of several residuals, which will be derived and explained in the following.

Base Parameter Set

The algorithm requires several parameters, all of which are acquired with an EoL-run of the machine. Parameters specific to the electrical machine like the winding resistance or the flux linkage over angle are determined at the EoL of the supplier of the elctrical machine.

Determination of the process-specific parameters demands a run-up procedure of the electrical drive under known ambient conditions while being installed in the vehicle, as these parameters are strongly dependent on the air perfusion through the engine compartment. As a consequence, this test-run has to take place in the plant of the car manufacturer. Both EoL-tests and the resulting parameters are outlined in Figure 5.6 and Table 5.5, respectively. Please note that externally delivered variables are marked with a tilde and acquired reference values are indicated with the subscript 0.
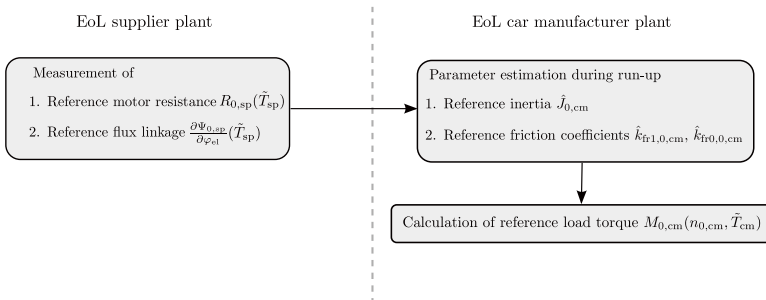

Figure 5.6: Diagram depicting required steps for determination of the base parameter set

Table 5.5: Overview of base parameter set determination

EoL supplier of electrical drive			
Method	Supplied externally	Determined parameter	Corresponding residual
Winding resistance determination (Section 4.1)	$\tilde{R}_\text{sp},\tilde{T}_\text{sp}$	$R_{0,\text{sp}}(\tilde{T}_\text{sp})$	$r_{\text{el},1,\text{sp}}$
Flux linkage over angle determination (Section 4.2)	$\tilde{a}_{i,\text{sp}},\tilde{T}_\text{sp}$	$\frac{\partial \Psi_{0,\text{sp}}}{\partial \varphi_\text{el}}(\tilde{T}_\text{sp})$	$r_{\text{em},i,\text{sp}}$
-	$\tilde{k}_{\text{fr0},\text{sp}}, \tilde{k}_{\text{fr1},\text{sp}}(\tilde{T}_\text{sp})$		-

EoL car manufacturer			
Method	Supplied externally	Determined parameter	Corresponding residual
Parameter estimation (Section 2.1.3)	$\tilde{J}_\text{cm}$	$\hat{J}_{0,\text{cm}}$	$r_{\text{mech},1,\text{cm}}$
Parameter estimation (Section 2.1.3)		$\hat{k}_{\text{fr0},0,\text{cm}}$	$r_{\text{mech},3}$
Parameter estimation (Section 2.1.3)		$\hat{k}_{\text{fr1},0,\text{cm}}$	$r_{\text{mech},4}$
Calculation ((5.26))	$\tilde{T}_\text{cm}$	$M_{0,\text{cm}}(n_{0,\text{cm}},\tilde{T}_\text{cm})$	$r_{\text{mech},5}$

For the proposed method, parameters specific to the electrical machine, i.e. the winding resistance $R_{0,\text{sp}}(\tilde{T}_\text{sp})$ and the flux linkage over angle $\frac{\partial \Psi_{0,\text{sp}}}{\partial \varphi_\text{el}}(\tilde{T}_\text{sp})$, are determined at the supplier plant of the electrical machine and stored in the microcontroller.

The motor resistance is required for determination of the winding temperature during operation of the drive, whereas the flux linkage is utilized for torque calculation according to (3.19). Determination of both parameters at the EoL of the supplier plant was already described in Section 5.1 and Section 5.2, respectively. After determination of the values, a first fault detection can take place by comparing to externally delivered reference value in healthy state, leading to the *winding resistance residual* (5.2)

$$r_{\text{el},1,\text{sp}} = R_{0,\text{sp}}(\tilde{T}_\text{sp}) - \tilde{R}_\text{sp}(\tilde{T}_\text{sp})\,, \tag{5.13}$$

and the *demagnetization residuals* (5.6)

$$r_{\text{em},i,\text{sp}} = a_{0,i,\text{sp}}(\tilde{T}_\text{sp}) - \tilde{a}_{i,\text{sp}}\,. \tag{5.14}$$

The flux linkage over angle $\frac{\partial \Psi_{0,\text{sp}}}{\partial \varphi_\text{el}}$ can easily be determined from the retrieved amplitudes

and phase angles of the relevant harmonics. The right part of Figure 5.6 depicts the procedure for determination of parameters when the drive is completely assembled in the car including fan and shroud, i.e. it represents the EoL stage at the plant of the car manufacturer. The reference inertia $\hat{J}_{0,\text{cm}}$ and the friction coefficients $\hat{k}_{\text{fr}0,0,\text{cm}}$ and $\hat{k}_{\text{fr}1,0,\text{cm}}$ are determined by parameter estimation during a run-up procedure with

$$M_{\text{mot}} = \hat{J}_{0,\text{cm}}\dot{\omega}_{\text{rot}} + \hat{k}_{\text{fan,cm}}\omega_{\text{rot}}^2 + \hat{k}_{\text{fr}1,0,\text{cm}}\omega_{\text{rot}} + \hat{k}_{\text{fr}0,0,\text{cm}} \,. \tag{5.15}$$

M_{mot} is the torque produced by the electrical machine and calculated according to (3.19), $\hat{J}_{0,\text{cm}}$ the inertia of the motor and the fan, and $\hat{k}_{\text{fan,cm}}$ the fan constant.

In Table 5.5 it can be seen, that two reference friction coefficients in healthy state, $\tilde{k}_{\text{fr}0,\text{sp}}$ and $\tilde{k}_{\text{fr}1,\text{sp}}$, are already supplied to the ECU during the EoL stage in the plant of the supplier of the electrical drive. This is because estimation of the friction coefficients with (5.15) gives implausible results, as the estimator seems to be distorted by the additional entries in the measurement matrix. For calculation of the friction torque with

$$M_{\text{fr}} = \omega_{\text{rot}}\tilde{k}_{\text{fr}1,\text{sp}}\left(\frac{T_{\text{mag}}}{\tilde{T}_{\text{sp}}}\right) + \tilde{k}_{\text{fr}0,\text{sp}} \,, \tag{5.16}$$

however, correct values of the friction coefficients are required. As will be shown later, storage of the wrongly estimated friction coefficients is not unnecessary. Re-estimating the coefficients with a defect bearing showed significant deviations of the estimated values for the friction coefficients, which makes them suitable for diagnosing a bearing fault.

Estimation of the inertia with (5.15) gave results which were expected based on geometric data. Comparing the estimated value at the EoL with the externally delivered inertia in healthy state $\tilde{J}_{\text{cm}}$ yields the *inertia residual*

$$r_{\text{mech},1,\text{cm}} = \tilde{J}_{\text{cm}} - \hat{J}_{0,\text{cm}} \,. \tag{5.17}$$

Similar to the EoL measurement at the supplier plant, the current air temperature $\tilde{T}_{\text{cm}}$ has to be measured and transferred to the ECU. The estimated values are stored as a reference in the microcontroller and can be compared to newly estimated ones after each run-up procedure when the drive is operated in the car.

Main principle of the algorithm is to calculate an expected torque for the given operating point and compare that value with currently delivered torque by the electrical drive. Calculation of the expected torque is performed by utilization of the affinity law

$$M_{\text{expected}} = \left(\frac{\tilde{\rho}}{\tilde{\rho}_{0,\text{cm}}}\right) \cdot \left(\frac{n}{n_{0,\text{cm}}}\right)^2 M_{0,\text{cm}} \,, \tag{5.18}$$

with M_{expected} the expected torque for the operation point given by the air density $\tilde{\rho}$ and the rotational speed n. In (5.18), $\tilde{\rho}_{0,\text{cm}}$, $M_{0,\text{cm}}$ and $n_{0,\text{cm}}$ are reference values which have to be determined at the EoL of the car manufacturer. For determination, the engine cooling fan has to be held at a steady state operating point for a short time. The reference parameters can then be retrieved with

$$M_{0,\text{cm}}(n_0, \tilde{T}_{\text{cm}}) = M_{\text{mot}} - \tilde{k}_{\text{fr}1,\text{sp}} \cdot \left(\frac{\tilde{T}_{\text{cm}}}{\tilde{T}_{0,\text{sp}}}\right)\omega_{\text{rot}} - \tilde{k}_{\text{fr}0,\text{sp}} \,, \tag{5.19}$$

with n_0 the current rotational speed, $\tilde{T}_{cm}$ the externally supplied ambient air temperature, M_{mot} the torque delivered by the electrical machine according to (3.19), and $\tilde{k}_{fr,0,sp}$ and $\tilde{k}_{fr,1,sp}$ the externally supplied friction coefficients at the EoL of the supplier of the electrical drive. The friction coefficients estimated with (5.15) can not be used here as they, due to their wrong value, would distort the determination of the reference torque $M_{0,cm}$. For later usage of (5.18) it is also required to externally supply the ECU with a value for the current air density $\tilde{\rho}_{0,cm}$, which can be delivered by the ECU of the combustion engine.

Fault Detection and Diagnosis

Three stages for fault detection and diagnosis can be identified for the mechanical subsystem. The first one is at the EoL of the supplier of the electrical machine, the second stage is at the EoL of the car manufacturer and the third one is while the drive is being operated in the car.

The fault detection possibilities in the first and second stage, i.e. at the EoL, consist of comparison of determined parameters with externally supplied values in healthy state. At the EoL of the supplier of the electrical drive, winding and demagnetization faults can be detected with the *winding residual* and the *demagnetization residual*

$$r_{el,1,sp} = R_{0,sp}(\tilde{T}_{sp}) - \tilde{R}_{sp}(\tilde{T}_{sp}) \tag{5.20}$$

$$r_{em,i,sp} = a_{0,i,sp}(\tilde{T}_{sp}) - \tilde{a}_{i,sp} . \tag{5.21}$$

At the EoL of the car manufacturer, one residual can be evaluated. With the *inertia residual* it is possible to detect problems connected with the fan blade, such as dirt sticking to it:

$$r_{mech,1,cm} = \tilde{J}_{cm} - \hat{J}_{0,cm} . \tag{5.22}$$

While the drive is being operated in the car, a new set of residuals can be built. During each run-up procedure, a new parameter estimation according to (5.15) is performed, yielding a new set of values for the inertia $\hat{J}$ and the friction coefficients $\hat{k}_{fr,0}$ and $\hat{k}_{fr,1}$. With the new estimation, another *inertia residual* can be built as

$$r_{mech,2} = \hat{J} - \hat{J}_{0,cm} , \tag{5.23}$$

with $\hat{J}$ the newly estimated inertia and $\hat{J}_{0,cm}$ the inertia estimated during a run-up procedure at the EoL of the car manufacturer. The estimated friction coefficients can also be compared, leading to the *friction residuals*

$$r_{mech,3} = \hat{k}_{fr1} - \hat{k}_{fr1,0,cm} \tag{5.24}$$

$$r_{mech,4} = \hat{k}_{fr0} - \hat{k}_{fr0,0,cm} , \tag{5.25}$$

with $\hat{k}_{fr1}$ and $\hat{k}_{fr0}$ the newly estimated friction coefficients, and $\hat{k}_{fr0,0,cm}$ and $\hat{k}_{fr1,0,cm}$ the friction coefficients estimated during a run-up procedure at the EoL of the car manufacturer.

When the drive is operated in steady state, a *torque residual* can be evaluated as

$$r_{mech,5} = M_{mot} - (M_{\text{Af}} + M_{\text{fr}}) \;, \tag{5.26}$$

with M_{mot} the currently delivered torque according to (3.19), the term M_{Af} representing the currently expected torque and M_{fr} the friction torque. The currently expected torque can be calculated with

$$M_{\text{Af}} = \left(\frac{\tilde{\rho}}{\tilde{\rho}_{0,\text{cm}}} \right) \cdot \left(\frac{n}{n_{0,\text{cm}}} \right)^2 M_{0,\text{cm}} \;, \tag{5.27}$$

with $\tilde{\rho}$ the air density of the current operating point, taking into account the air pressure and temperature behind the cooler. See (3.46) to (3.49) for the corresponding equations. The air density can be supplied to the ECU of the engine cooling fan by the ECU of the combustion engine.

The resistance torque generated by friction and iron losses is calculated as

$$M_{\text{fr}} = \omega_{\text{rot}} \tilde{k}_{\text{fr1,sp}} \left(\frac{T_{\text{mag}}}{\tilde{T}_{\text{sp}}} \right) + \tilde{k}_{\text{fr0,sp}} \;. \tag{5.28}$$

5.4.2 Results

The faults, that can be detected and isolated with the above residuals, are listed in Table 5.6. For evaluation of the residuals, all faults were reproduced on the test bench. As the estimation of the friction coefficients is attached with a high degree of uncertainty, only one bearing defect was prepared (leaking lubrication) to investigate, whether the estimates can be used for diagnosis despite their wrong values. As can be seen in Table 5.6, the corresponding residuals show a clear pattern when the motor is operated with the defect bearing.

The fault *dirt on the fan blade* was simulated by using different sized clutches, which increase or decrease the overall inertia of the system. As expected, $r_{\text{mech,1,cm}}$ is a clear indicator for a changed inertia. Blockage, caused e.g. by leaves or whole branches stuck in the engine compartment, was reproduced by an additional constant load during operation, which leads to a load higher than expected.

An exemplary development of the parameter estimate of the inertia is shown in Figure 5.7, development of the residual $r_{\text{mech,5}}$ for different car velocities is illustrated in Figure 5.8. As can be seen, the car velocity distorts $r_{\text{mech,5}}$ as shown in Figure 5.8. The airstream caused by the moving car decreases the load of the fan drive, which is not covered by (5.27). Consequently, a moving car with no blockage leads to a negative value of $r_{\text{mech,5}}$, whereas a moving car with a simulated blockage is not detected, as $r_{\text{mech,5}}$ stays around zero. The car velocity for the example shown in Figure 5.8 was $10\,\text{km}\,\text{h}^{-1}$. Adjustment of (5.27) to account for the car velocity is possible, but, due to the nonlinearities inherent,

Table 5.6: Fault-symptom table for mechanical subsystem (0 no significant change; + increase; ++ large increase; − decrease; −− large decrease)

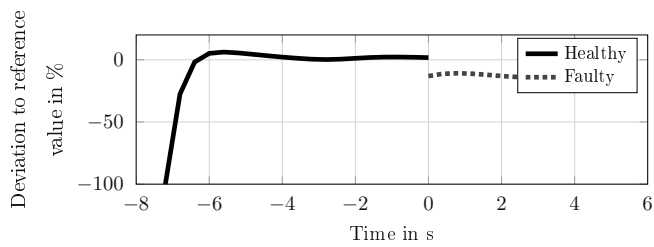| Fault	Residual						
	$r_{\text{el},1,\text{sp}}$	$r_{\text{em},i,\text{sp}}$	$r_{\text{mech},1,\text{cm}}$	$r_{\text{mech},2}$	$r_{\text{mech},3}$	$r_{\text{mech},4}$	$r_{\text{mech},5}$
Winding fault	$+/-$	0	0	0	0	0	0
Demagnetization	0	$++/0$	0	0	0	0	0
Defect bearing	0	0	0	0	$++$	$+$	0
Dirt on fan blade	0	0	$+$	$+$	0	0	0
Blockage	0	0	0	0	0	0	$++$

Figure 5.7: Development of parameter estimates for $\hat{J}\left(r_{\text{mech},2}\right)$. The error *dirt on fan blade* is introduced at time $t = 0\,\text{s}$.

demands a high computing effort. As the engine cooling fan is mainly operated when the car is not moving, this does not constitute a severe limitation.

The presented algorithm is able to overcome the limitations of current implementations indicated above. The implementation complexity, however, is very high, as a large number of parameters have to be acquired and be handled with. Despite the implementation issue, the presented approach shows a large potential in terms of decreasing application costs, as all relevant information is gathered with an EoL run. Unfortunately, the friction coefficients could not reliably be estimated, which requires to supply them externally. It was shown however, that despite their wrong values, the coefficients estimated with (5.15) can be used for diagnosing a defect bearing. Their utilization in a series product, however, is highly questionable due to the unreliability and the not fully understood side-effects on the estimation of the inertia and the fan constant.

5.5   Required Cycle Time at EoL

Assuming, that all described methods for fault detection and diagnosis are to be applied in a series product, several parameters have to be acquired at both the EoL of the supplier
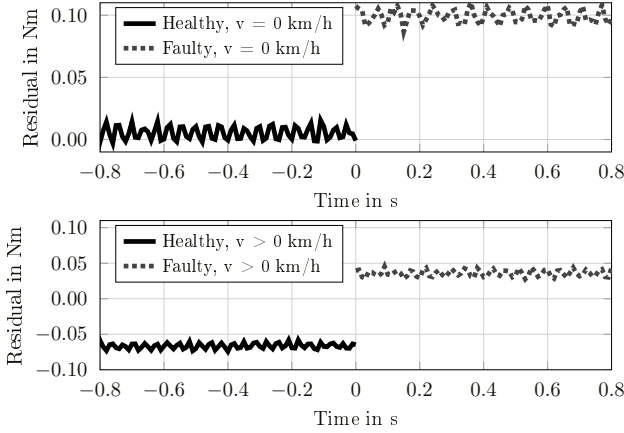
Figure 5.8: Development of calculated residual $r_{\mathrm{mech},5}$ according to Table 5.6 for unusual load detection. The error *blockage* is introduced at time $t = 0\,\mathrm{s}$.

of the electrical machine and the car manufacturer. Approximate times for the detection of the required parameters are given in Figure 5.9. At the EoL of the supplier of the electrical machine reference values for the winding resistance $R_{0,\mathrm{sp}}$, the resistance of the DC-link capacitor $R_{\mathrm{ESR},0,\mathrm{sp}}$ and the flux linkage over angle $\frac{\partial \Psi_{0,\mathrm{sp}}}{\partial \varphi_{\mathrm{el}}}$ have to be acquired.

Both the winding resistance and the equivalent series resistance can be determined with the electrical motor being in standstill. Determination of the reference winding resistance demands superposition of an injection voltage on one of the three phases. This superimposed DC-voltage leads to a short rotor movement, which has to be waited for to decline before the actual measurement can take place, resulting in an approximate time for the determination of the reference winding resistance of 200 ms.

The equivalent series resistance of the DC-link capacitor can be retrieved by injection of a short voltage pulse. As the rotor movement does not interfere with the measurement, $R_{\mathrm{ESR},0,\mathrm{sp}}$ can be determined in approximately 5 ms.

The flux linkage over angle can only be acquired during a power-off procedure of the drive. This requires a power-up of the electrical drive to an arbitrary rotational speed. The following power-off procedure can be supported by active braking performed by the EoL equipment, leading to a determination time of 30 ms.

At the plant of the car manufacturer reference values for the inertia $\hat{J}_{0,\mathrm{cm}}$ and the friction coefficients $\hat{k}_{\mathrm{fr},0,\mathrm{cm}}$ and $\hat{k}_{\mathrm{fr},1,\mathrm{cm}}$ have to be acquired. Furthermore, a reference torque has to be determined for later usage with the affinity laws. The inertia and friction coefficients are determined with parameter estimation during a run-up of the drive. As the drive is fully equipped, i.e. fan and shroud attached, the run-up procedure takes (depending on the final operating point) around 9 s. Once the run-up procedure is completed, acquisi-
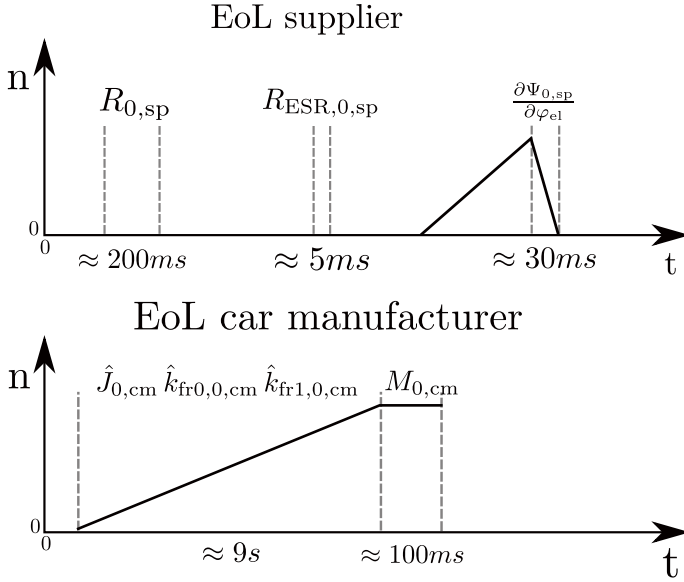
Figure 5.9: Required cycle times for detection of parameters at the EoL

tion of the reference torque requires the drive to be held in steady state for approximately 100 ms.

5.6 Conclusion

In this chapter it was demonstrated, that knowledge of internal states and parameters enables the application of a detailed fault detection and diagnosis, which is simple to implement and does not require extensive computational resources. Furthermore, connections between the single residuals were kept at a minimum, allowing for implementation of the described methods to different applications without requiring additional application effort. Since there is no interconnection between the individual residuals, all faults can be diagnosed unambiguously.

In most cases, the detailed knowledge of the parameters enables a procedure for fault detection and diagnosis by a comparison with a predefined threshold. Only the mechanical subsystem requires evaluation of several residuals to increase the overall robustness of the algorithm.

A summary of all fault-symptom tables developed in Section 5 is given in Table 5.7 and a complete overview of the required parameters for detection and diagnosis of the selected faults is given in Table 5.8.

Table 5.7: Summarized fault-symptom table for investigated faults (0 no significant change; + increase; ++ large increase; − decrease; −− large decrease)

Electrical subsystem			
	$r_{\mathrm{el,1,sp}}$	$r_{\mathrm{el,2,sp}}$	$r_{\mathrm{el,3}}$
Winding fault	+/−	0	0
Aged / damaged capacitor	0	+/++	++

Electromagnetic subsystem				
	$r_{\mathrm{em,1}}$	$r_{\mathrm{em,2}}$	$r_{\mathrm{em,3}}$	$r_{\mathrm{em,7}}$
Strong demagnetization	++	++	++	++
Medium or low demagnetization	+	0	+	+

Thermal subsystem	
	$r_{\mathrm{th,1}}$	$r_{\mathrm{th,2}}$
Overheat Winding	−	−
Overheat Magnet	−	−

Mechanical subsystem					
	$r_{\mathrm{mech,1,cm}}$	$r_{\mathrm{mech,2}}$	$r_{\mathrm{mech,3}}$	$r_{\mathrm{mech,4}}$	$r_{\mathrm{mech,5}}$
Defect bearing	0	0	++	+	0
Dirt on fan blade	+	+	0	0	0
Blockage	0	0	0	0	++

Table 5.8: Investigated faults in this work broken down to the different stages. Also given are required parameters for their detection and diagnosis along with a reference to the used method for parameter acquisition.

Fault	Method	Supplied externally	Determined parameter	Corresponding residual
EoL supplier of electrical drive				
Winding fault	Winding resistance determination (Section 4.1)	$\tilde{R}_{\mathrm{sp}},\tilde{T}_{\mathrm{sp}}$	$R_{0,\mathrm{sp}}(\tilde{T}_{\mathrm{sp}})$	$r_{\mathrm{el},1,\mathrm{sp}}$
Demagnetization	Flux linkage over angle determination (Section 4.2)	$\tilde{a}_{i,\mathrm{sp}},\tilde{T}_{\mathrm{sp}}$	$a_{0,i,\mathrm{sp}}$	$r_{\mathrm{em},i,\mathrm{sp}}$
Aged / damaged DC-link capacitor	ESR determination (Section 4.3)	$\tilde{R}_{\mathrm{ESR,sp}}$	$R_{\mathrm{ESR},0,\mathrm{sp}}$	$r_{\mathrm{el},2,\mathrm{sp}}$
EoL car manufacturer				
Dirt on fan blade	Parameter estimation (Section 2.1.3)	$\tilde{J}_{\mathrm{cm}}$	$\hat{J}_{0,\mathrm{cm}}$	$r_{\mathrm{mech},1,\mathrm{cm}}$
Operation in the car				
Demagnetization	Flux linkage over angle determination (Section 4.2)	-	a_i	$r_{\mathrm{em},i}$
Aged / damaged DC-link capacitor	ESR determination (Section 4.3)	-	R_{ESR}	$r_{\mathrm{el},3}$
Overheat winding	Winding resistance determination (Section 4.1)	$\tilde{T}_{\mathrm{sp}},\tilde{T}_{\mathrm{winding,max,sp}}$	$R_{\mathrm{winding}},T_{\mathrm{winding}}$	$r_{\mathrm{th},1}$
Overheat magnet	Thermal network (Section 4.4)	$\tilde{T}_{\mathrm{mag,max,sp}}$	T_{mag}	$r_{\mathrm{th},2}$
Defect bearing	Parameter estimation (Section 2.1.3)	-	$\hat{k}_{\mathrm{fr0}},\hat{k}_{\mathrm{fr1}}$	$r_{\mathrm{mech},3},r_{\mathrm{mech},4}$
Dirt on fan blade	Parameter estimation (Section 2.1.3)	-	$\hat{J}$	$r_{\mathrm{mech},2}$
Blockage	Calculation ((5.26))	$\tilde{T}_{\mathrm{cm}},\tilde{k}_{\mathrm{fr0,sp}},\tilde{k}_{\mathrm{fr1,sp}}$	$M_{\mathrm{mot}},M_{\mathrm{fr}},M_{\mathrm{Af}}$	$r_{\mathrm{mech},5}$

6 Summary and Outlook

In this work, a contribution to the area of fault detection and diagnosis for electrically driven engine cooling fans has been made. As is illustrated in Figure 6.1, the focus was set to the determination and handling of *internal states and parameters* of the electrical machine. They not only allow for the development of a detailed fault detection and diagnosis but also serve as an enabler for the reduction of application costs.

This was demonstrated in Section 5, which illustrates the techniques used for detecting and diagnosing selected faults. Due to an efficient *EoL parametrization*, most of the algorithms can be utilized without any additional application effort. It is furthermore shown, that the detailed knowledge of internal states and parameters allows for a straightforward and resource saving implementation.

After an introduction of the engine cooling fan and derivation of corresponding equations, methods for determination of important parameters are presented. Acquisition of the *winding resistance* (see Section 4.1) by injection of a short pulse allows for the detection of *winding faults* and can be used for derivation of the *winding temperature*, which is utilized in the thermal network. The technique furthermore allows for the determination of a winding temperature before starting the motor, which represents a new contribution, as this was not possible so far without a dedicated temperature sensor.

Acquisition of the *flux linkage over rotor position angle* (see Section 4.3) is done during a power-off procedure of the drive by just measuring the line voltages. It is both utilized for torque calculation and for detection of a *demagnetization fault*. In terms of required resources and computing power it is superior to the methods described in the literature.

The equivalent series resistance is, like the method for determination of the winding resistance, based on an injection technique. During *standstill* of the drive a short pulse is injected and the resistance value derived from the system answer by measurement of the DC-link voltage and the line current. It is utilized for detection of an *aged DC-link capacitor*. The proposed method can be applied without requiring a current sensor for the battery current. Compared to existing approaches, it is thus cheaper to implement, as it requires less current sensors to operate.

The algorithms were specifically designed to account for the limited resources available. Usefulness of the proposed methods was proven both by simulation and by evaluation on the test bench. The algorithms can not only be used for engine cooling fans, but are suitable for all continuous run motors. In some cases, such as determination of the equivalent series resistance or the winding resistance during standstill, they can also be used for actuators.

The thermal network presented in Section 4.4 takes the winding, the ambient air temperature and the power loss induced in the windings as an input to determine the current magnet temperature. Both the winding temperature and the magnet temperature are important quantities for fault detection and diagnosis, which is presented in Chapter 5.
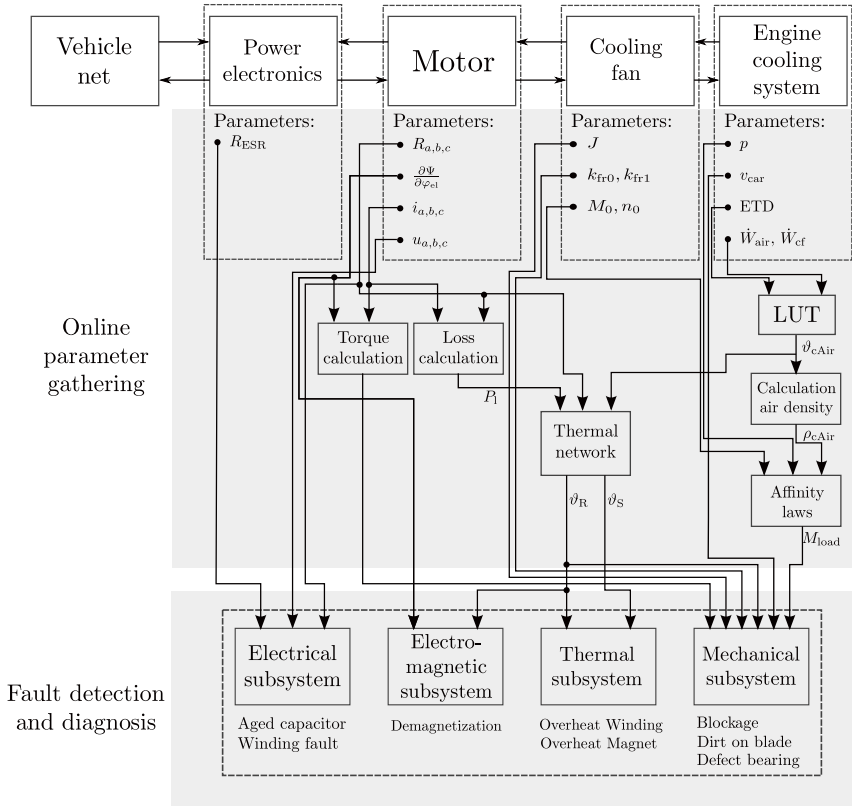
Figure 6.1: Overview of covered topics.

Despite some shortcomings, the presented thermal network poses a promising approach for the online determination of critical motor temperatures. Together with the DC-injection technique (see Section 4.1), it furthermore provides the ability to determine the rotor temperature without any additional application effort.

The presented approach for a thermal network, however, can still be improved by further investigations. Another proposal for a thermal network is depicted in Figure 6.2. It is based on an advancement in model order reduction, which allows for an efficient determination of a state space model based on a complex FEM model. Considering certain boundary conditions, the output temperatures of the state-space model can be chosen arbitrarily. However, the created state space model is only valid for certain environmental conditions, rendering it unsuitable for usage in the field. However, if the relationship between the parameters of the reduced-order model and the environmental conditions were known,

a look-up-table (LUT) could be calculated offline and stored in the microcontroller for later usage. Based on this parameter set and the reduced-order model an observer could be designed, equal to the one proposed in Section 4.4. The observer error could also be designed to be

$$e = \vartheta_\mathrm{S} - \hat{\vartheta}_\mathrm{S} \,, \tag{6.1}$$

with ϑ_S the measured stator temperature and $\hat{\vartheta}_\mathrm{S}$ the observer output. Like in the thermal network presented in Section 4.4, the stator temperature could be measured with the DC-injection technique.

Finding the relationship between the parameters of the reduced-order model and the
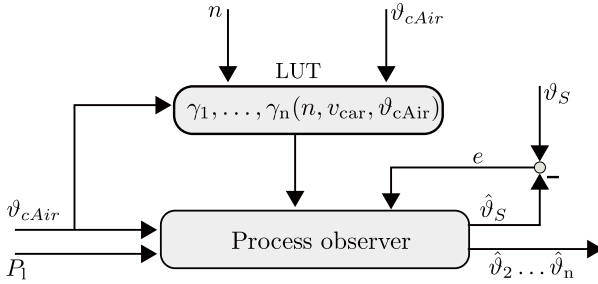

Figure 6.2: Proposal for an online thermal network based on FEM model combined with LUT

environmental conditions is a difficult task and requires extensive research. However, once the LUT can be calculated offline, an efficient online thermal model can be implemented which requires no application effort, as the FEM model is always created during the design phase of the electrical motor and can thus easily be used for the model-order reduction.

Future work in the area of online parameter gathering should concern the adaption of the developed algorithms to dynamic operating points, which would make them more suitable for utilization for actuator applications. In their current implementation, only selected functionalities can be applied to actuators.

Furthermore, due to the novelty grade of the presented algorithms, experience has to be gathered with implementation on series hardware to ensure reliable functioning of the system in all operating conditions.

In summary, following new contributions could be obtained for the field of fault detection for engine cooling fans:

- an enhanced method, which allows for determination of the winding resistance both during standstill and operation of the drive was presented. The value of the winding resistance is utilized for detection of a *winding fault*. Futhermore, it is utilized for derivation of the winding temperature and thus serves as a temperature sensor inside the motor.

- an approach for determination of the equivalent series resistance of the DC-link capacitor was presented, which does not require a battery or capacitor current to be measured. The resistance value is used for *detection of an aged or damaged capacitor*.

- a novel approach for determination of the flux linkage over rotor position angle during a power-off of the engine cooling fan was presented. The acquired flux linkage over rotor position angle is used for detection of a *demagnetization* and utilized for torque calculation.

- a thermal network was developed, which uses the winding temperature and the power loss incurred in the windings to determine the magnet temperature. The temperature of the magnets is used in several places throughout this work, such as adaption of the calculated torque and prevention of an *overheating of the magnets*.

- All above described methods were combined to allow for the detection of several faults at the EoL of the supplier of the electrical machine, the EoL of the car manufacturer and while the engine cooling fan is being operated in the car. Among the fault detection algorithms is a novel approach for detection of unusal load conditions, caused for example by a *blockage*. Due to the possibilities, to acquire all required parameters at the EoL, the application effort to apply the fault detection algorithms to new applications is minimized.

Appendices

A The Condition of a Matrix

The condition number is a measure to determine how linearly dependent a system of equations is or how strong it reacts to measurement uncertainties. The system of equations

$$\mathbf{A} \cdot \mathbf{\Theta} = \mathbf{b} \tag{A.1}$$

is considered well-conditioned if a small change in the coefficient matrix $\mathbf{A}$ or the input vector $\mathbf{b}$ results in a small change in the solution vector $\mathbf{\Theta}$. Likewise, the system (A.1) is considered ill-conditioned if a small change in $\mathbf{A}$ or $\mathbf{b}$ results in a large change in the solution vector $\mathbf{\Theta}$. The definition of the condition number δ is based on the matrix norm. If using the L_2-norm the condition number can be derived as the ratio of the largest to the smallest singular value of $\mathbf{A}$

$$\delta(\mathbf{A}) = \frac{\sigma_{max}}{\sigma_{min}} \geq 1 \tag{A.2}$$

If $\mathbf{A}$ is normal, (A.2) becomes

$$\delta(\mathbf{A}) = \frac{\kappa_{max}}{\kappa_{min}}, \tag{A.3}$$

with κ_{max} and κ_{min} the largest respectively smallest eigenvalue of $\mathbf{A}$.

The higher the condition number, the worse the condition of the matrix. Assuming a disturbance of vector $\mathbf{b}$ by $\Delta\mathbf{b}$ the correct solution according to (A.1) is falsified by $\Delta\mathbf{\Theta}$

$$\mathbf{A}(\mathbf{\Theta} + \Delta\mathbf{\Theta}) = \mathbf{b} + \Delta\mathbf{b}. \tag{A.4}$$

The parameter error hence yields

$$\Delta\mathbf{\Theta} = \mathbf{A}^{-1}\Delta\mathbf{b}. \tag{A.5}$$

By applying the L_2-norm to (A.5), one obtains

$$||\Delta\mathbf{\Theta}|| = ||\mathbf{A}^{-1}\Delta\mathbf{b}|| \leq ||\mathbf{A}^{-1}|| \cdot ||\Delta\mathbf{b}||. \tag{A.6}$$

From (A.1) it follows, that

$$||\mathbf{b}|| = ||\mathbf{A} \cdot \mathbf{\Theta}|| \leq ||\mathbf{A}|| \cdot ||\mathbf{\Theta}||, \tag{A.7}$$

from which one obtains

$$\frac{1}{||\mathbf{\Theta}||} \leq \frac{||\mathbf{A}||}{||\mathbf{b}||}. \tag{A.8}$$

Extending (A.8) with (A.6) finally yields

$$\frac{||\Delta\mathbf{\Theta}||}{||\mathbf{\Theta}||} \leq ||\mathbf{A}|| \cdot ||\mathbf{A}^{-1}|| \frac{||\Delta\mathbf{b}||}{||\mathbf{b}||} = \delta(\mathbf{A}) \frac{||\Delta\mathbf{b}||}{||\mathbf{b}||}, \tag{A.9}$$

which shows, that the relative error $||\Delta\mathbf{b}||/||\mathbf{b}||$ amplifies the relative error of the solution $||\Delta\mathbf{\Theta}||/||\mathbf{\Theta}||$ by the condition number $\delta(\mathbf{A})$. Hence, the condition number should be kept as small as possible. One possibility is a continuous excitation of the process, as this increases the smallest eigenvalue κ_{min}, which in turn decreases the condition number (Vetter, 1988).

B   Star-Delta-Transformation

The motor used for validation of the developed methods is delta-connected. Star quantities have to be transferred to their corresponding delta quantities and vice versa. For the following derivations the notations are used as depicted in Figure 3.5.

Assuming identical values for all phases, resistances can be transformed between star and delta configuration according to

$$R_{\mathrm{Y}} = \frac{1}{3} R_{\Delta} \, . \tag{B.1}$$

When transforming voltages, the harmonics have to be taken into account. The induction voltage of phase a in star configuration can be written as

$$u_{\mathrm{i},a,\mathrm{Y}}(t) = \frac{a_0}{2} + \sum_{k=1}^{\infty} \left(A_k \cos(k\omega t - \varphi_k) \right) \, .$$

Substituting

$$\alpha = \omega t \, ,$$

and considering a phase-shift of 120° for phase b, the induced voltages in star configuration can be written as

$$u_{\mathrm{i},a,\mathrm{Y}}(\alpha) \;=\; \frac{a_0}{2} + \sum_{k=1}^{\infty} \left(A_k \cos(k\alpha - \varphi_k) \right) \tag{B.2}$$

$$u_{\mathrm{i},b,\mathrm{Y}}(\alpha) \;=\; \frac{a_0}{2} + \sum_{k=1}^{\infty} \left(A_k \cos(k(\alpha - \frac{2}{3}\pi) - \varphi_k) \right) \, . \tag{B.3}$$

Transferring the induced voltages in phases a and b to the delta connected motor yields

$$u_{\mathrm{i},uv,\Delta}(\alpha) \;=\; u_{\mathrm{i},a,\mathrm{Y}}(\alpha) - u_{\mathrm{i},b,\mathrm{Y}}(\alpha) \tag{B.4}$$

$$=\; \sum_{k=1}^{\infty} A_k \left(\cos(k\alpha - \varphi_k) - \cos(k(\alpha - \frac{2}{3}\pi) - \varphi_k) \right) \, .$$

Using the addition theorem, which states that

$$\cos(x) - \cos(y) = 2\sin\frac{y+x}{2}\sin\frac{y-x}{2} \, ,$$

equation (B.4) can be rearranged to

$$u_{\mathrm{i},uv,\Delta}(\alpha) = \sum_{k=1}^{\infty} A_k \left(2\sin(k\alpha - k\frac{\pi}{3} - \varphi_k)\sin(-k\frac{\pi}{3}) \right) = \sum_{k=1}^{\infty} u_{\mathrm{i},uv,\Delta,k}(\alpha) \, . \tag{B.5}$$

Substitung $k = 6n + \zeta$, $n \in \mathbb{N}_0$, equation (B.5) can be solved as

$$u_{\mathrm{i},uv,\Delta,k}(\alpha) = A_k \cdot \begin{cases} -\sqrt{3}\sin(k\alpha - \varphi_k - k\frac{\pi}{3}) & \text{for } \zeta \in [1,2] \\ \sqrt{3}\sin(k\alpha - \varphi_k - k\frac{\pi}{3}) & \text{for } \zeta \in [4,5] \\ 0 & \text{for } \zeta \in [0,3] \end{cases} \tag{B.6}$$

C State Variable Filter

When using continuous process models for estimating unknown process parameters, time derivatives of certain variables often appear in these equations. As the time derivatives can seldomly be measured in the system, they have to be calculated in software. However, standard differentiation methods can hardly be implemented, as they amplify the signal noise. To overcome this problem, Wolfram and Vogt (2002) describes alternative ways for computing time derivatives. The method used in this work is the state variable filter, which is an analog filter in Frobenius form (direct form II), in which the internal states correspond to the differentials of the filtered signal.

Consider the following transfer function

$$G(s) = \frac{Y(s)}{U(s)} = \frac{b_0}{a_{\mathrm{n}}s^n + a_{\mathrm{n-1}}s^{n-1} + \ldots + a_1 s + a_0} \tag{C.1}$$

in canonical form, i.e. $a_{\mathrm{n}} = 1$. In the time domain this equals

$$y^{(n)} + a_{\mathrm{n-1}}y^{(n-1)} + \ldots + a_1\dot{y} + a_0 y = b_0 u \,. \tag{C.2}$$

Letting $y = x_1$, one can derive the following equations:

$$\dot{x}_1 \;=\; x_2 \tag{C.3}$$
$$\dot{x}_2 \;=\; x_3 \tag{C.4}$$
$$\vdots \tag{C.5}$$
$$\dot{x}_{n-1} \;=\; x_n \tag{C.6}$$
$$\dot{x}_{\mathrm{n}} \;=\; -a_{\mathrm{n-1}}x_{(\mathrm{n})} - a_{\mathrm{n-2}}x_{(\mathrm{n-1})} - \ldots - a_1 x_2 - a_0 x_1 + b_0 u \,. \tag{C.7}$$

This yields the following equations in state space notation

$$
\begin{pmatrix} \dot{x}_1 \\ \dot{x}_2 \\ \vdots \\ \dot{x}_{n-1} \\ \dot{x}_{\mathrm{n}} \end{pmatrix}
=
\begin{pmatrix}
0 & 1 & 0 & \cdots & 0 \\
0 & 0 & 1 & \cdots & 0 \\
\vdots & \vdots & \vdots & \ddots & \vdots \\
0 & 0 & 0 & \ldots & 1 \\
-a_0 & -a_1 & -a_2 & \cdots & -a_{n-1}
\end{pmatrix}
\cdot
\begin{pmatrix} x_1 \\ x_2 \\ \vdots \\ x_{n-1} \\ x_{\mathrm{n}} \end{pmatrix}
+
\begin{pmatrix} 0 \\ 0 \\ \vdots \\ 0 \\ b_0 \end{pmatrix}
\cdot u \tag{C.8}
$$

$$
y =
\begin{pmatrix}
1 & 0 & \ldots & 0 & 0 \\
0 & 1 & \ldots & 0 & 0 \\
\vdots & \vdots & \ddots & \vdots & \\
0 & 0 & \ldots & 1 & 0 \\
0 & 0 & \ldots & 0 & 1
\end{pmatrix}
\cdot
\begin{pmatrix} x_1 \\ x_2 \\ \vdots \\ x_{n-1} \\ x_{\mathrm{n}} \end{pmatrix}
+
\begin{pmatrix} 0 \\ 0 \\ \vdots \\ 0 \\ 0 \end{pmatrix}
\cdot u \tag{C.9}
$$

As can be seen, the internal states correspond to the looked for quantities.

D   Datasheet Parameters of Selected Test Bench Components

Load machine

Manufacturer	Stoeber Antriebstechnik GmbH + Co. KG
Model	EK501U
Type	Permanent magnet brushless motor, electronically commutated
Rated speed	$6000\,\mathrm{min}^{-1}$
Rated torque	$2.6\,\mathrm{N\,m}$
Rated Power	$1.6\,\mathrm{kW}$
Stall Torque	$3.36\,\mathrm{N\,m}$
Peak Torque	$15\,\mathrm{N\,m}$
Electrical time constant	$2.85\,\mathrm{ms}$
Mass moment of inertia	$3.19 \times 10^{-4}\,\mathrm{kg\,m}^2$

Torque sensor

Manufacturer	Lorenz Messtechnik GmbH
Model	DR-2531
Type	Contactless dual range torque sensor
Maximum speed	$1200\,\mathrm{min}^{-1}$
Nominal torque	$2\,\mathrm{N\,m} \cdots 20\,\mathrm{N\,m}$
Accuracy	$0.1\,\%$ from scale

Incremental encoder

Manufacturer	Heidenhain
Model	ERN420
Increments	1024

Bibliography

Baehr, **H. D. and K. Stephan** (2013). *Wärme- und Stoffübertragung*. 8th ed. Berlin: Springer Vieweg.

Basak, **D.**, **A. Tiwari**, **and S. Das** (2006). "Fault diagnosis and condition monitoring of electrical machines - A Review". *IEEE International Conference on Industrial Technology (ICIT)*. Mumbai, India, pp. 3061–3066.

Becker, **K. and J. Kaye** (1962). "Measurements of Diabatic Flow in an Annulus With an Inner Rotating Cylinder". *Journal of Heat Transfer*, vol. 84, pp. 97–104.

Benecke, **W.** (1966). "Temperaturfeld und Wärmefluss bei kleineren oberflächengekühlten Drehstrommotoren mit Käfigläufer". *ETZ-A*, vol. 87, no. 13, pp. 455–459.

Binder, **A.** (2012). *Elektrische Maschinen und Antriebe. Grundlagen, Betriebsverhalten*. 1st ed. Berlin: Springer-Verlag.

Blodt, **M.**, **P. Granjon**, **B. Raison**, **and G. Rostaing** (2008). "Models for Bearing Damage Detection in Induction Motors Using Stator Current Monitoring". *IEEE Transactions on Industrial Electronics*, vol. 55, no. 4, pp. 1813–1822.

Boglietti, **A.**, **A. Cavagnino**, **and D. Staton** (2008). "Determination of Critical Parameters in Electrical Machine Thermal Models". *IEEE Transactions on Industry Applications*, vol. 44, no. 4, pp. 1150–1159.

Boglietti, **A.**, **A. Cavagnino**, **D. Staton**, **M. Shanel**, **M. Mueller**, **and C. Mejuto** (2009). "Evolution and Modern Approaches for Thermal Analysis of Electrical Machines". *IEEE Transactions on Industrial Electronics*, vol. 56, no. 3, pp. 871–882.

Bohl, **W. and W. Elmendorf** (2008). *Strömungsmaschinen 1. Aufbau und Wirkungsweise*. 10th ed. Kamprath-Reihe. Würzburg: Vogel.

Bommes, **L.** (1994). *Ventilatoren*. Essen: Vulkan-Verlag.

Brown, **J.** (2004). *Power MOSFET Basics: Understanding Gate Charge and Using it to Assess Switching Performance*. Malvern, Pennsylvania, USA: Vishay Siliconix.

Brünglinghaus, **C. and J. Winterhagen** (2011). "CO_2 Limits Determine Future Direction". *ATZ worldwide eMagazines Edition*, no. 2. URL: http://www.atzonline.com/index.php;do=auth/site=a4e/sid=06599ttc0rc8mr8v00hr5va6e5/alloc=3/id=12588/pdfdir=atzww/pdf_filename=a02-11-02.pdf/key=d8ab8d0f357bc3fea12444a30c289b6e (Retrieved 11/13/2013).

Casadei, **D.**, **F. Filippetti**, **C. Rossi**, **and A. Stefani** (2009). "Magnets faults characterization for Permanent Magnet Synchronous Motors". *IEEE International Symposium on Diagnostics for Electric Machines, Power Electronics and Drives (SDEMPED)*. Cargese, France, 6 pp.

CDM Cornell Duilier (2013). *Aluminum Electrolytic Capacitor Application Guide*. CDM Cornell Dubilier. Liberty, South Carolina, USA.

Chowdhury, **S. and P. Baski** (2010). "A simple lumped parameter thermal model for electrical machine of TEFC design". *2010 Joint International Conference on Power Electronics, Drives and Energy Systems (PEDES)*. New Delhi, India, 7 pp.

Da, **Y.**, **X. Shi**, **and M. Krishnamurthy** (2011). "Health monitoring, fault diagnosis and failure prognosis techniques for Brushless Permanent Magnet Machines". *IEEE Vehicle Power and Propulsion Conference (VPPC)*. Chicago, Illinois, USA, 7 pp.

Dietrich, **H.** (1970). "Interdependence of thermal aftereffect and natural aging in permanent magnet materials". *IEEE Transactions on Magnetics*, vol. 6, no. 2, pp. 272 − 275.

Dou, **Z.**, **R. Xu**, **and A. Berduque** (2008). "The Development of Electrolytes in Aluminium Electrolytic Capacitors for Automotive and High Temperature Applications". *CARTS-Europe Conference*. Helsinki, Finland, 11 pp.

Duran, **M. and J. Fernandez** (2004). "Lumped-parameter thermal model for induction machines". *IEEE Transactions on Energy Conversion*, vol. 19, no. 4, pp. 791–792.

Ebrahimi, **B.**, **J. Faiz**, **and M. Roshtkhari** (2009). "Static-, Dynamic-, and Mixed-Eccentricity Fault Diagnoses in Permanent-Magnet Synchronous Motors". *IEEE Transactions on Industrial Electronics*, vol. 56, no. 11, pp. 4727–4739.

Ebrahimi, **B.**, **J. Faiz**, **and B. Araabi** (2010). "Pattern identification for eccentricity fault diagnosis in permanent magnet synchronous motors using stator current monitoring". *Electric Power Applications, IET*, vol. 4, no. 6, pp. 418–430.

Edwards, **S.**, **R. Müller**, **G. Feldhaus**, **T. Finkeldei**, **and M. Neubauer** (2008). "CO2-Minderung bei einem Turbo-DI-Ottomotor durch optimiertes Thermomanagement". *MTZ - Motortechnische Zeitschrift*, vol. 69, no. 1, pp. 26–33.

Eilemann, **A. and E. Pantow** (2014). "Thermomanagement - Komponenten für innovative Kühlsysteme". *Internationaler Motorenkongress 2014*. Baden-Baden, Germany: Springer Fachmedien Wiesbaden, pp. 517–533.

EU Proposal (2012). *Proposal for a Regulation of the European Parliament and of the Council amending Regulation (EC) No 443/2009 to define the modalities for reaching the 2020 target to reduce CO2 emissions from new passenger cars*. URL: http://eur-lex.europa.eu/LexUriServ/LexUriServ.do?uri=COM:2012:0393:FIN:EN:PDF (Retrieved 11/13/2013).

EU Regulation 443 (2009). *Regulation (EC) No. 443/2009 of the European Parliament and of the Coucil of 23 April 2009 setting emission performance standards for new passenger cars as part of the Community's integrated approach to reduce CO2 emissions*

from light-duty vehicles. URL: http://eur-lex.europa.eu/LexUriServ/LexUriServ.do?uri=OJ:L:2009:140:0063:008:en:PDF (Retrieved 11/13/2013).

EU Regulation 661 (2009). *Regulation (EC) No. 661/2009 of the European Parliament and of the Council of 13 July 2009 concerning type-approval requirements for the general safety of motor vehicles, their trailers and systems, components and separate technical units intended therefor.* URL: http://eur-lex.europa.eu/legal-content/EN/TXT/PDF/?uri=CELEX:32009R0661&from=EN (Retrieved 11/15/2013).

Fabis, M. (2006). "Beitrag zum Energiemanagement in Kfz-Bordnetzen". Dissertation. Technische Universität Berlin.

Föllinger, O., **F. Dorrscheidt**, **and M. Klittich** (2008). *Regelungstechnik. Einführung in die Methoden und ihre Anwendung.* 10th ed. Heidelberg: Hüthig Verlag.

Füssel, D. (2002). "Fault Diagnosis with Tree-Structured Neuro-Fuzzy Systems". Dissertation. Technische Universität Darmstadt.

Gandhi, A., **T. Corrigan**, **and L. Parsa** (2011). "Recent Advances in Modeling and Online Detection of Stator Interturn Faults in Electrical Motors". *IEEE Transactions on Industrial Electronics*, vol. 58, no. 5, pp. 1564–1575.

Gasperi, M. (1996). "Life prediction model for aluminum electrolytic capacitors". *Conference Record of the 1996 IEEE Industry Applications Conference (IAS)*, vol. 3, pp. 1347–1351.

Gorter, R. J. A., **P. P. J.** van den **Bosch**, **and S. Weiland** (1995). "Simultaneous estimation of induction machine parameters and velocity". *26th Annual IEEE Power Electronics Specialists Conference (PESC)*, vol. 2, pp. 1295–1301.

Graovac, D., **M. Pürschel**, **and A. Kiep** (2006). *MOSFET Power Losses Calculation Using the Data-Sheet parameters.* Infineon. Neubiberg, Germany.

Harada, K., **A. Katsuki**, **and M. Fujiwara** (1993). "Use of ESR for deterioration diagnosis of electrolytic capacitor". *IEEE Transactions on Power Electronics*, vol. 8, no. 4, pp. 355–361.

Haylock, J., **U. Hoefer**, **and A. Jack** (2006). "Predicting and preventing demagnetisation in permanent magnet motor drives". *The 3rd IET International Conference on Power Electronics, Machines and Drives (PEMD)*. Dublin, Ireland, pp. 474 –478.

Henao, H., **G.-A Capolino**, **M. Fernandez-Cabanas**, **F. Filippetti**, **C. Bruzzese**, **E. Strangas**, **R. Pusca**, **J. Estima**, **M. Riera-Guasp**, **and S. Hedayati-Kia** (2014). "Trends in Fault Diagnosis for Electrical Machines: A Review of Diagnostic Techniques". *IEEE Industrial Electronics Magazine*, vol. 8, no. 2, pp. 31–42.

Howey, D., **P. Childs**, **and A. Holmes** (2012). "Air-Gap Convection in Rotating Electrical Machines". *IEEE Transactions on Industrial Electronics*, vol. 59, no. 3, pp. 1367–1375.

Höfling, **T.** (1996). "Methoden zur Fehlererkennung mit Parameterschätzung und Paritätsgleichungen". Dissertation. Technische Hochschule Darmstadt.

Imam, **A.**, **T. Habetler**, **R. Harley**, **and D. Divan** (2005). "Condition Monitoring of Electrolytic Capacitor in Power Electronic Circuits using Adaptive Filter Modeling". *36th IEEE Power Electronics Specialists Conference (PESC)*. Recife, Brazil, pp. 601–607.

Isermann, **R.** (2006). *Fault-Diagnosis Systems. An Introduction from Fault Detection to Fault Tolerance.* 1st ed. Berlin: Springer-Verlag.

Isermann, **R.** (2008). *Mechatronische Systeme. Grundlagen.* 2nd ed. Berlin: Springer-Verlag.

Isermann, **R.** (2011). *Fault-Diagnosis Applications. Model-based condition monitoring: Actuators, drives, machinery, plants, sensors, and fault tolerant-systems.* 1st ed. Berlin: Springer-Verlag.

Isermann, **R. and M. Münchhof** (2011). *Identification of Dynamic Systems. An Introduction with Applications.* 1st ed. Berlin: Springer-Verlag.

Jacobina, **C.**, **J. Filho, and A. Lima** (2000). "On-line estimation of the stator resistance of induction machines based on zero-sequence model". *IEEE Transactions on Power Electronics*, vol. 15, no. 2, pp. 346–353.

Kallenbach, **E.**, **R. Eick**, **T. Ströhla**, **K. Feindt**, **M. Kallenbach**, **and O. Radler** (2012). *Elektromagnete. Grundlagen, Berechnung, Entwurf und Anwendung.* 4th ed. Wiesbaden: Vieweg + Teubner Verlag.

Khoobroo, **A. and B. Fahimi** (2010). "A novel method for permanent magnet demagnetization fault detection and treatment in permanent magnet synchronous machines". *Twenty-Fifth Annual IEEE Applied Power Electronics Conference and Exposition (APEC)*. Palm Springs, California, USA, pp. 2231–2237.

Kim, **M.**, **S. Sul**, **and J. Lee** (2012). "Condition monitoring of DC-link capacitors in drive system for electric vehicles". *Vehicle Power and Propulsion Conference (VPPC)*. Seoul, South Korea, pp. 633–637.

Kowalczyk, **M.**, **F. Kunkel**, **and R. Isermann** (2013). "Online iterative real-time measurements and modeling of combustion engines". *13th Stuttgart International Symposium on Automotive and engine technology.* Vol. 2. Stuttgart, pp. 515–534.

Krebber-Hortmann, **K.**, **A. Köster**, **A. Tönnesmann**, **and C. Brunetti** (2013). "Möglichkeiten zur Kraftstoffeinsparung durch elektrische Nockenwellenverstellung". *MTZ - Motortechnische Zeitschrift*, vol. 74, no. 11, pp. 854–859.

Krüger, **H. U.** (2003). "Betriebsdiagnose bei Elektronikmotoren". Dissertation. Technische Universität Braunschweig.

Lee, **K.**, **M. Kim**, **J. Yoon**, **S. Lee**, **and J. Yoo** (2008). "Condition Monitoring of DC-Link Electrolytic Capacitors in Adjustable-Speed Drives". *IEEE Transactions on Industry Applications*, vol. 44, no. 5, pp. 1606–1613.

Lee, **S.-B. and T. Habetler** (2003). "An online stator winding resistance estimation technique for temperature monitoring of line-connected induction machines". *IEEE Transactions on Industry Applications*, vol. 39, no. 3, pp. 685–694.

Lee, **W.-C.**, **T.-K. Lee**, **and D.-s. Hyun** (2001). "Comparison of single-sensor current control in the DC link for three-phase voltage-source PWM converters". *IEEE Transactions on Industrial Electronics*, vol. 48, no. 3, pp. 491–505.

Leonhard, **W.** (2001). *Control of Electrical Drives*. 3rd ed. Berlin: Springer-Verlag.

Lunze, **J.** (2008). *Regelungstechnik 2. Mehrgrößensysteme, Digitale Regelung*. 2nd ed. Berlin: Springer-Verlag.

Ma, **H. and L. Wang** (2005). "Fault diagnosis and failure prediction of aluminum electrolytic capacitors in power electronic converters". *31st Annual Conference of IEEE Industrial Electronics Society (IECON)*. Raleigh, North Carolina, USA, 6 pp.

Marcetic, **D. and E. Adzic** (2010). "Improved Three-Phase Current Reconstruction for Induction Motor Drives With DC-Link Shunt". *IEEE Transactions on Industrial Electronics*, vol. 57, no. 7, pp. 2454–2462.

Microchip (2009). *Single-Shunt Three-Phase Current Reconstruction Algorithm for Sensorless FOC of a PMSM*. URL: http://ww1.microchip.com/downloads/en/AppNotes/01299A.pdf.

Moreno, **J. F.**, **F. Hidalgo**, **and M. Martinez** (2001). "Realisation of tests to determine the parameters of the thermal model of an induction machine". *IEEE Proceedings on Electric Power Applications*, vol. 148, no. 5, pp. 393–397.

Moseler, **O.** (2001). "Microcontrollerbasierte Fehlererkennung für mechatronische Komponenten am Beispiel eines elektromechanischen Stellantriebs". Dissertation. Technische Universität Darmstadt.

Nandi, **S.**, **H. Toliyat**, **and L. Xiaodong** (2005). "Condition Monitoring and Fault Diagnosis of Electrical Motors - A Review". *IEEE Transactions on Energy Conversion*, vol. 20, no. 4, pp. 719–729.

Parler, **S. and L. Macomber** (1999). *Predicting Operating Temperature and Expected Lifetime of Aluminum-Electrolytic Bus Capacitors with Thermal Modeling*. CDM Cornell Dubilier. Liberty, South Carolina, USA.

Pfeufer, **T.** (1999). "Modellgestützte Fehlererkennung und Diagnose am Beispiel eines Kraftfahrzeugaktors". Dissertation. Technische Universität Darmstadt.

Plotkin, **J.**, **M. Stiebler**, **and D. Schuster** (2008). "A novel method for online stator resistance estimation of inverter-fed ac-machines without temperature sensors". *11th International Conference on Optimization of Electrical and Electronic Equipment (OP-TIM)*. Brasov, Romania, pp. 155–161.

Pyrhönen, **J.**, **T. Jokinen**, **and V. Hrabovcová** (2008). *Design of rotating electrical machines*. 1st ed. Chichester: Wiley.

Rau, **A.** (2006). "Dezentrale elektrische Antriebe im Automobil". *ATZ - Automobiltechnische Zeitschrift*, vol. 108, no. 11, pp. 940–944.

Reif, **K.** (2012). *Sensoren im Kraftfahrzeug*. Bosch Fachinformation Automobil. Wiesbaden: Vieweg+Teubner Verlag.

Robert Bosch GmbH (2011). *Automotive Handbook*. 8th ed. Robert Bosch GmbH.

Rosero, **J.**, **L. Romeral**, **J. Cusido**, **and J. Ortega** (2007). "Fault detection by means of wavelet transform in a PMSMW under demagnetization". *33rd Annual Conference of the IEEE Industrial Electronics Society (IECON)*. Taipei, Taiwan, pp. 1149 –1154.

Rosero, **J.**, **J. Cusido**, **A. Garcia**, **J. Ortega**, **and L. Romeral** (2006). "Study on the Permanent Magnet Demagnetization Fault in Permanent Magnet Synchronous Machines". *32nd Annual Conference on IEEE Industrial Electronics (IECON)*. Paris, France, pp. 879 –884.

Ruoho, **S. and A. Arkkio** (2008). "Partial Demagnetization of Permanent Magnets in Electrical Machines Caused by an Inclined Field". *IEEE Transactions on Magnetics*, vol. 44, no. 7, pp. 1773 –1778.

Ruoho, **S.**, **J. Kolehmainen**, **J. Ikaheimo**, **and A. Arkkio** (2010). "Interdependence of Demagnetization, Loading, and Temperature Rise in a Permanent-Magnet Synchronous Motor". *IEEE Transactions on Magnetics*, vol. 46, no. 3, pp. 949 –953.

Ruschetti, **C.**, **G. Bossio**, **C. De Angelo**, **and C. Verucchi** (2010). "Effects of partial rotor demagnetization on permanent magnet synchronous machines". *2010 IEEE International Conference on Industrial Technology (ICIT)*. Vi a del Mar, Chile, pp. 1233 –1238.

Saadaoui, **W. and K. Jelassi** (2011). "Induction motor bearing damage detection using stator current analysis". *IEEE International conference on Power Engineering, Energy and Electrical Drives (POWERENG)*. Torremolinos, Malaga, Spain, 6 pp.

Schlender, **F. and G. Klingenberg** (1996). *Ventilatoren im Einsatz. Anwendung in Geräten und Anlagen*. Berlin: Springer-Verlag.

Schmidt, **M.** (2003). "Maßnahmen zur Reduktion des Energieverbrauchs von Nebenaggregaten im Kraftfahrzeug". Dissertation. Technische Universität Darmstadt.

Schmiederer, **K.** (2011). "Thermomanagement als Zukunftsaufgabe im Automobilbau". *ATZextra*, vol. 6, pp. 66 –70.

Schröder, **D.** (2009). *Elektrische Antriebe - Grundlagen. Mit durchgerechneten Übungs- und Prüfungsaufgaben*. 4th ed. Berlin: Springer-Verlag.

Sebastian, **K.**, **C. Kurdzel**, **K. Martin**, **and R. Kirchhoff** (2010). "Thermomanagement und Innenraumklimatisierung". *ATZextra*, vol. 15, no. 11, pp. 82–91.

Shaoyong, **Y.**, **D. X.**, **A. Bryant**, **P. Mawby**, **L. Ran**, **and P. Tavner** (2010). "Condition Monitoring for Device Reliability in Power Electronic Converters: A Review". *IEEE Transactions on Power Electronics*, vol. 25, no. 11, pp. 2734–2752.

Simonin, **M.**, **S. Burgold**, **B. Gessier**, **and M. Ponchant** (2008). "Modular front-end cooling module architecture for future powertrains". *ATR worldwide*, vol. 110, no. 7-8, pp. 22–29.

Souza Ribeiro, **L.** de, **C. Jacobina**, **and A. Lima** (1999). "Linear parameter estimation for induction machines considering the operating conditions". *IEEE Transactions on Power Electronics*, vol. 14, no. 1, pp. 62–73.

Staton, **D.**, **A. Boglietti**, **and A. Cavagnino** (2005). "Solving the More Difficult Aspects of Electric Motor Thermal Analysis in Small and Medium Size Industrial Induction Motors". *IEEE Transactions on Energy Conversion*, vol. 20, no. 3, pp. 620–628.

Stiebler, **M. and Y. Plotkin** (2005). "Online winding temperature monitoring of PWM inverter-fed induction machines". *European Conference on Power Electronics and Applications (EPE)*. Dresden, Germany, 5 pp.

Straky, **H.** (2003). "Modellgestützter Funktionsentwurf für Kfz-Stellglieder : Regelung der elektromechanischen Ventiltriebaktorik und Fehlerdiagnose der Bremssystemhydraulik". Dissertation. TU Darmstadt.

Straßer, **K.** (1990). "Ein Beitrag zur Berechnung der PKW-Motorkühlung unter Berücksichtigung des Verbrennungsverfahrens". Dissertation. Technische Universität München.

Taylor, **G. I.** (1923). "Stability of a viscous liquid contained between two rotating cylinders". *Philosophical Transactions of the Royal Society A*, vol. 223, pp. 289–343.

Velez-Reyes, **M.**, **K. Minami**, **and G. C. Verghese** (1989). "Recursive speed and parameter estimation for induction machines". *Conference Record of the 1989 IEEE Industry Applications Society Annual Meeting*. Vol. 1. San Diego, California, USA, pp. 607–611.

Vetter, **T.** (1988). "Überwachung und Prädiktion des Erwärmungsverhaltens einer Asynchronmaschine mit Käfigläufer mittels Parameterschätzung". Dissertation. Technische Hochschule Darmstadt.

Walter, **J.** (2001). "Automotive Cooling System Component Interactions". PhD thesis. Texas, USA: Graduate Faculty of Texas Tech University.

Wechsler, **A.**, **B. Mecrow**, **D. Atkinson**, **J. Bennett**, **and M. Benarous** (2012). "Condition Monitoring of DC-Link Capacitors in Aerospace Drives". *IEEE Transactions on Industry Applications*, vol. 48, no. 6, pp. 1866–1874.

Wilson, **S.**, **G. Jewell**, **and P. Stewart** (2005). "Resistance estimation for temperature determination in PMSMs through signal injection". *IEEE International Conference on Electric Machines and Drives (IEMDC)*. San Antonio, Texas, USA, pp. 735–740.

Wolfram, **A. and M. Vogt** (2002). "Zeitdiskrete Filteralgorithmen zur Erzeugung zeitlicher Ableitungen". *at - Automatisierungstechnik*, vol. 7, pp. 346–353.

Wolfram, **A.** (2002). "Komponentenbasierte Fehlerdiagnose industrieller Anlagen am Beispiel frequenzumrichtergespeister Asynchronmaschinen und Kreiselpumpen". Dissertation. Technische Universität Darmstadt.

Wu, **Y. and H. Gao** (2006). "Induction-motor stator and rotor winding temperature estimation using signal injection method". *IEEE Transactions on Industry Applications*, vol. 42, no. 4, pp. 1038–1044.

Xie, **L.**, **Q. Miao**, **Y. Chen**, **W. Liang**, **and M. Pecht** (2012). "Fan bearing fault diagnosis based on continuous wavelet transform and autocorrelation". *IEEE Conference on Prognostics and System Health Management (PHM)*. Minneapolis, Minnesota, USA, 6 pp.

Zhang, **P.**, **Y. Du**, **T. Habetler**, **and B. Lu** (2011). "Magnetic Effects of DC Signal Injection on Induction Motors for Thermal Evaluation of Stator Windings". *IEEE Transactions on Industrial Electronics*, vol. 58, no. 5, pp. 1479–1489.

Zhou, **W.**, **T. Habetler**, **and R. Harley** (2007). "Stator Current-Based Bearing Fault Detection Techniques: A General Review". *IEEE International Symposium on Diagnostics for Electric Machines, Power Electronics and Drives (SDEMPED)*. Cracow, Poland, pp. 7–10.

Supervised Bachelor and Master Theses

Arican, **S.** (2012). "Entwicklung einer schnellen Berechnungsmethode zur Verlustleistungsberechnung eines B6-Wechselrichters". B.Sc. Thesis. Duale Hochschule Baden-Württemberg, Karlsruhe.

Decker, **G.** (2013). "Entwicklung von Verfahren zur Ermittlung der Flussverkettung eines EC-Motors im laufenden Betrieb". Diploma Thesis. Wilhelm Buechner Hochschule Darmstadt.

Online-Buchshop für Ingenieure

Die Reihen der Fortschritt-Berichte VDI:

ISBN 978-3-18-5**26208**-1